Improving Kidney Stone Treatment through Materials Chemistry

by

John Wesley Robinson

A dissertation submitted in partial fulfillment
of the requirements for the degree of
Doctorate of Philosophy
(Chemistry)
in the University of Michigan
2024

Doctoral Committee:

Professor Adam J. Matzger, Chair
Professor Stephen Maldonado
Professor William W. Roberts
Associate Professor Dominica Zgid

John Robinson

johnwr@umich.edu

ORCID iD: 0000-0002-8185-2699

© John Robinson 2024

Dedication

To every NDN that has suffered from a kidney stone, I hope this research helps reduce the burden of stone disease in our communities in some small way.

Acknowledgements

First, I thank my research adviser, Professor Adam Matzger, for his support and guidance in my time at the University of Michigan. I am especially grateful for the space and trust he has given me to grow from anxious student to more confident scientist who manages their research independently. Thank you for helping me build a solid intellectual and personal foundation that will enable my continued growth throughout my career.

I am also thankful for my committee members, Professor Dominika Zgid, Professor Stephen Maldonado, and Professor William Roberts for their guidance over the past four years as I have conducted research and prepared this dissertation. I am especially grateful for Dr. Roberts who has often acted as a second research adviser to me and taught me a great deal about kidney stones and the medical approaches to their treatment. I would also like to thank my collaborators the urology department at Michigan Medicine especially Dr. Khurshid Ghani, Niki Kajeh, and Ron Marom who all helped me better understand kidney stone treatment.

Numerous teachers and advisers have contributed to my intellectual and personal growth over the years. Of these, I want to thank Professor Gerald van Hecke and Professor Kathleen Nolta for believing in my ability to succeed and encouraging me even when I doubted myself.

Graduate school is often challenging, and the friends I have made have contributed much to my personal growth in this time. Thank you to members of the Matzger group both past and present for the support and friendly environment that has made working in lab a positive experience. Outside of lab, I want to thank the Native American Student Association for providing

a welcoming environment for someone who often feels caught between cultures. And finally: gracias, thank you, miigwech, ᖶᐱᑕᑎ to my friends Gloria, Laurel, Mahalina, and Ariel for the conversations, walks, gardening, and other nonsense made my time in graduate school more enjoyable than I ever expected.

Table of Contents

Dedication ii

Acknowledgements iii

List of Tables viii

List of Figures ix

Abstract xiv

Chapter 1 Introduction 1

1.1 Kidney stones as materials 1

1.2 Kidney stone disease 1

1.2.1 Calcium oxalate stones 2

1.2.2 Calcium phosphates 3

1.2.3 Uric acid 4

1.2.4 Struvite and other infectious stones 5

1.3 Lithotripsy 5

1.4 Photothermal laser ablation 7

1.5 From crystals to kidney stones 8

1.6 Outline of dissertation 10

Chapter 2 Photothermal Properties of Kidney Stone Minerals 12

2.1 Introduction 12

2.2 Methods 13

2.2.1 Crystal growth 13

2.2.1 Absorption coefficient measurements 20

2.2.2 Diffuse reflectance measurements 21
2.3 Results and discussion 22
2.3.1 Comparing absorption at different laser wavelengths 22
2.3.2 Assignment of near-infrared peaks to vibrational modes 24
2.3.1 Diffuse reflectance 28
2.3.2 Applying absorption coefficients to lithotripsy research 30
2.4 Conclusions 31
Chapter 3 Raman Mapping for Structural Analysis of Kidney Stones 32
3.1 Introduction 32
3.1.1 Techniques for structural analysis of kidney stones 32
3.1.2 Raman spectroscopy for kidney stone analysis 34
3.2 Methods 35
3.2.1 Sample preparation 35
3.2.2 Raman mapping 37
3.3 Results and Discussion 38
3.3.1 Raman spectra of powdered minerals 38
3.3.2 COM stone (type 1a) 42
3.3.3 Uric acid stone 43
3.3.4 Brushite stone 45
3.3.5 Struvite stone 47
3.3.6 Mixed calcium oxalate and calcium phosphate stones 52
3.4 Conclusions 55
3.5 Appendix: Additional Raman spectra 56
Chapter 4 Improved Kidney Stone Models 62
4.1 Materials and methods 63

4.1.1 Brushite plasters 63
4.1.2 Single-pulse lithotripsy 66
4.2 Results and Discussion 67
4.2.1 Quantitative ablation performance 67
4.2.2 Microstructure 74
4.2.3 Examples of fracture 75
4.3 Conclusions 77
Chapter 5 Future Work 78
5.1 Additional phantoms 78
5.1.1 Struvite plaster 78
5.1.2 COM/chitosan composites 80
5.2 Orientation effects in the Raman spectrum of calcium oxalates 82
5.3 Growing kidney stones in vitro 86
5.4 Modeling kidney stone fragmentation 89
5.4.1 Radiative transfer 90
5.4.2 Thermal properties 91
5.4.3 Computational modeling of mechanical destruction 92
Appendix: Additional Raman Images 93
References 101

List of Tables

Table 1.1: Common kidney stone compounds and their prevalence. 2

Table 2.1: Absorption coefficients at commercial thulium fiber (k_{TF}, 1.94 μm) and Ho:YAG ($k_{Ho:YAG}$, 2.12 μm) laser lithotripter wavelengths along the crystallographic directions indicated. 22

Table 3.1: Raman mapping settings for listed figures. 38

Table 3.2: Raman peaks for mineral identification in kidney stone mapping. 39

Table 4.1: Brushite plaster formulations. 66

Table 4.2: Table of ablated crater volumes and mole fraction of calcium phosphate. Composition percentages may not add up to 100% due to rounding or presence of unidentified compounds. 68

Table 5.1: Concentration of artificial urine components. Adapted from Sarigul et al.[152] 87

Table 5.2: Table of available thermal data for kidney stone minerals. 92

List of Figures

Figure 1.1: Crystal structures of calcium oxalate monohydrate (left) and calcium oxalate monohydrate (right) 3

Figure 1.2: Crystal structures of uric acid (P21/n, left) and hydroxyapatite (right). 4

Figure 1.3: Crystal structures of struvite (left) and brushite (right). 5

Figure 1.4: Schematic of laser lithotripsy. 7

Figure 2.1: Images of COM crystals. (a) Agglomerated hexagonal plates of COM. (b) COM hexagonal plates imaged perpendicular to axis used in absorption measurements. Bottom: assorted hexagonal plates under crossed polarizers. 15

Figure 2.2: Uric acid crystals grown by cooling of saturated solutions. (a) Uric acid crystals with square plate and rectangular morphologies. (b) Uric acid image perpendicular to absorption measurement axis. (c) Additional uric acid 16

Figure 2.3: (a) Brushite blades. (b) Brushite crystal imaged perpendicular to axis used for absorption measurements. 17

Figure 2.4: (a) HAp crystals under brightfield illumination. (b) and (c): hydroxyapatite crystals under crossed polarizers with halfwave plate inserted. 17

Figure 2.5: (a) Struvite crystals grown in slowly rotated plastic vials. (b) Struvite crystal imaged perpendicular to axis used for absorption measurements with surface degradation visible. (c) Struvite crystal grown in glass vial; (c) has the same scale as (a). 18

Figure 2.6: (a) COD crystals growing in vial. (b) COD crystal imaged perpendicular to the axis used for absorption measurements. 19

Figure 2.7: Schematic of absorption measurements made by infrared microscope. 21

Figure 2.8: Absorption coefficients for kidney stone minerals. Blue and yellow vertical lines indicate wavelengths of commercial thulium fiber and Ho:YAG laser lithotripters. Adapted from Robinson et al.[53] At Ho:YAG wavelength, the order of minerals in terms of absorption coefficient is struvite > uric acid > COD > COM > brushite. Like the case of COM ablation using Tm fiber (1.91) and Ho:YAG lasers (2.12 μm), the radiant energy required for damage is lower for minerals with higher absorption coefficients with struvite < uric acid < COM.[72] 23

Figure 2.9: Structure of calcium oxalates with water molecules labeled as in Daudon[1] (COM) and Petit (COD).[77] Figure adapted from Robinson et al.[53] 26

Figure 2.10: Crystal structures of brushite (top) and struvite (bottom) with water molecules labeled. Figure adapted from Robinson et al.[53] 27

Figure 2.11: Absorbance comparison between single crystals (dashed line) and DRIFTS (solid lines). 29

Figure 3.1: Normalized Raman spectra for powdered mineral samples from 150-4000 cm^{-1} 40

Figure 3.2: Raman map of a COM kidney stone with region of interest marked by green square. (a) 10 µm spatial resolution map of COM sample (1464 cm^{-1} peak dominant). (b) Region of interest at 1 µm spatial resolution (1464 cm^{-1} peak dominant). (c) 10 µm spatial resolution map of COM sample (1490 cm^{-1} peak). (d) Region of interest at 1 µm spatial resolution (1490 cm^{-1} peak). (e) White light image of COM stone sample. (f) Map of COD at 1 µm spatial resolution in region of interest. 41

Figure 3.3: Example of improper identification of COD by least-squares methods. (a) COM identified by 1464 cm^{-1} peak as in Figure 3.2. (b) COM identified by 1490 cm^{-1} peak as in Figure 3.2. (c) COM identified by spectrum of COM powder. (d) COD identified by spectrum of COD powder. 42

Figure 3.4: Map of a predominantly uric acid stone containing COM lasers using 785 nm laser. (a) Survey map of uric acid at 10 µm spatial resolution. (b) Survey map of COM (1464 cm^{-1} peak). (c) White light image for (a) and (b). (d) 1 µm map uric acid in region of interest. (e) µm map of COM in region of interest. (f) White light image for (d) and (e). 45

Figure 3.5: (a) Survey map of brushite stone. (b) 0.5 µm spatial resolution map at the transition zone from radial-to-compact brushite crystal organization. (c) Concentric ring of apatite growth. 48

Figure 3.6: White light images of the brushite kidney stone fragment mapped in Figure 3.5. 49

Figure 3.7: Map of a majority-struvite (green) kidney stone containing small amounts of apatite (magenta). (a) 10 µm spatial resolution map. (b) White light image of inset in (a). (c) 1 µm spatial resolution map of inset in (a). 50

Figure 3.8: White light images of the struvite stone fragment mapped in Figure 3.7. 51

Figure 3.9: Top: White light image of stone fragment. Bottom: 1 µm spatial resolution map of mixed oxalate and apatite stone fragment. 53

Figure 3.10: Plot showing higher autofluorescence in darker region (i) than in lighter region (ii) of the crystal marked in region (c) Figure 3.9. 54

Figure 3.11: Map of stone fragment containing COD and COM at 0.5 µm spatial resolution. ... 55

Figure 3.12: Raman spectrum of powdered COM in wavenumber region used for mapping..... 57

Figure 3.13: Raman spectrum of powdered COD in wavenumber region used for mapping. 57

Figure 3.14: Raman spectrum of powdered uric acid in wavenumber region used for mapping. 58

Figure 3.15: Raman spectrum of powdered hydroxyapatite in wavenumber region used for mapping..... 58

Figure 3.16: Raman spectrum of powdered COD in wavenumber region used for mapping. 59

Figure 3.17: Raman spectrum of powdered COD in wavenumber region used for mapping. 59

Figure 3.18: Raman spectrum of cyanoacrylate glue, cured and polished. 60

Figure 3.19: Raman spectrum of clear CrystalBond 509, polished. 60

Figure 3.20: Raman spectrum of CrystalBond 509. 61

Figure 3.21: Raman spectrum of acrylic sheet, polished 61

Figure 4.1: 1 J, single-pulse crater volumes for differing plaster formulations. Error bars indicate ±1 standard devation. 68

Figure 4.2: Summary histogram of fragmentation occurrence compared to laser energy required for formulations ($A_{0.60}$, $A_{0.90}$, and $A_{1.20}$). 69

Figure 4.3: Histogram of energy required to fragment stone for formulation A0.60 The number of drilled holes is indicated by color. 70

Figure 4.4: Histogram of energy required to fragment stone for formulation A0.90 The number of drilled holes is indicated by color. 70

Figure 4.5: Histogram of energy required to fragment stone for formulation A1.20 The number of drilled holes is indicated by color. 71

Figure 4.6: Histogram of energy required to fragment stone for formulation A1.79 The number of drilled holes is indicated by color. 71

Figure 4.7: Histogram of energy required to fragment stone for formulation A2.39 The number of drilled holes is indicated by color. 72

Figure 4.8: Histogram of energy required to fragment stone for BegoStone with a 15:3 ratio of powder:water. The number of drilled holes is indicated by color. 72

Figure 4.9: Histogram of energy required to fragment stone for BegoStone with a 15:5 ratio of powder:water. The number of drilled holes is indicated by color. 73

Figure 4.10: Histogram of energy required to fragment stone for phantoms of formulation $B_{2.39}$. The number of drilled holes is indicated by color. 73

Figure 4.11: SEM images of brushite stone and plaster. (a) Human brushite stone. (b) Formulation $B_{2.39}$. (c) Formulation $A_{1.20}$. (d) Image of region of interest indicated in (c). 75

Figure 4.12: High-speed imagery of brushite phantoms fragmenting during laser ablation. (a) Full cross-sectional fracture of formulation $A_{1.20}$. (b) Edge fragmentation of formulation $B_{2.39}$. 76

Figure 5.1: Examples of COM/chitosan composites. (a) Trapped air bubbles alongside craters. (b) Dried composite. (c) Sample from (b) after soaking in water 15 minutes. 81

Figure 5.2: Remapped image of Figure 3.2b,d,f using additional COM orientations. 83

Figure 5.3: Raman spectra of calcium oxalate monohydrate perpendicular to the (100) plane with laser polarization oriented (blue) parallel to the [010] direction and (orange) perpendicular to the [010] direction. 84

Figure 5.4: Raman spectra of calcium oxalate monohydrate perpendicular to the (010) plane with laser polarization oriented (blue) perpendicular to the [001] direction and (orange) parallel to the [001] direction. 85

Figure 5.5: Raman spectra of calcium oxalate monohydrate perpendicular to the (001) plane with laser polarization oriented (blue) parallel to the [010] direction and (orange) perpendicular to the [010] direction 86

Figure 5.6: Schematic and image of flow cells used for artificial stone growth. 88

Figure 5.7: Growth of a mixed COM/COD artificial stone. 89

Figure 5.8: Optical modeling of a vapor bubble generated by a 1 J short pulse from a Ho:YAG laser. 90

Figure 5.9: Overview of parameters impacting ablation. 91

Figure A.1: Raman spectra of COM used for least-squares fitting in Raman maps below. COM 1 was taken normal to the (001) plane with polarization oriented parallel to the [010] axis. COM 2 and COM 3 were taken along the [010] axis parallel and perpendicular to the [001] direction, respectively. 94

Figure A.2: Additional fragment originating from the mixed calcium oxalate and calcium phosphate stone imaged in Figures 3.9 and 3.11. 95

Figure A.3: Additional fragment originating from the mixed calcium oxalate and calcium phosphate stone imaged in Figures 3.9 and 3.11. 96

Figure A.4: Additional fragment originating from the mixed calcium oxalate and calcium phosphate stone imaged in Figures 3.9 and 3.11. 97

Figure A.5 High (0.5 μm) spatial resolution map of fragment originating from the mixed calcium oxalate and calcium phosphate stone imaged in Figures 3.9 and 3.11..... 98

Figure A.6: High (0.5 μm) spatial resolution Raman map of calcium oxalate/phosphate fragment shown in Figure A.4. 99

Figure A.7: Map of struvite stone using a violet (405 nm) laser. Green indicates struvite, while black regions indicate laser damage and burning. The laser is scanned from left to right. In many samples, once damage occurs along a raster line it continues as burned, darkened surfaces absorb more light making damage easier to cause. However, for this struvite sample, damage seems to follow the contours of layering in the stone. This could indicate higher presence of organic matter in the burned areas. This would be a case where observation via fluorescence microscopy prior to Raman mapping may benefit Raman users as regions with higher organic matter could be avoided or scanned with lower laser power. 100

Figure A.8: Example of uric acid stone mapped using a 405 nm laser. 100

Abstract

As pathogenic bioinorganic composites, the formation and destruction of kidney stones is of fundamental and practical interest for materials chemists. The prevalence of urinary calculi has increased in industrialized societies over the past 50 years and today about 1 in 10 people will experience at least one kidney stone in their lifetime. The increase in prevalence has been correlated with dietary changes and the increase in related medical problems like obesity and diabetes. Kidney stones are treated surgically using various forms of lithotripsy with near-infrared, laser-based lithotripsy becoming increasingly favored over older mechanical methods. Despite the common application of near-infrared laser ablation to stone destruction, the mechanisms of laser lithotripsy are poorly understood quantitatively.

This dissertation begins with a focus on quantitative measurement of photothermal properties related to kidney stone decomposition in Chapter 2, particularly the absorption coefficients of kidney stone minerals. To achieve these measurements, new methods for growth of large single crystals of kidney stone minerals were developed. Absorption in the near-infrared region was determined to primarily result from the excitation of the combination vibrational modes of water molecules found within crystal lattices. Peak near-infrared absorption for kidney stone minerals typically occurs in the range of 1.9-2.0 μm aligning well with existing near-infrared laser systems.

Chapter 3 is devoted to understanding kidney stone growth and destruction requiring an understanding of kidney stone structure. Sample preparation techniques were developed to allow

Raman imaging of kidney stone cross-sections and fragments. Sub-micrometer spatial resolutions were achieved in Raman chemical maps revealing previously unobserved features like ≈1 μm thick rings of calcium oxalate monohydrate in uric acid stones that may prevent effective treatment by dissolution. In brushite stones, calcium oxalate crystals were shown to be localized to regions of brushite crystals with specific morphology and may be an indicator of higher stone recurrence risk. Such structural insights become important when designing new artificial kidney stone models for use in urology research.

Many lithotripsy studies have utilized gypsum-based plasters for artificial stone models though gypsum itself does not form kidney stones. Chapter 4 describes new brushite-based plasters developed for use as artificial kidney stone models. These have superior composition and ablation performance compared to gypsum plasters and allowed new studies of the stone ablation process. It was determined that fragmentation of stones occurs on <100 μs time scales, much shorter than the laser pulse length of some lithotripsy systems. Such insights can be use by medical device engineers to improve lithotripter performance.

Chapter 1 Introduction

1.1 Kidney stones as materials

From the view of the materials chemist, kidney stones can be seen as mechanically tough bioinorganic materials composed of pathological mineral crystals with bioorganic molecules interspersed throughout. Crystal morphology and agglomeration patterns on the microscale influence growth and organization of urinary calculi at much larger scales and stones with similar compositions can exhibit large difference in mechanical properties.[1–3] The thermochemical and mechanical properties of stones influence the ability of urologists to treat stones using various forms of lithotripsy – the group of surgeries used to degrade stones into small particles that can pass through the ureteral tract and out the body. With such diverse phenomena involved in the growth and eventual elimination of kidney stones their study benefits from the interdisciplinary approaches of materials chemistry hence this dissertation.

1.2 Kidney stone disease

Kidney stones or, more generally, urinary calculi, are hard deposits of mineral or organic material that form in the urinary tract of humans and other mammals.[4] Kidney stone disease will impact about 1 in 10 people during their lifetime in the United States and other industrialized societies[4] where kidney stone disease has increased in prominence over the past half century.[5] As kidney stone disease is linked to other conditions of increasing concern like metabolic syndrome or diabetes,[6] its burden is likely to rise in the future[7] necessitating a better understanding of growth and treatment to improve patient outcomes.

Six crystalline materials form the majority of kidney stones in humans[4]: calcium oxalate monohydrate (COM), calcium oxalate dihydrate (COD), hydroxyapatite (HAp), uric acid (UA), brushite (calcium hydrogen phosphate dihydrate), and struvite (magnesium ammonium phosphate hexahydrate). Prevalence, chemical formulas, and mineral names of each are included in Table 1. Rarer types of kidney stones can also be formed from pharmaceutical metabolites[8] or cystine[4] though these will not be covered further in this work. Each of the six most common stones is further discussed below.

Table 1.1: Common kidney stone compounds and their prevalence.

Material	Chemical formula	Prevalence (majority component)[4]	Mineral name
Calcium oxalate monohydrate (COM)	$CaC_2O_4 \cdot H_2O$	65 %	Whewellite
Calcium oxalate dihydrate (COD)	$CaC_2O_4 \cdot (H_2O)_{2+x}$ $(0 < x < 0.5)$	11 %	Weddellite
Hydroxyapatite (HAp)	$Ca_{10}(PO_4)_6(OH)_2$	18 %	Hydroxylapatite
Uric acid (UA)	$C_5H_4N_4O_3$	5 %	Uricite
Struvite	$MgNH_4PO_4 \cdot 6(H_2O)$	1 %	Struvite
Brushite	$CaHPO_4 \cdot 2(H_2O)$	1 %	Brushite

1.2.1 Calcium oxalate stones

Calcium oxalate monohydrate, also known as COM or whewellite, is the most common crystalline material found in kidney stones.[4] COM is the most stable and least soluble form of calcium oxalate in saline solution at room temperature[9] although the dihydrate and trihydrate forms can be kinetically favored.[9,10] The most common type of stone, referred to as type 1a in some literature,[1,11] is built by concentric layers of COM that apparently grow slowly and maintain crystallite orientation even as new layers are added.[10,12,13] COM stones are more often associated with high oxalate concentrations in urine, known as hyperoxaluria.[14]

Calcium oxalate dihydrate typically forms crystals with octahedral prism or blade-like morphologies and can rapidly growth to sizes on the order of 100 µm in the kidney.[15] COD is more likely to occur in patients with hypercalciuria – excessive calcium in the urine. In solution, COD will slowly dissolve and reprecipitate as less soluble compounds,[9,16,17] namely COM or hydroxyapatite which are the least soluble minerals of calcium oxalate and calcium phosphate in normal urine.

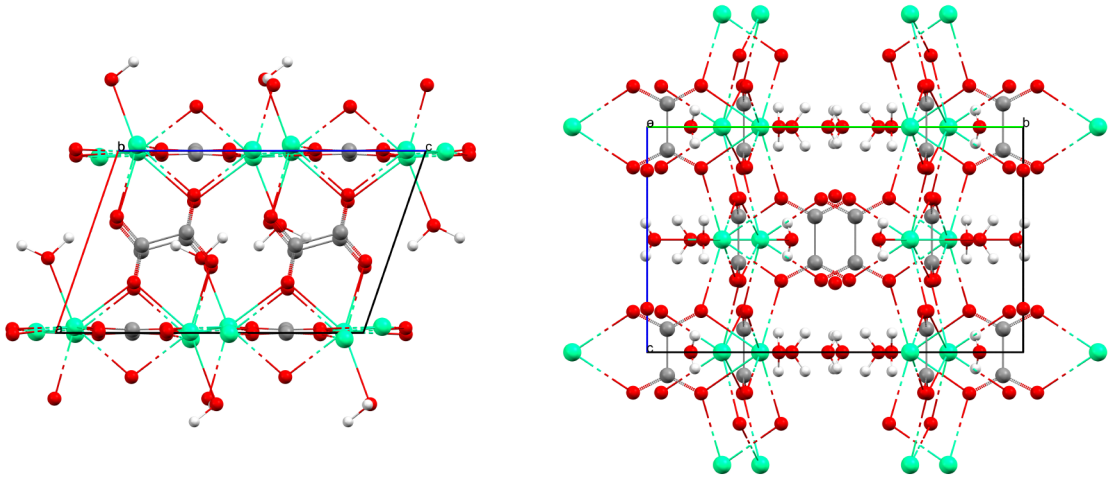

Figure 1.1: Crystal structures of calcium oxalate monohydrate (left) and calcium oxalate monohydrate (right)

1.2.2 Calcium phosphates

Hydroxyapatite is found in a large percentage of stones though it is rarely found as the sole component of larger stones.[4] Benign calcifications within the kidney, known as Randall's plaques, often contain some amount of amorphous calcium phosphate or apatitic calcium phosphate mineral.[18,19] At normal urine pH (5.5-8.5), hydroxyapatite is the most stable form of calcium phosphate[16,17,20] and has the lowest solubility product of all kidney stone minerals in pure water.[21]

Brushite ($CaHPO_4 \cdot 2H_2O$), also referred to as calcium hydrogen phosphate dihydrate (CHPD) or dicalcium phosphate dihydrate (DCPD), is often kinetically favored over apatite though it is the more soluble mineral at physiological pH.[16,22] Brushite stone formation is typically associated with

hypercalciuria or hypocitraturia,[23,24] abnormally low citrate concentration in urine. Both conditions lead to higher calcium activity in urine and are common in the formation of all calcium-containing stones.[25]

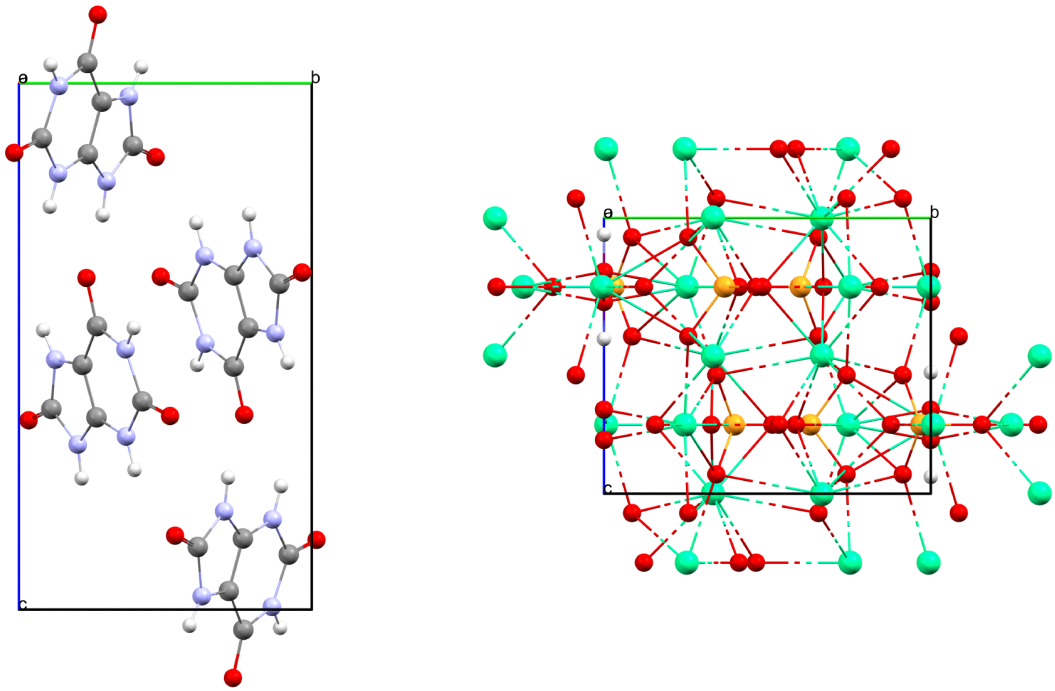

Figure 1.2: Crystal structures of uric acid (P21/n, left) and hydroxyapatite (right).

1.2.3 Uric acid

Uric acid is a purine base found throughout the body with important antioxidant properties in mammalian blood.[26,27] Uric acid solubility decreases sharply below pH 5 which can lead to uric acid precipitation.[28,29] Uric acid stones are often associated with low urine pH and, in some cases, can be treated by raising urine pH through ingestion of citrate or bicarbonate.[30] Sodium and ammonium urate stones may also form in cases of hyperuricosuria (excess uric acid) when urine pH is >5.5.[25] The solubility of sodium and ammonium urates at pH >5.5 are 1-2 orders of magnitude higher than the solubility of uric acid at pH <5.5 which explains the higher likelihood of uric acid stone formation over urate stone formation.[28,29] Uric acid dihydrate is also found in

some stones though it is unstable and converts to anhydrous uric acid in kidneys and in air after stone extraction.[31]

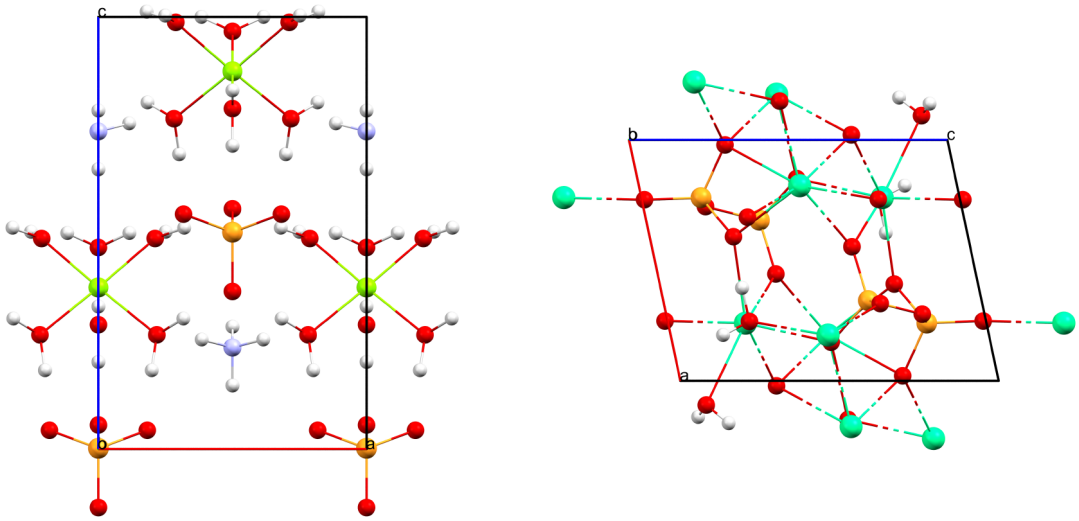

Figure 1.3: Crystal structures of struvite (left) and brushite (right).

1.2.4 Struvite and other infectious stones

Struvite, magnesium ammonium phosphate hexahydrate (MAPH), is unique among kidney stones as it only forms as the result of certain urinary tract infections. Bacteria with urease enzymes hydrolyze urea, the most concentrated component of normal urine, into ammonia and carbon dioxide precipitating struvite as a kinetically favored phase when magnesium, ammonium, and phosphate are available in sufficient quantities.[32] Struvite stones often contain carbonated apatite (carbapatite) which can nucleate simultaneously with struvite or form from its dissolution.[32,33]

1.3 Lithotripsy

Lithotripsy, the class of surgeries for fragmenting urinary calculi, has its origins in devices used to mechanically crush kidney stones.[34,35] During the 1970s, new mechanical treatments utilizing shockwaves were developed into extracorporeal shockwave lithotripsy (ESWL) which

uses focused shockwaves from outside the body to break stones into smaller, passable fragments. While both methods are still used today, laser lithotripsy is increasingly used in treatment of large stones as the focused nature of energy delivery via fiber optic allows stone destruction with lower chances of collateral damage to surrounding tissue.

Laser lithotripsy was originally developed using high-powered ruby or neodymium:yttrium-aluminum-garnet (Nd:YAG) lasers emitting at 1064 nm or lower wavlengths.[34] Unlike modern laser lithotripters, these early lasers destroyed kidney stones through mechanical means as large shockwaves were induced by absorption of high-powered 1064 or 694 nm laser pulses at the surface of kidney stones in water.[34] The high power of the lasers and the relatively low absorption of 1064 or 694 nm radiation by water[36] made such lasers dangerous to operate as collateral damage to surrounding tissues was likely when operators failed to target kidney stones accurately.

In the 1990s, laser lithotripsy using Holmium:YAG lasers emitting at 2.12 μm was developed.[37] Unlike earlier, lower wavelength lasers, it was determined that Ho:YAG lasers ablated stones via a photothermal mechanism.[38,39] This mechanism allows for more effective treatment of mechanically hard stones like dense calcium oxalates that are resistant to shockwave lithotripsy. The relatively high absorption of 2.12 μm radiation by water also reduces the chance of collateral damage to surrounding tissue when lasers are fired off target.[34] Numerous studies have shown that stone recurrence is higher in shockwave lithotripsy than laser lithotripsy making it a more cost effective treatment when available.[40,41] Thus, photothermal laser lithotripsy is increasingly used over mechanical forms of lithotripsy for stone treatment.

Recent developments in the field of photothermal laser lithotripsy include the introduction of thulium-fiber lasers (Tm fiber or TFLs) emitting at 1.94 μm as an alternative to Ho:YAG lasers.[42–44] Thulium fiber lithotripters have advantages in terms of power requirements and compactness

allowing their use in locations that lack the high-voltage electrical systems needed for Ho:YAG systems. Despite the similarity of the two systems in terms of emitted wavelength, Tm fiber lithotripters tend to produce more "dust" than Ho:YAG systems and the advantages of each system are still being explored.[45]

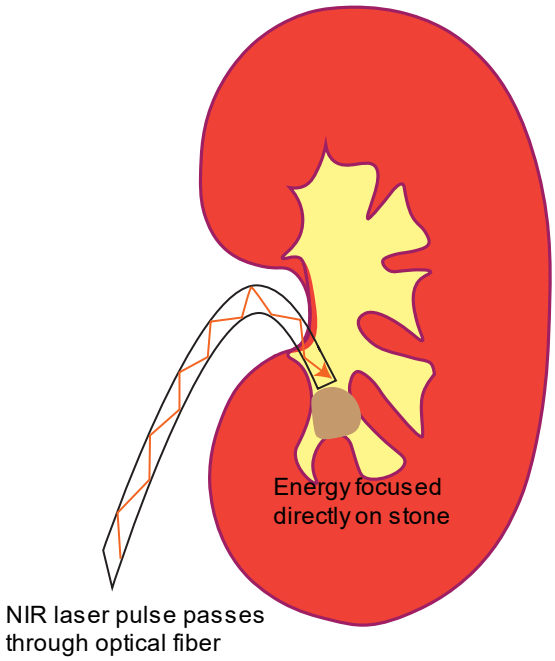

Figure 1.4: Schematic of laser lithotripsy.

1.4 Photothermal laser ablation

Laser ablation of kidney stones begins with the absorption of high-energy laser pulses by urine and urinary calculi. Radiative transfer of laser pulses within these two media is influenced predominantly by two processes: absorption and scattering. For a uniform layer of media, light extinction with depth can be modeled with the following equation:

$$I(z) = I_0 e^{-(k_a + k_s)l}$$

where l is path length, $I(l)$ is radiation intensity along the path l, I_0 is intensity at $l = 0$, k_a is the absorption coefficient of the medium, and k_s is the extinction coefficient due to scattering. At body temperatures, intensity contributions from thermal emissions are expected to be much lower than

the intensity contributions from laser pulses allowing emission to be ignored in this simplified model of light extinction.

Infrared absorption occurs due to changes in vibrational frequency that result in a change of dipole moment in molecules. In most cases, the first excited vibrational state is separated from the ground vibrational state by 100-4000 cm^{-1}, equivalent to photons with wavelengths of 100-2.5 μm (3-120 THz). Both the Tm fiber and Ho:YAG lasers used in laser lithotripsy emit at lower wavelengths of 1.94 and 2.12 μm, respectively. Thus, the excitement of vibrational states by these lasers is expected to be primarily driven by overtones modes or combination modes. Overtone modes refer to changes in vibrational quantum number $\Delta v > 1$. These transitions are forbidden under the harmonic approximation of molecular vibration and are typically weaker as Δv increases. Combination modes involve simultaneous transitions in two vibrational modes such as the bending and stretching modes of a water molecule. Combination modes also tend to be less intense than fundamental vibrational modes.

1.5 From crystals to kidney stones

Crystallization in biological systems often deviates from classical crystallization theory due to factors ranging from amorphous precursor formation to face-specific adsorption of biomolecules on growing crystals. Classical crystallization theory, which was developed from the study homogeneous nucleation and growth of vapor droplets in air, uses relative saturation ratio to describe the thermodynamic driving force for crystal nucleation and growth[46,47]:

$$S = \frac{\prod_{i=1}^{n} c_i}{k_{sp}}$$

where S is the saturation ratio, c_i is the concentration of a species in solution, and k_{sp} is the solubility product of the crystal. When the saturation ratio is >1, crystals are expected to grow while crystals

are expected to dissolve when the saturation ratio is <1. In classical theory, smaller crystals or clusters of ions or molecules have higher effective supersaturation than larger particles. From a chemical standpoint, this can be understood by considering the number of fully bonded species within a crystal in comparison to partially bonded species at the crystal surface. This creates a thermodynamic barrier requiring supersaturation >1 for homogenous crystal nucleation. Interested readers can find further discussion of classical nucleation and growth in existing literature.[47]

In biological systems, there are often large deviations from the equilibrium concentration picture provided by classical nucleation theory. For example, in urine, cation concentrations do not correlate well with their activity due to presence of biomolecules that complex with calcium or magnesium. Similarly, oxalate activity with respect to calcium oxalate formation can be decreased by presence of divalent or trivalent cations other than calcium. A more accurate representation of (super)saturation requires use of activity rather than concentration which is difficult to determine in complex systems like urine.

Calcium minerals commonly found in biological systems like calcium carbonates and calcium phosphates are known to form phase-separated liquid or amorphous solid precursors prior to conversion to crystalline phases.[46] Such amorphous phases are believed to form initially as ion clusters in solution. Similar clusters are known to form between oxalate and calcium which can lead to metastable amorphous calcium oxalate in aqueous or alcohol solutions.[48–50] Small molecules like citrate and some polymers seem to encourage formation of phase-separated, amorphous liquids on the nanoscale forming what are known as polymer-induced liquid precursors (PILPs).[46,48,51] These precursors can spontaneously convert to crystal phases on their own or when they come in contact with existing crystalline solids that provide a surface for heterogeneous nucleation.

In addition to growth by agglomeration of unoriented particles, kidney stones may also grow via oriented attachment of nanocrystals. Oriented attachment can occur due to stronger attractions between specific crystal faces leading to organized aggregation.[46] In the case of minerals that have charged faces like COM, nanocrystals near the surface of a growing stone may reorient to align oppositely charged (100)[52,53] faces before attachment leading to organized crystal growth. Nanocrystals may fuse after attachment leading to formation of single crystals despite growth by aggregation.[54] With amorphous calcium phosphate and calcium oxalate expected in urine, various crystallization nucleation and growth mechanisms, both classical and nonclassical, are likely active simultaneously.[55] Classical growth, liquid and amorphous solid precursors, and oriented attachment will used to explain potential mechanisms of kidney stone growth in the following chapters.

1.6 Outline of dissertation

This dissertation covers a broad range of experiments and topics that have been performed and studied to better understand kidney stone growth and destruction. Though many empirical studies have been performed with Tm fiber and Ho:YAG lasers, little research has attempted to understand the underlying physicochemical properties that lead to photothermal ablation of kidney stones. Chapter 2 focuses on the development of a more quantitative understanding of photothermal laser ablation. Most work focuses on the measurement of absorption coefficients of kidney stone minerals with related development of crystallization methods for 10-1000 μm scale mineral single crystals. The origin of NIR absorption by kidney stone minerals is discussed in detail with NIR peaks attributed to specific water molecules and bonds within kidney stone minerals.

Understanding stone growth and structure is essential for the development of non-surgical interventions and prevention of kidney stone formation. Chapter 3 focuses on the use of Raman

chemical imaging to study the microstructure of kidney stones and relates structural observations to potential growth conditions. The development of better sample preparation techniques allowed use of Raman lasers that normally cause excessive autofluorescence in kidney stone samples enabling imaging on spatial scales ≤1 μm. Raman imaging revealed previously unobserved structures within kidney stones with potential consequences relating to dissolution therapy of uric acid stones and recurrence in calcium phosphate stones.

Chapter 4 focuses on the development of artificial brushite kidney stone models and their characterization. Unlike previous artificial models, these brushite plasters fracture like human stones which demonstrating that fracture likely occurs in <100 μs under laser irradiation, a time period much shorter than the pulse length of some Tm fiber lithotripters.

Avenues for future research at the interface of chemistry and urology are discussed in Chapter 5. Preliminary work with promising artificial models formed from struvite plaster or chitosan/COM composites is described along with efforts to grow kidney stones in vitro. Orientation effects of calcium oxalates on Raman spectra are discussed with potential applications to future structural studies of kidney stones. Finally, ideas for computational modeling of kidney stone destruction are briefly discussed for urologists, scientists, and engineers who are interested optimizing laser lithotripters in the future.

Chapter 2 Photothermal Properties of Kidney Stone Minerals^

2.1 Introduction

Despite nearly 30 years of clinical use, a quantitative understanding of the ablation of kidney stones by Ho:YAG lasers remains poorly developed. Most evidence points to a photothermal mechanism of ablation in which the mineral components of kidney stones absorb near-infrared (NIR) radiation, heating stones until decomposition occurs.[38,39,56,57] Evidence for the photothermal mechanism over mechanical destruction by cavitation includes heat-induced chemical changes,[38,39,56,58] high-speed imagery of ablation prior to cavitation,[59] stone ablation in air,[39] and lower ablated volumes when H_2O is substituted by D_2O in stones.[57]

To understand laser lithotripsy quantitatively, it is first necessary to understand irradiance at the stone surface. Laser radiation is absorbed by both water and the stone itself with a vapor bubble forming on the scale of 10-100 μs[59] thus requiring a quantitative understanding of bubble dynamics to fully model the ablation process. At the stone, surface heating and decomposition are dependent on the stone's absorption of radiation and specific heat capacity. Eventual destruction can occur via several processes: mineral decomposition, inclusion vaporization, and/or thermal stress. Mineral decomposition is known to take place during laser lithotripsy as thermal decomposition products can be found post-ablation.[56,58] As chemical evidence suggests heating beyond 100 °C,

^ Adapted from:
Robinson, J. W.; Ghani, K. R.; Roberts, W. W.; Matzger, A. J. Near-Infrared Absorption Coefficients in Kidney Stone Minerals and Their Relation to Crystal Structure. *J. Phys. Chem. C* **2023**, *127* (1), 759–767. https://doi.org/10.1021/acs.jpcc.2c07475.

any urine inclusions within kidney stones are likely vaporized as well leading to localized pressure increases that will induce strain which can lead to mechanical failure. Thermal expansion may also play a role in stone fracture though this idea remains unexplored.

A thorough understanding of many chemical and physical properties is necessary to model kidney stone ablation dynamically. Prior to my research, literature sources had only observed NIR absorption spectra of kidney stones using highly scattering samples preventing absorption coefficient comparison among different minerals.[57,60] This chapter focuses on absorption coefficient measurements made for the most common minerals found in kidney stones: calcium oxalate monohydrate (COM), calcium oxalate dihydrate (COD), hydroxyapatite (HAp), uric acid, struvite, and brushite. The absorption coefficient of gypsum, which is found in BegoStone plaster models of kidney stones, was also measured and compared favorably to literature values (Table 2.1). Absorption coefficient measurements were performed using single crystals to avoid complications from multiple scattering. Water bending + stretching combination modes were determined to be the primary contributors to NIR absorption in the 1.8-2.2 μm region where laser lithotripters operate. Absorption peaks in this region are attributed to specific water molecules and bonds within crystal lattices when possible. Absorption coefficients were significantly different between Ho:YAG and thulium fiber wavelengths though additional factors seem to ultimately drive ablation in artificial stone models.

2.2 Methods

2.2.1 Crystal growth

To measure absorption coefficients while reducing contributions from scattering it was necessary to grow large crystals of the various minerals found within kidney stones. Crystals for infrared microscope measurements require at least two flat, parallel faces with transverse

dimensions >30 μm. This allows the IR beam with a square aperture of 15 μm to pass through the crystal with a low chance of refracting through the sides of the crystal which would lead to erroneous extinction measurements. Detailed methods for symmetric growth of single crystals for COM, COD, hydroxyapatite, uric acid, brushite, and struvite are described below. Images of crystals can be seen in Figures 2.1-2.6.

2.2.1.1 Calcium oxalate monohydrate

Hexagonal plates of COM (Figure 2.1) were prepared by adding 25 μL of liquid dimethyl oxalate (85 °C) to a 20 mL aqueous solution of 2 M NaCl and 5 mM $CaCl_2$ in a 20 mL borosilicate scintillation vial. Dimethyl oxalate that solidified on contact with aqueous solution was dissolved by sonication. Vials were capped and placed in convection ovens set to 37 °C for one week to allow hexagonal plates to form.

The high ionic activity provided by 2 M NaCl serves as inhibitor of growth in the [100] direction of COM crystals as the high ionic strength solution interferes with charged oxalate/water or Ca^{2+}/oxalate layers along this direction.[52,53] Slow release of the oxalate ion via dimethyl oxalate hydrolysis serves to limit nucleation allowing larger COM crystals to grow. Lower concentrations of NaCl may be used to growth thicker hexagonal plates though there is an increase in agglomeration and twinning.

2.2.1.1 Uric acid

Anhydrous uric acid (Figure 2.2) was prepared through dissolution in boiling water followed by incremental decreases in temperature over the course of 5-10 days. An excess of commercial uric acid powder was dissolved in 150 mL deionized water stirred in an Erlenmeyer flask. Heated uric acid solution was filtered through 0.45 μm nylon syringe filters into 20 mL borosilicate scintillation vials placed in a 95 °C heat block. For large crystals with up to 1 mm length and width,

vials were cooled in increments 5 °C/day without agitation. Smaller crystals can be prepared using larger daily increments of temperature change.

2.2.1.1 Brushite

Large brushite crystals (Figure 2.3) were prepared by mixing equal volumes of 300 mM NaH_2PO_4 and 300 mM $CaCl_2$. Crystals were allowed to grow for 1-3 days at room temperature, often forming bundles of needles and blades originating from a central point. Plates from these mixtures have lengths on the order of millimeters with widths reaching up to one millimeter.

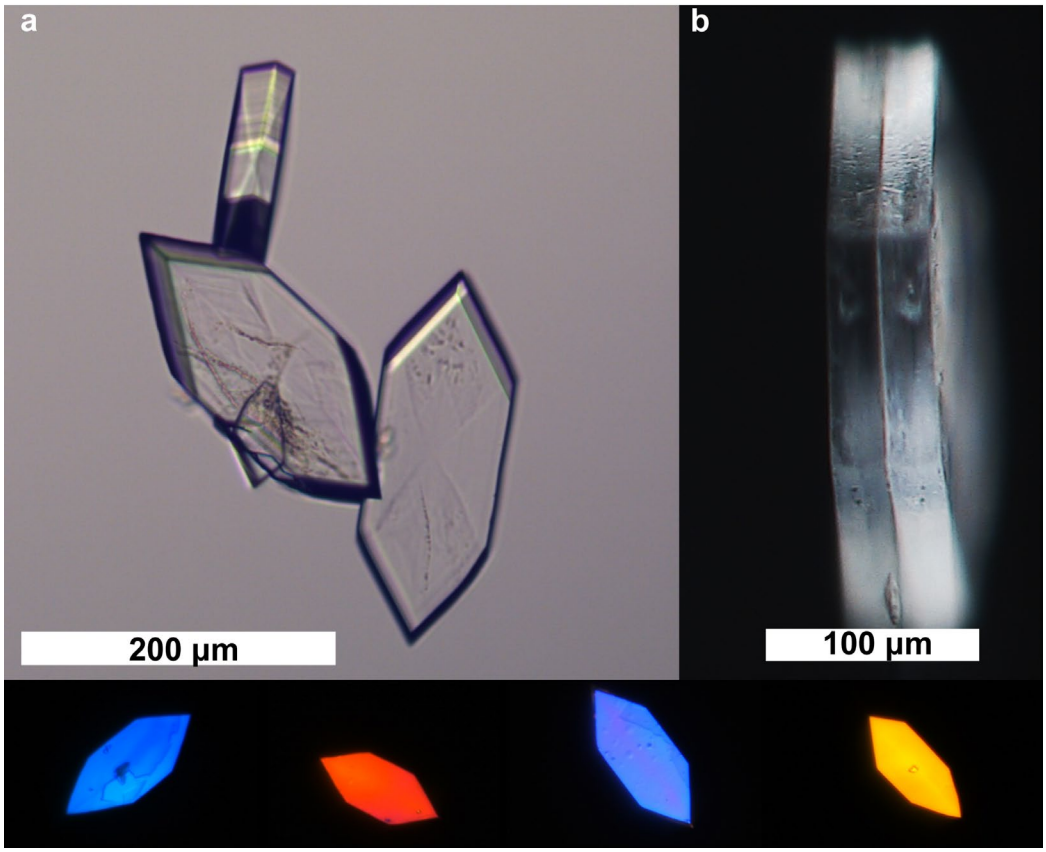

Figure 2.1: Images of COM crystals. (a) Agglomerated hexagonal plates of COM. (b) COM hexagonal plates imaged perpendicular to axis used in absorption measurements. Bottom: assorted hexagonal plates under crossed polarizers.

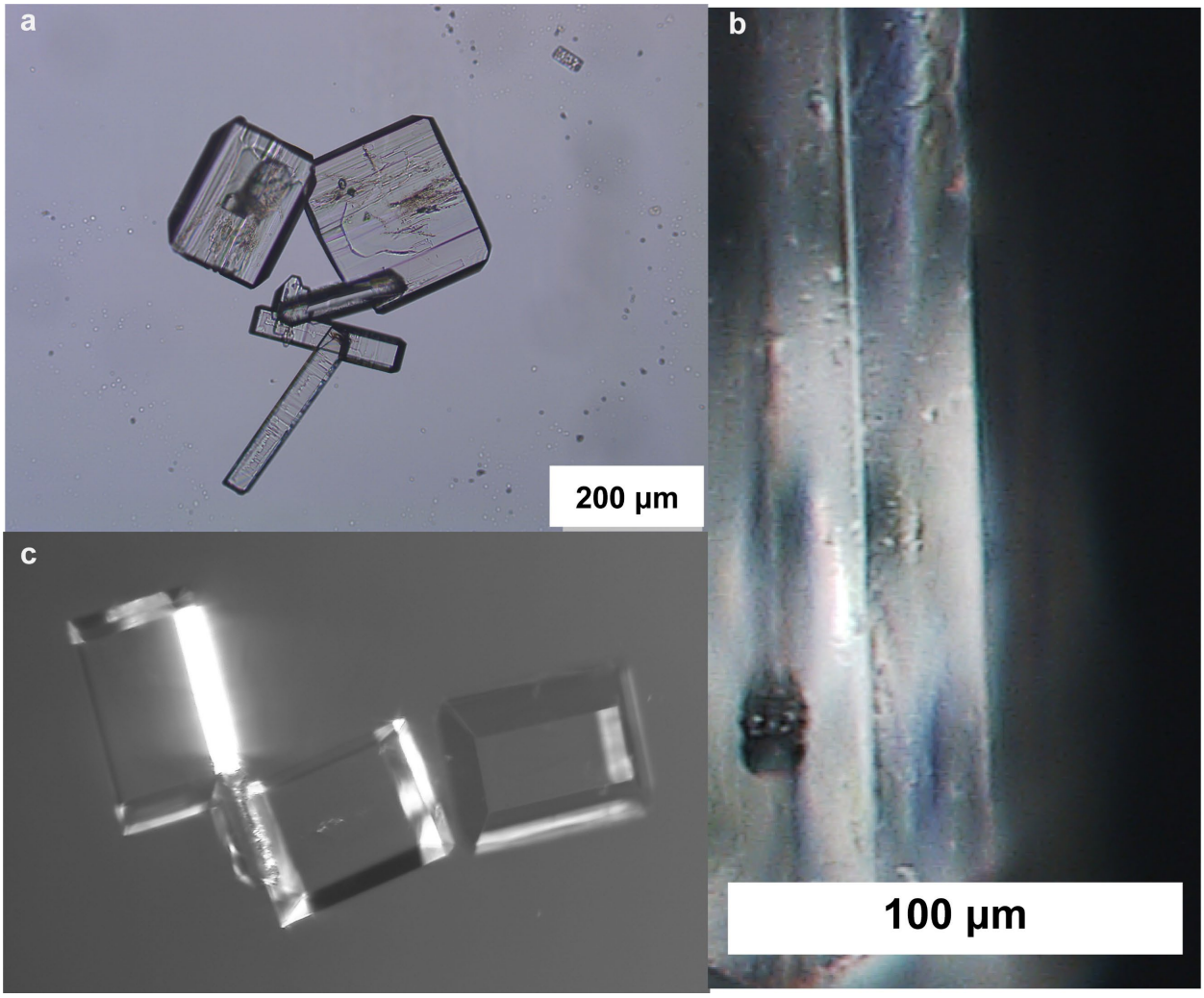

Figure 2.2: Uric acid crystals grown by cooling of saturated solutions. (a) Uric acid crystals with square plate and rectangular morphologies. (b) Uric acid image perpendicular to absorption measurement axis. (c) Additional uric acid

2.2.1.1 Hydroxyapatite

Apatite crystals (Figure 2.4) were grown by recrystallization in molten salt using a method adapted from literature.[61] Commercial hydroxyapatite powder was mixed with potassium sulfate in a 1:4 mass ratio. Mixtures were ball milled at 30 Hz for 10 minutes to achieve intimate contact between the K_2SO_4 flux and the hydroxyapatite. Milled powders were placed in alumina crucibles which were placed in a tube or muffle furnace. Furnaces were heated at a rate of 5 °C/minute to a temperature of 1050 °C, held at 1050 °C for 12 hours, and rapidly cooled to 800 °C. This rapid cooling freezes the molten salt quickly resulting in higher quality crystals compared to slow

cooling. Below 800 °C temperature was reduced gradually at 5 °C/min to prevent damage to equipment from thermal shock. Water was used to dissolve remaining K_2SO_4 and larger apatite crystals were chosen for infrared measurements.

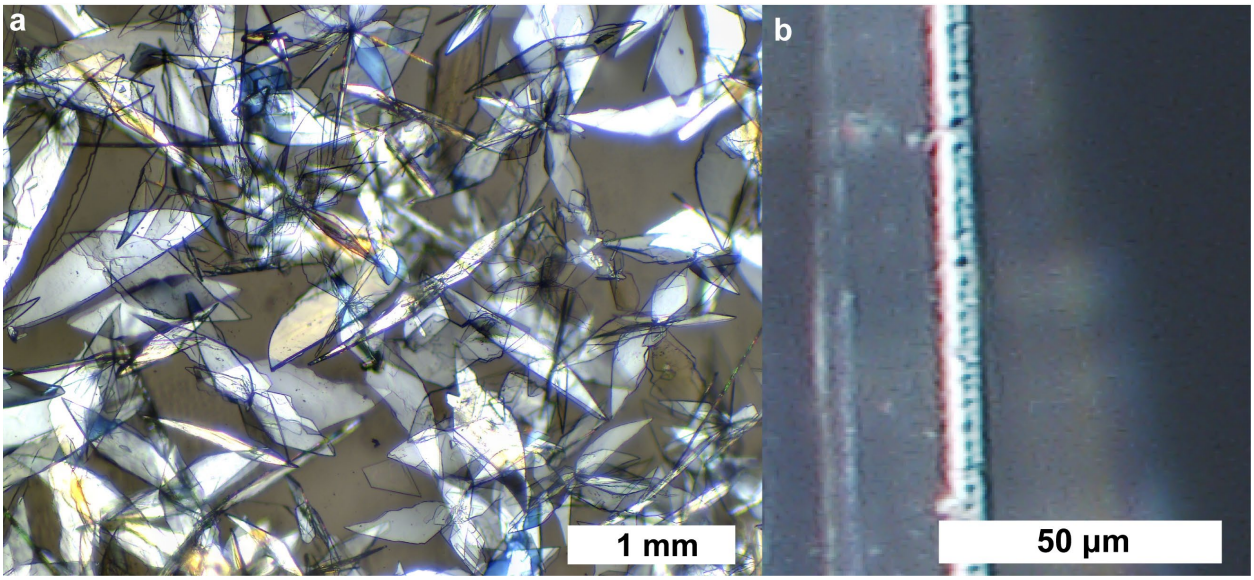

Figure 2.3: (a) Brushite blades. (b) Brushite crystal imaged perpendicular to axis used for absorption measurements.

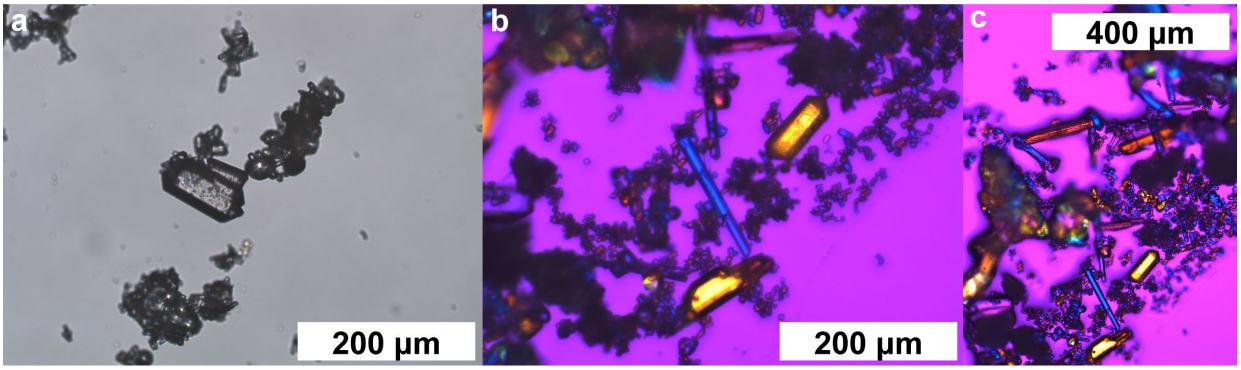

Figure 2.4: (a) HAp crystals under brightfield illumination. (b) and (c): hydroxyapatite crystals under crossed polarizers with halfwave plate inserted.

2.2.1.2 Struvite

Struvite crystals with flat, parallel faces (Figure 2.5) were prepared by mixing 40 mM $MgCl_2$, deionized water, and 40 mM $(NH_4)_2HPO_4$ in a 1:3:1 volume ratio, typically 5 mL, 15 mL, and 5 mL, respectively. The mixed solution was poured into 20 mL plastic vials completely filling the

vials to minimize air bubble size. Vials were capped and placed on rollers for gentle rotation. Crystals were selected after 24 hours. Use of plastic vials and gentle rotation prevent attachment of crystals to the vial which leads to the asymmetric "coffin" growth habit often observed in literature preparations of struvite.[62] Air bubble minimization serves the same purpose as small crystals often localize to the air-water interface.

Larger struvite crystals without flat, parallel faces can be grown using 10 mM $MgCl_2$ and 10 mM $(NH_4)_2HPO_4$ mixed in equal parts in glass vials at room temperature. Under these conditions, struvite typically nucleates on the glass walls of the vials leading to asymmetric growth but thick crystals reaching 1 mm in length can be grown for polishing (Figure 2.5c).

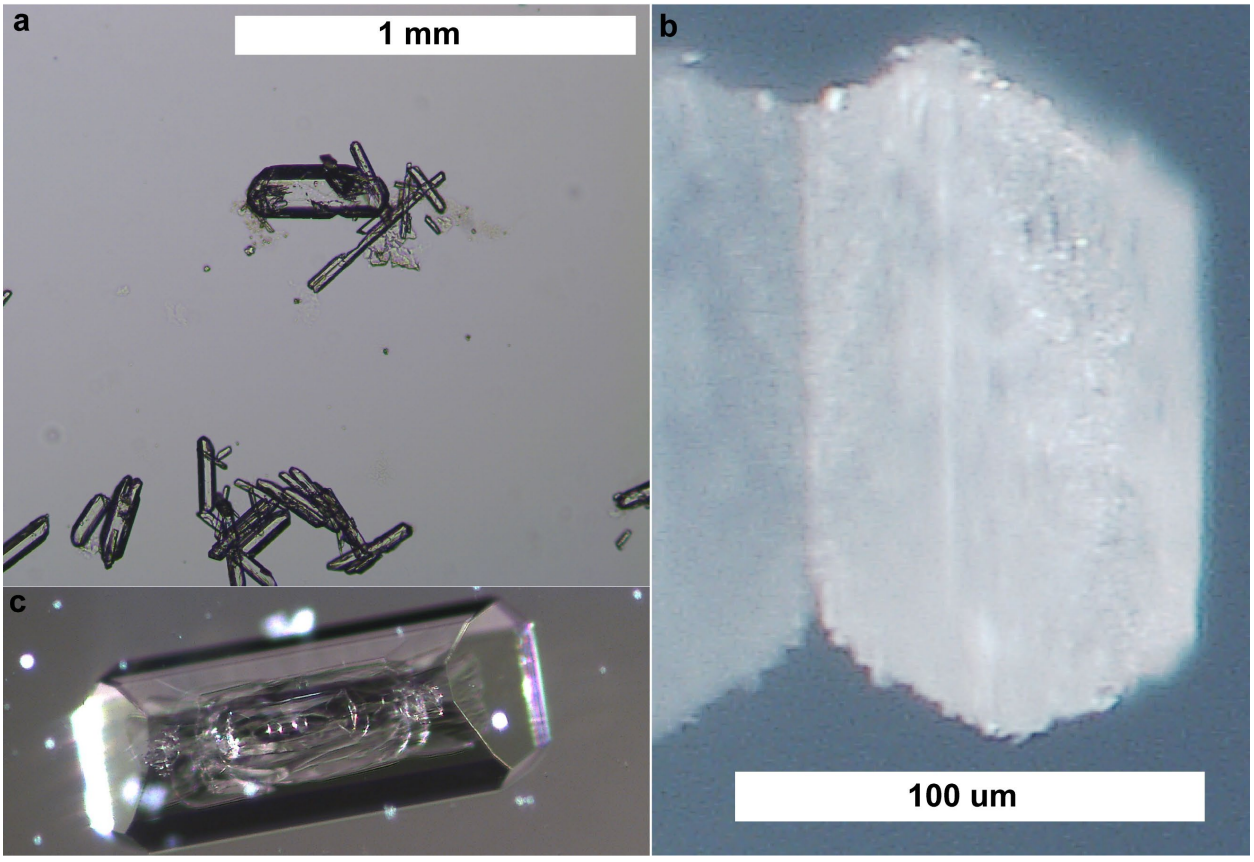

Figure 2.5: (a) Struvite crystals grown in slowly rotated plastic vials. (b) Struvite crystal imaged perpendicular to axis used for absorption measurements with surface degradation visible. (c) Struvite crystal grown in glass vial; (c) has the same scale as (a).

2.2.1.3 COD

COD crystals typically form octahedral prisms in aqueous solution containing oxalate and calcium which are unsuitable for IR microscopy.[63,64] To induce a morphology change to elongated octahedral prisms, polyacrylic acid may be used as it preferably binds to the <100> planes of COD.[63,64] Crystallization was accomplished by adding 0.8 mL 10 mM sodium oxalate, 1 mL 10 mM sodium pyrophosphate, 0.2 mL of 1 wt.% polyacrylic acid (11000 g M_w), and 17.2 mL deionized water to a 20 mL glass scintillation vial. These solutions were thoroughly mixed prior to addition of 0.8 mL 10 mM $CaCl_2$ for crystallization. The 20 mL scintillation vials were left uncapped and placed in a large crystallization dish containing a saturated solution of NaCl. The crystallization dish was covered with aluminum to reduce evaporation providing a ≈75% relative humidity[65] environment for slow evaporation from the vials containing the COD crystallization solution. COD crystals were allowed to grow undisturbed for at least 1 week.

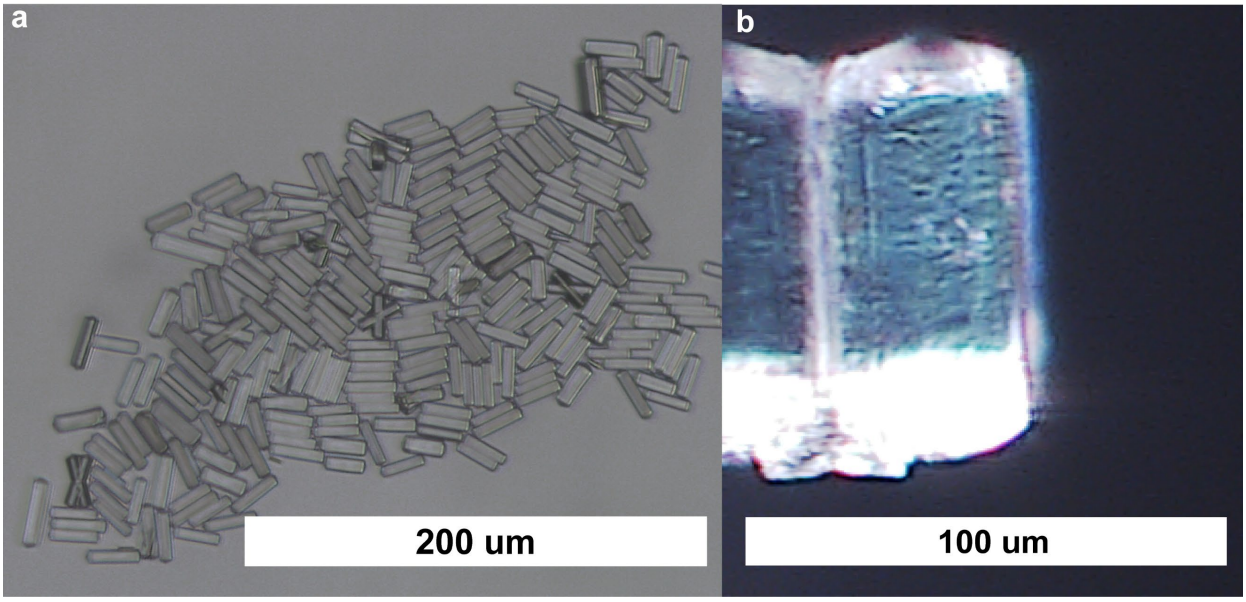

Figure 2.6: (a) COD crystals growing in vial. (b) COD crystal imaged perpendicular to the axis used for absorption measurements.

Sodium pyrophosphate in this solution serves to inhibit COM nucleation its presence will decrease calcium and oxalate concentrations below saturation with respect to COD.[9,66] COD

crystals grown in this fashion reach ≈100 μm in length but only tens of micrometers in width. Larger crystals of COD that fuse into serrated blade-like structures may be grown from artificial urine as an alternative to the above method. The conditions for this type of growth are covered in Chapter 5.

2.2.1 Absorption coefficient measurements

For absorbance measurements, mineral single crystals were placed on copper transmission electron microscopy (TEM) grids with mesh sizes of 600 or lower (hole size >30 μm) with TEM grids glued to custom acrylic holders. Near-infrared absorption was measured using a Thermo-Nicolet iN10 infrared microscope using the liquid nitrogen cooled mercury-cadmium-tellurium (MCT) detector. The microscope aperture was set to a 15 by 15 μm square to ensure the infrared beam passed through the mineral single crystals and the copper TEM grids on which they were mounted. The aperture was rotated as needed. Absorbance measurements were carried out with the visible-light camera of the IR microscope focused on the bottom of each crystal where IR light enters the sample in transmission mode (Figure 2.7). Near-infrared spectra were collected at 4 cm^{-1} resolution from 4000-7000 cm^{-1}. The baseline from reflection and refraction for each absorption spectrum was removed using a linear function.

To determine absorption coefficients from absorbance measurements, crystals were transferred from the copper TEM grids to glass slides for crystal thickness measurements. Crystal thicknesses were measured using a Hirox RH-2000 digital microscope tilted 90° with respect to the crystal axis along which absorption was measured. The crystallographic axes along which absorption coefficient measurements were made are listed in Table 2.1.

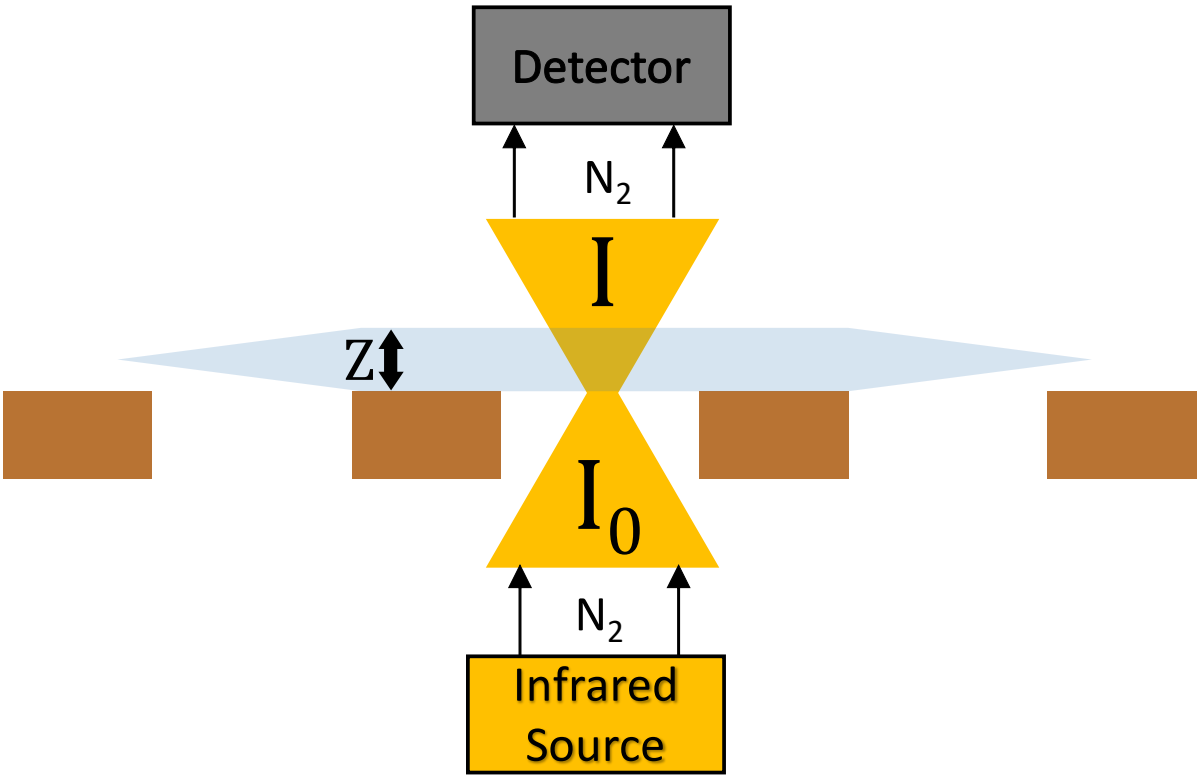

Figure 2.7: Schematic of absorption measurements made by infrared microscope.

2.2.2 Diffuse reflectance measurements

Diffuse reflectance infrared Fourier transform spectroscopy (DRIFTS) was used to measure isotropic absorbance of mineral powders. DRIFTS was performed with a Harrick Praying Mantis diffuse reflectance attachment for a Thermo-Nicolet iS50 infrared spectrometer. Samples were prepared by mixing mineral powders with mass fractions of 0.001-0.01 with potassium bromide. KBr powder was sieved to select for grain sizes between 45 and 75 μm. At sizes greater than ≈20 μm, scattering by the KBr powder primarily follows principles of geometric optics rather than Rayleigh scattering or Mie scattering allowing an assumption of wavelength-independent scattering for KBr powder.

2.3 Results and discussion

Table 2.1: Absorption coefficients at commercial thulium fiber (k_{TF}, 1.94 μm) and Ho:YAG ($k_{Ho:YAG}$, 2.12 μm) laser lithotripter wavelengths along the directions indicated.

Compound	Perpendicular face(s)	$k_{TF} \pm 1\sigma$ / mm^{-1} (λ = 1.94 μm)	$k_{Ho:YAG} \pm 1\sigma$ / mm^{-1} (λ = 2.12 μm)
COM	{100}[19,25,26]	3.5 ± 0.2	1.08 ± 0.08
COD	{100}[20,21]	6.5 ± 0.6	1.7 ± 0.2
HAp	{100}	0.0 ± 0.2	0.0 ± 0.2
Uric acid	{001}[27] (for P21/n)	0.3 ± 0.1	1.8 ± 0.1
Struvite	Unknown/various	3.2 ± 0.3	7.9 ± 0.6
Brushite	{010}[28]	2.83 ± 0.08	0.42 ± 0.06
Gypsum (this work)	{010}	3.8 ± 0.4	0.8 ± 0.2
Robertson et al.[67]	Powder reflectance (spherical particle model)	6.8	0.7
Roush et al.[68]	Diffuse powder reflectance	3.2	0.6
Ye et al.[69]	Multiple angle reflectance	3.3	0.7
Water (liquid)[30]	-	14	3

Absorption coefficients in the region of interest are shown in Figure 2.8 and listed in Table 2.1. Comparisons to diffuse reflectance spectra are shown in Figure 2.11. Welch's two-tailed t-test was used for statistical comparison of absorption coefficients. Absorption coefficients were considered significantly different for $p < 0.05$.

2.3.1 Comparing absorption at different laser wavelengths

Excluding struvite, water-bearing minerals have higher absorption for Tm fiber lasers (1.94 μm) than Ho:YAG lasers (2.12 μm). This matches the absorption patterns for both liquid water[36,70] and ice[71] suggesting the absorption features observed are primarily the result of absorption by water bending + stretching combination modes.[53] Struvite and anhydrous uric acid both absorb more strongly at 2.12 μm than 1.94 μm; though struvite contains water, stronger hydrogen bonding appears to shift struvite absorption to longer wavelengths as discussed below.

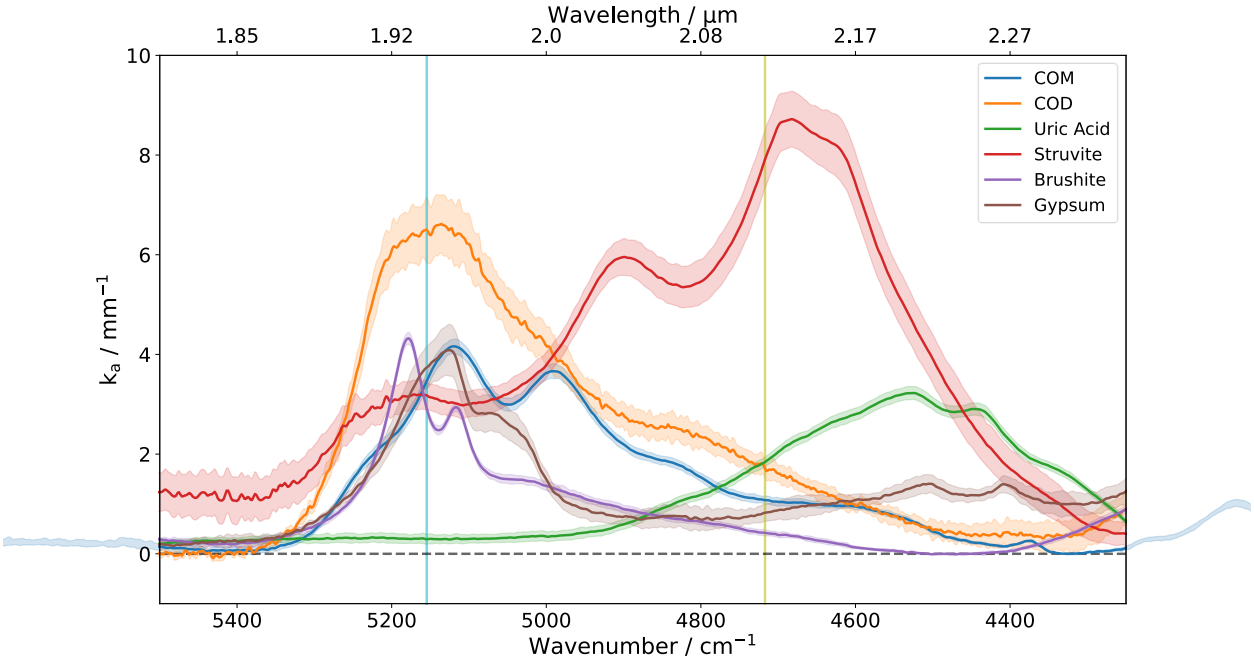

Figure 2.8: Absorption coefficients for kidney stone minerals. Blue and yellow vertical lines indicate wavelengths of commercial thulium fiber and Ho:YAG laser lithotripters. Adapted from Robinson et al.[53]At Ho:YAG wavelength, the order of minerals in terms of absorption coefficient is struvite > uric acid > COD > COM > brushite. Like the case of COM ablation using Tm fiber (1.91) and Ho:YAG lasers (2.12 μm), the radiant energy required for damage is lower for minerals with higher absorption coefficients with struvite < uric acid < COM.[72]

For commercial thulium fiber systems emitting at 1.94 μm the absorption strength order is COD > COM ≈ struvite ≈ gypsum > brushite > uric acid. The higher absorption in COD is expected from its higher water molecule density/volume in the crystal lattice. The relatively high standard deviation in COD absorption coefficient (±0.6 mm^{-1}) is likely due to the variable amount of uncoordinated water found within its channel structure. COM, struvite, and gypsum have similar absorption coefficients that are not significantly different. Brushite is only slightly lower while the absorption coefficient of uric acid is an order of magnitude lower than other compounds.

At 2.12 μm, compounds from most absorbing to least absorbing are struvite > uric acid ≈ COD > COM ≈ gypsum > brushite. Struvite has higher absorption due to stronger hydrogen bonding which is correlated with a peak shift to lower energy among water-bearing minerals.[73–75] The

higher strength of absorption in COD than other minerals likely results from the higher density of water in its structure compared to COM, brushite, or gypsum.

The radiant energy density (J/cm^2) required to ablate COM stones is known to be ≈4 times higher for Ho:YAG lasers compared to research-grade Tm fiber lasers emitting at 1.908 μm.[76] Additionally, at 2.12 μm, ablation thresholds were shown to be lower for struvite < uric acid < COM.[72] In both examples, the ablation threshold is inversely related to the measured absorption coefficient suggesting absorption coefficients are a good predictor of damage onset in kidney stones.

Though ablation thresholds are lower for lasers emitting in mid-infrared region with wavelengths >2.5 μm,[72] a lack of flexible fibers able to deliver energy within the urinary tract prevents adoption of systems such as Er:YAG lasers that emit at 2.83 μm. The absorption of NIR light by water and water-bearing minerals is near its peak at the 1.94 μm wavelengths offered by Tm fiber lasers. Thus, from the perspective of causing kidney stone ablation at the lowest possible radiant energy densities, Tm fiber lasers are likely the ideal choice given current fiber technologies. In surgical practice, lasers are often fired with optical fibers at a 0.5-1 mm standoff distance from a stone's surface meaning NIR lasers may be more practical than MIR lasers as pulse attenuation within water is less significant in the NIR allowing more light absorption at the stone surface prior to bubble formation and contact.

2.3.2 Assignment of near-infrared peaks to vibrational modes

NIR absorption peaks from 4500-5500 cm^{-1} are typically caused by the combination of water bending (≈1650 cm^{-1}) + stretching peaks (≈3500 cm^{-1}) for water-bearing materials. The peak absorption for liquid water in this region varies with temperature from 5130-5250 cm^{-1} (1.95-1.90 μm) with the peak shifting to higher frequencies as temperature increases due to decreasing

influence of hydrogen bonding on molecular vibrations.[70] Prior combined computational and experimental work has provided in-depth analysis of the vibrational modes for calcium oxalates,[77] brushite,[78] and struvite.[79] Mid-infrared absorption peaks in anhydrous uric acid had not been assigned definitely in the literature.

The NIR spectrum for COM has two stronger peaks at 5115 and 4990 cm^{-1} with shoulders near 5200, 4820, and 4620 cm^{-1} which likely correspond to the five water stretching modes in the mid-IR spectrum.[77,80] The combination peak near 4615 cm^{-1} likely results from $\nu_a O(1) - H(1) + \delta H_2 O(1)$ as the O(1)-H(1) bond is 0.990 Å (Figure 2.9) which is longer than most OH bonds in minerals other than struvite and likely contributes to the higher absorption coefficient of COM for Ho:YAG lasers compared to brushite or gypsum

COD has two waters in its crystal structure along with disorganized water adsorbed within channels (Figure 2.9). The NIR water peak is centered at 5150 cm^{-1} for COD and is expected to primarily originate from the combination modes of the lattice waters which have a broad stretching mode peak centered near 3500 cm^{-1} and bending mode peaks near 1640 cm^{-1}. The room temperatures position of the HOH bending mode has not been determined for COD as it cannot be distinguished from the stronger carboxylate stretching peak.[77,80] The peak positions of disordered waters have not been determined.

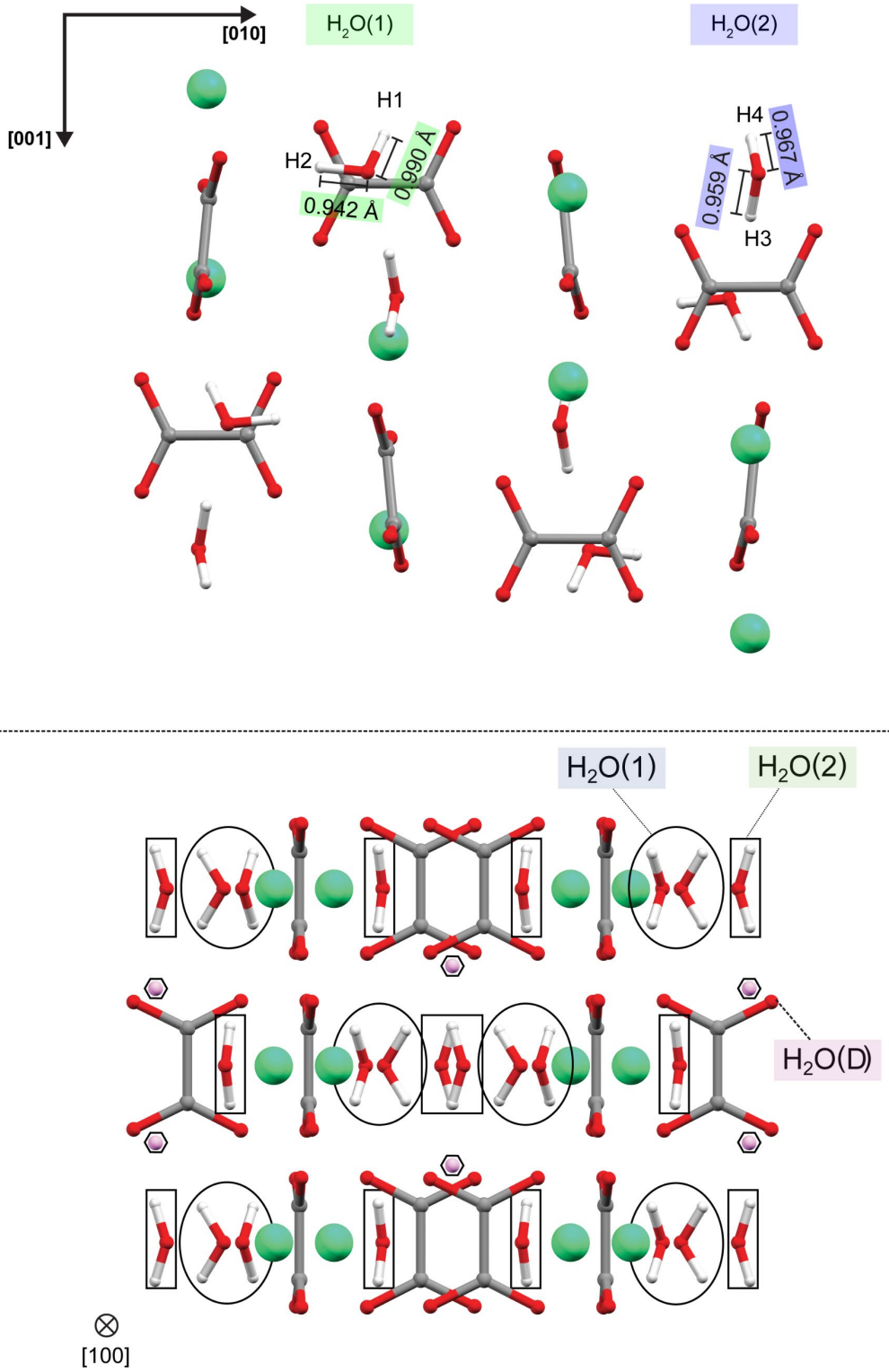

Figure 2.9: Structure of calcium oxalates with water molecules labeled as in Daudon[1] (COM) and Petit (COD).[77] Figure adapted from Robinson et al.[53]

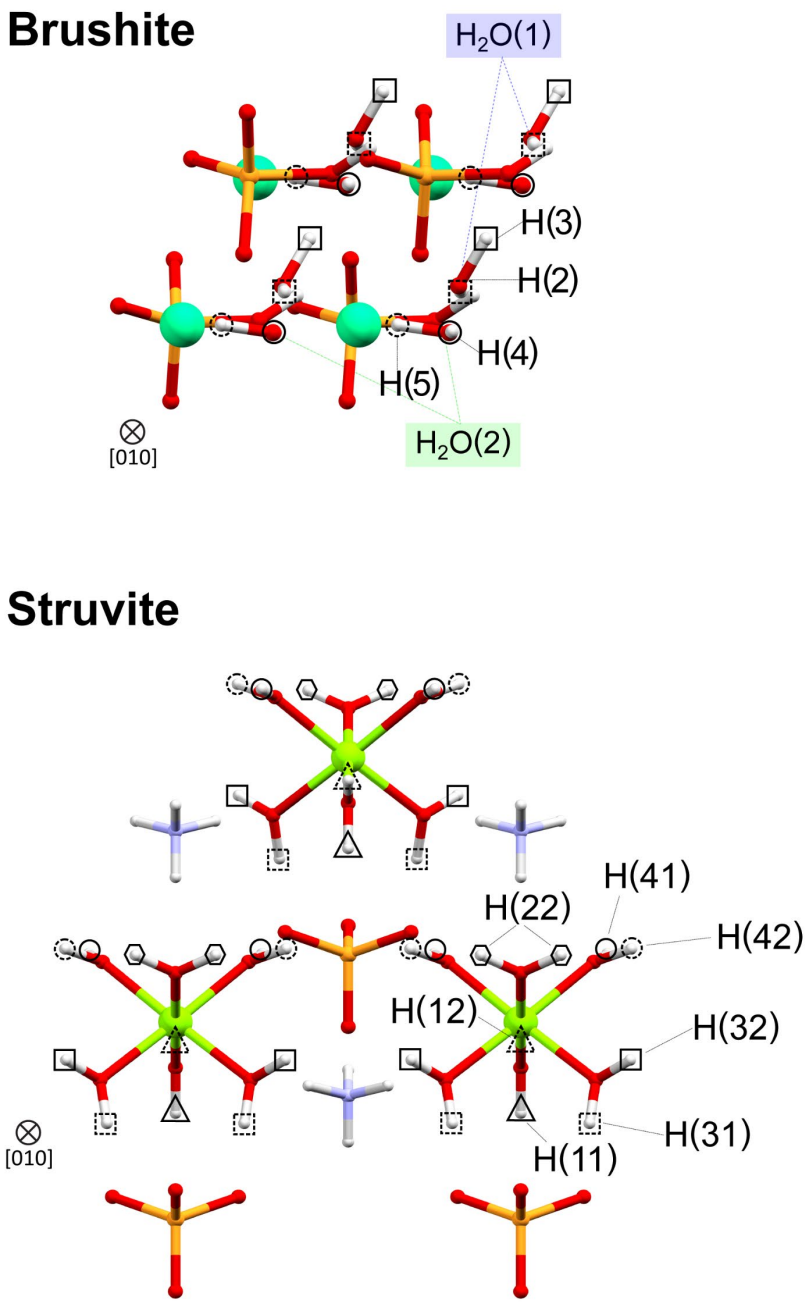

Figure 2.10: Crystal structures of brushite (top) and struvite (bottom) with water molecules labeled. Figure adapted from Robinson et al.[53]

The NIR spectrum of brushite has two main peaks at 5177 and 5117 cm^{-1} with a broad tail on the lower-frequency side of the peaks. The peak at 5120 cm^{-1} likely originates from $H_2O(1)$ (Figure 2.10) which has longer OH bonds in its neutron diffraction structure (0.97-0.98 Å) than $H_2O(2)$ (0.94-0.95 Å) which has a NIR peak at 5180 cm^{-1}.[81] Brushite has four water stretching modes in

the mid-IR with $H_2O(1)$ having peaks at 3270 and 3080 cm^{-1} and $H_2O(2)$ having peaks at 3522 and 3471 cm^{-1}. Bending modes for the two waters are indistinguishable at 1650 cm^{-1}. As the summed frequency of the stretching + bending modes for $H_2O(1)$ are below the observed NIR peaks, the primary brushite at 5180 and 5120 cm^{-1} are from $H_2O(2)$. Shoulders near 5000 and 4800 cm^{-1} are likely from the weaker stretching + bending modes of $H_2O(1)$ within the tail of the stronger $H_2O(2)$ combination modes.

2.3.1 Diffuse reflectance

DRIFTS was used to check whether absorption features from oriented single crystal measurements correlated with the anisotropic absorption spectrum for minerals of interest. Figure 2.10 Shows relative absorption from DRIFTS with mineral concentration within KBr powder calculated in terms of volume fraction $\left(\frac{-\ln(R)}{c_m \rho}\right)$ where R is the raw reflectance spectrum, c_m is mass fraction, and ρ is mineral density. Peak shapes in the region of interest correlate well between DRIFTS powder spectra and single-crystal spectra. Thus, it seems that the single-crystal absorption spectra capture the absorption features present in isotropic powders. Water molecules in COM, COD, and gypsum are known to flip 180° about the water C_2 axis at frequencies $>10^6$ s^{-1} which likely lessens the influence of anisotropy indicated by crystal structure.[82,83] Similar behavior is likely exhibited in struvite and brushite.

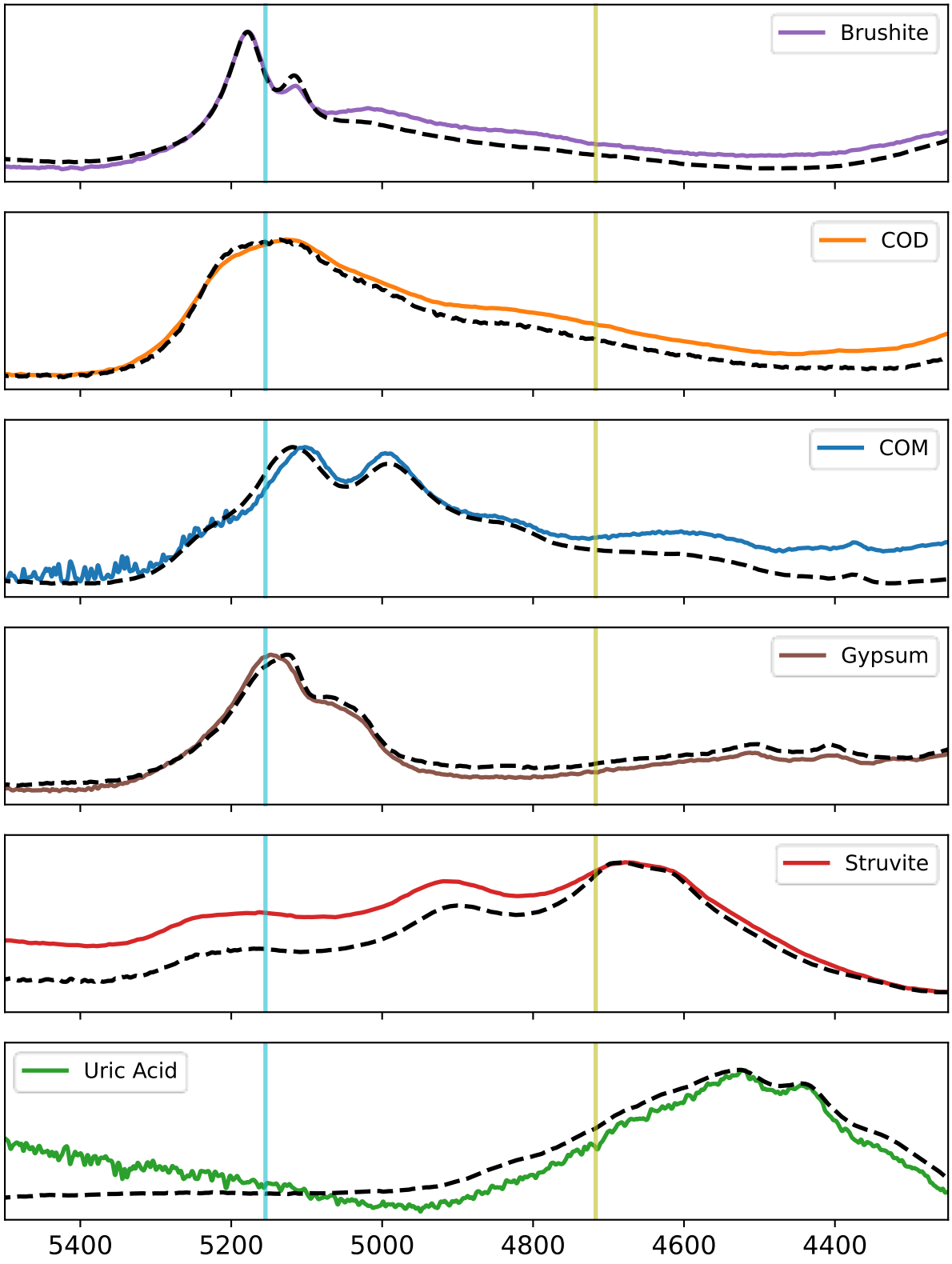

Figure 2.11: Absorbance comparison between single crystals (dashed line) and DRIFTS (solid lines).

2.3.2 Applying absorption coefficients to lithotripsy research

Access to quantitative absorption coefficients has significant potential value for those looking to model laser lithotripsy. Absorption by minerals within kidney stones is likely to vary from values presented here as in-vivo mineralization occurs in complex solutions allowing for substitution of ions in the crystal structure. Laser light is unpolarized when exiting laser fibers during lithotripsy, and small crystallites will scatter radiation in all directions making absorption isotropic for kidney stones in practice. Though diffuse reflectance data indicates good correlation in absorption in the regions of interest, differences in absorption due to crystal orientation may result in deviations when modeling ablation. Biomolecules present within kidney stones may alter the average absorption spectrum of stones, though the NIR absorption spectra of kidney stone powders and pure mineral powders are still similar suggesting most absorption is caused by the more abundant minerals.[60]

The main source of variability in absorption and ablation of kidney stones in pure minerals versus human stones is likely to result from urine present in pores or cracks within a stone. For thulium lasers, for example, the absorption coefficient of water is ≈50 times greater than the absorption coefficient for uric acid. A uric acid stone with only 5% of its volume occupied by pores or cracks would thus have more laser energy absorbed by water than anhydrous uric acid for thulium fiber lasers. Further structural analysis of stones will be necessary to understand any potential role of urine-filled pores or cracks on overall ablation.

Finally, other factors like pulse duration or peak pulse power likely play an important role in ablation efficacy of differing laser systems. The significant effects of laser pulse characteristics are discussed in Chapter 4.

2.4 Conclusions

Quantitative measurements of photothermal and thermochemical properties are essential to quantitative discussion of kidney stone ablation by laser lithotripsy. This work presented near-infrared absorption coefficients for kidney stone minerals that can be used alongside heat capacities and degradation temperatures to model mineral decomposition. NIR peaks were correlated with mineral crystal structures with most water-bearing minerals showing stronger absorption at 1.94 μm than 2.12 μm due to the combination of water bending and stretching modes. The relative strength of absorption coefficients provides a quantitative explanation for previously observed ablation thresholds in kidney stone minerals. Urological researchers may use these absorption coefficients to improve understanding of laser lithotripsy mechanisms with discussion of potential computation models presented in Chapter 5.

Chapter 3 Raman Mapping for Structural Analysis of Kidney Stones[^]

3.1 Introduction

Despite the prevalence of kidney stone disease, elucidating the specific mechanisms of kidney stone formation has proven difficult given the impracticality of studying their growth in vivo. In the absence of longitudinal in vivo measurements, an understanding of kidney stone growth has been developed through in vitro crystallization experiments and post-surgical analysis of kidney stone structure. Numerous analytical techniques have been applied to the observation of kidney stone structure including computed tomography, electron microscopy, polarized light microscopy, fluorescence microscopy, multiphoton excitation microscopy, infrared microscopy, and Raman microscopy.[1,8,10,12,13,84–91] Each method has advantages and disadvantages which are detailed below.

3.1.1 Techniques for structural analysis of kidney stones

X-ray computed tomography (CT), especially modern micro computed tomography (μCT), is the most general method for studying the distribution of bulk materials in kidney stones.[13,15,84–86,88,92,93] The most significant advantage of CT methods is their non-destructive nature: mineral distribution within kidney stone fragments of any size may be analyzed without sample preparation. Modern μCT can achieve voxel resolution reaching 2 μm^3 for smaller stone fragments revealing regions of COM in uric acid stones or apatite in struvite stones.[85] The major drawback of μCT is the reliance on contrast from relative attenuation for differing compounds of interest which can lead to mistaken mineral identification.[86] In some cases, lack of contrast prevents

specific chemical identification entirely as is the case for anhydrous uric acid and its various derivatives like uric acid dihydrate, sodium urate, or ammonium urate.[85] Identification of specific drug metabolites is also important in rare but potentially deadly cases which cannot be accomplished by X-ray contrast alone but is straightforward for vibrational spectroscopies due to the availability of spectral libraries for drugs and their metabolites.[8]

Scanning electron microscopy will always be of use for analyzing kidney stones due to its superior spatial resolution compared to tomography or optical methods.[1,90,91,94] This allows direct imaging of nanoscale features[95] like bacterial imprints left on the minerals forming urinary calculi.[96,97] Energy dispersive X-ray spectroscopy (EDX) allows observation of elemental ratios via SEM which can be used to identify minerals present.[90,94,98,99] Despite the obvious advantages, SEM typically uses high vacuum which may cause dehydration of certain minerals like struvite or brushite. Analyzing large stone fragments via SEM can also be time consuming as reaching high vacuum is difficult for large, porous samples containing adsorbed water. Environmental SEM can be used for wet samples at higher pressures though attempts at identifying calcium oxalates by carbon/oxygen ratio has proven difficult in literature examples.[13]

Infrared microscopy provides similar information to Raman spectroscopy but can only reach spatial resolutions of ≥5 μm due to the diffraction limit of infrared light. Synchrotron IR microscopy has proven useful in identifying abundance of organic material within stones,[100] but spatial resolution is still poor and access to synchrotrons is limited. Polarizing light microscopy can provide information about crystal orientation at 1 μm spatial resolution but requires thin sectioning which destroys the majority of stone samples.[12,15,84] Multiphoton microscopy shows strong potential for mapping kidney stones as crystal composition and orientation can be gleaned

from a single instrument.[87] However, the literature only contains one example of multiphoton microscopy applied to kidney stones and, thus far, lacks identification of brushite and struvite.[87]

3.1.2 Raman spectroscopy for kidney stone analysis

Use of Raman spectroscopy for phase identification in kidney stones has its origins in the work of Michel Daudon et al. in the 1980s.[101] At that time, infrared spectroscopy was used for bulk analysis of stone minerals much as it is today. The value of Raman spectroscopy was recognized by Daudon for its ability to identify phase of individual crystals on a scale of 1 μm which offers insight into kidney stone formation not available by bulk analysis.[101] Proliferation of commercial Raman instrumentation in the past 40 years has enabled many researchers to adopt Raman spectroscopy for analysis of biomineralization with more advanced computers allowing for chemical imaging in addition to spot measurements of individual crystals.[8,102–110]

Raman chemical imaging of kidney stones has received some recent attention in the literature for both primary analysis of stone structure and as secondary analysis to confirm fluorescence microscopy observations.[8,10,13] Like fluorescence microscopy, Raman microscopy can image on spatial scales near the diffraction limit of visible light intermediate between μCT (>2 μm) and SEM (<100 nm). Despite its potential, autofluorescence from biomolecules has been a barrier to wider adoption of Raman chemical mapping for the study of biomineralizations as it can preclude the use of more sensitive visible wavelength lasers for Raman excitation.[110–112] Switching to longer wavelength lasers significantly decreases the intensity of Raman scattering as $I_{Raman} \propto \lambda^{-4}$. The decrease in Raman scattering efficiency requires longer exposure times or higher power densities increasing the risk of sample degradation due to heating from laser exposure.

Photobleaching is often employed as an alternative to laser switching in samples with high fluorescence background.[111,113] Photobleaching inactivates fluorophores by exposing samples to

laser radiation prior to spectral collection. In some cases, exposure to laser radiation during continuous scanning can adequately reduce background fluorescence negating the need for separate bleaching periods.[111] Alternatively, chemical bleaching using 30% hydrogen peroxide can reduce autofluorescence but requires careful application to prevent tissue damage in biological samples.[114] Chemiphotobleaching has been recently proposed as an alternative to laser photobleaching and harsh chemical bleaching utilizing lower (3%) concentrations of hydrogen peroxide in concert with photodiode irradiation for gentle and permanent destruction of fluorophores in pigmented samples.[115] This chemiphotobleaching technique was adapted for use with kidney stones which ultimately allowed use of 532 nm radiation with all inorganic stones.

3.1.2.1 Raman mapping of kidney stones

In the remainder of this chapter, chemical maps of kidney stones are presented and their implications for stone formation discussed. Images at ≤1 μm are shown for the six most common forms of kidney stone revealing important features like the potential disruption of layered COM growth by a <3 μm scale crystal of COD and the existence of 2-3 μm thick COM rings with uric acid stones that could hinder dissolution and excretion.

3.2 Methods

Raman imaging was performed on kidney stone samples from a library of de-identified stones and fragments. Samples and the figures in which they appear are listed in Table 3.1 with major minerals of each sample listed.

3.2.1 Sample preparation

Kidney stone samples were prepared by embedding, grinding, and polishing to achieve optically flat surfaces. Small stone fragments with sizes <5 mm were placed in the center of

circular, 1 inch diameter acrylic holders with depressions tailor-milled for each sample. Fragment samples were then embedded in cyanoacrylate glue which was left to cure for 1 week before grinding and polishing. Water-wetted sandpaper was used for hand-grinding of embedded samples with a final grit size of J2500 (average particle size of 5.5 μm). All grinding and polishing used float glass as a backing material for sandpaper or polishing cloth to ensure flatness.

For larger kidney stone fragments, Crystalbond 509 (Ted Pella) or Crystalbond 555 (Ted Pella) were used for fixing samples in acrylic holders as these are both removable using acetone or water, respectively. Crystalbond 509 was used for samples primarily composed of COM, uric acid, or hydroxyapatite as these are not degraded at the 150 °C temperature used for melting the embedding medium. For struvite, brushite, and COD Crystalbond 555 was used as it has sufficient flow for embedding at 70 °C. Samples fixed by or embedded in Crystalbond 555 were ground using sandpaper wetted by mineral oil to prevent release of the sample due to dissolution of the mounting medium.

After grinding, samples were polished consecutively using 1 μm and 0.3 μm alumina suspensions on Alpha-A low-nap polishing cloth (Ted Pella). For samples embedded in Crystalbond 555, mineral oil and alumina suspension were mixed in roughly equal parts volume to prevent sample release due to dissolution of Crystalbond 555 by water. After polishing, mineral oil was removed by rinsing with hexanes or petroleum ether followed by two 24-hour cycles of soaking and rinsing in 20 mL hexanes or petroleum ether.

Chemiphotobleaching was performed after polishing by covering samples with 1 mL of 6% hydrogen peroxide solution and exposing them to light from a high-power rectangular array of white light emitting diodes (GS Vitec LT-V9-15) placed 5-6 cm above the sample for one hour.

Samples were re-polished using 0.3 μm alumina suspensions after chemiphotobleaching to re-expose fresh mineral faces.

3.2.2 Raman mapping

Raman microscopy was conducted using Renishaw InVia microscopes. Instrument settings for each of the figures presented in this chapter are listed in Table 3.1. Additional Raman images that are not discussed in this chapter can be found in Appendix A for future researchers interested in kidney stone structure. Scans were typically performed using high confocality mode for better fluorescence rejection. 532 nm diode lasers were predominantly used for calcium oxalates, calcium phosphates, and struvite stones while a 785 nm diode laser was predominantly used with uric acid stones. A 633 nm diode laser was tested but was found to be inferior in all cases. Several maps were performed with a 30 mW violet laser (405 nm) which can analyze both uric acid stones and inorganic mineral stones but causes damage in most samples.

Raman images were collected using Renishaw's StreamHR® mode for Raman mapping. Typical settings for COM, COD, and HAp samples were 0.1 s exposure time with spatial resolution of 0.5 μm for a scan speed of 5 μm/s. The 532 nm laser power was typically set to ≈100 mW output for these three minerals. With losses in the optics of the instrument, the power at the sample is ≈50 mW with a spot size of 0.5 μm for a 50× objective for a power density of 20 W/μm^2. For struvite and brushite power output of the 532 nm laser was lowered to ≈50 mW, exposure times were reduced to 0.05 μs, and spatial step size was increased to 1 μm for a scan speed of 20 μm/s. At these settings, irradiance at the sample surface is estimated to be 2.5 W/μm^2. These settings have prevented damage on polished and peroxide-treated samples of struvite and brushite.

Uric acid stones were imaged using a 785 nm laser as uric acid itself fluoresces when using visible wavelength lasers. Exposure times were increased to 1 s to compensate for the lower sensitivity at 785 nm.

Table 3.1: Raman mapping settings for listed figures.

	Major minerals	Laser λ	Spatial resolution	Objective	Exposure time (s)	Confocality
Figure 3.2a,c	COM	532 nm	5 µm	50×	0.1	High
Figure 3.2b,d,f	COM	532 nm	1 µm	50×	0.5	High
Figure 3.4a,b	Uric acid	785 nm	10 µm	20×	1	Standard
Figure 3.4d,e	Uric acid	785 nm	1 µm	50×	1	Standard
Figure 3.5a	Brushite	532 nm	10 µm	50×	0.05	High
Figure 3.5b	Brushite	532 nm	1 µm	50×	0.025	High
Figure 3.5c	Brushite	532 nm	1 µm	50×	0.05	Standard
Figure 3.7a	Struvite	532 nm	10 µm	50×	0.05	Standard
Figure 3.7b	Struvite	532 nm	1 µm	50×	0.05	Standard
Figure 3.9	COD, COM, HAp	532 nm	0.5 µm	50×	0.1	High

3.3 Results and Discussion

3.3.1 Raman spectra of powdered minerals

Raman spectra of powdered minerals from 150-4000 cm^{-1} are shown in Figure 3.1 with fluorescence background removed using Renishaw's WiRE software. In Figure 3.12-Figure 3.21 Raman spectra from 150-1900 cm^{-1}, the typical scan region for the 532 nm laser, are shown for individual minerals as well as potential interferants like embedding media. Peaks useful in

identifying the six most common minerals of kidney stones are listed in Table 3.2; the origins of each peak are referenced if available.

Table 3.2: Raman peaks for mineral identification in kidney stone mapping.

Mineral	Peak position	Relative peak intensity	Notes
COM	1491	0.55	Carboxylate CCO symmetric stretch[77]
	1464	1	Carboxylate CCO symmetric stretch[77]
	897	0.35	Carboxylate CCO bending mode [77]
COD	1478	1	Carboxylate CCO symmetric stretch[77]
	913	0.22	Carboxylate CCO bending mode[77]
Uric acid	626	1	
	999	0.56	
	1039	1	
	1407	0.65	
Hydroxyapatite	962	1	Phosphate P-O symmetric stretch[116]
	611	0.026	Phosphate ν_4 antisymmetric bend[116]
	589	0.099	Overlaps with peak at 611 cm^{-1} Double/shouldered peak near 600 cm^{-1} distinguishes carbonate apatite from struvite
Brushite	985	1	Phosphate ν_1 symmetric stretch[117]
	993	0.45	Appears as shoulder to more intense phosphate stretch at 985 cm^{-1}.
	878	0.26	Phosphate ν_3 antisymmetric stretch [117]
Struvite	945	1	Phosphate ν_1 symmetric stretching mode?[118]
	565	0.46	Phosphate ν_4 antisymmetric bending mode[79]
	1691	0.13	Ammonium stretching band(s),[118]

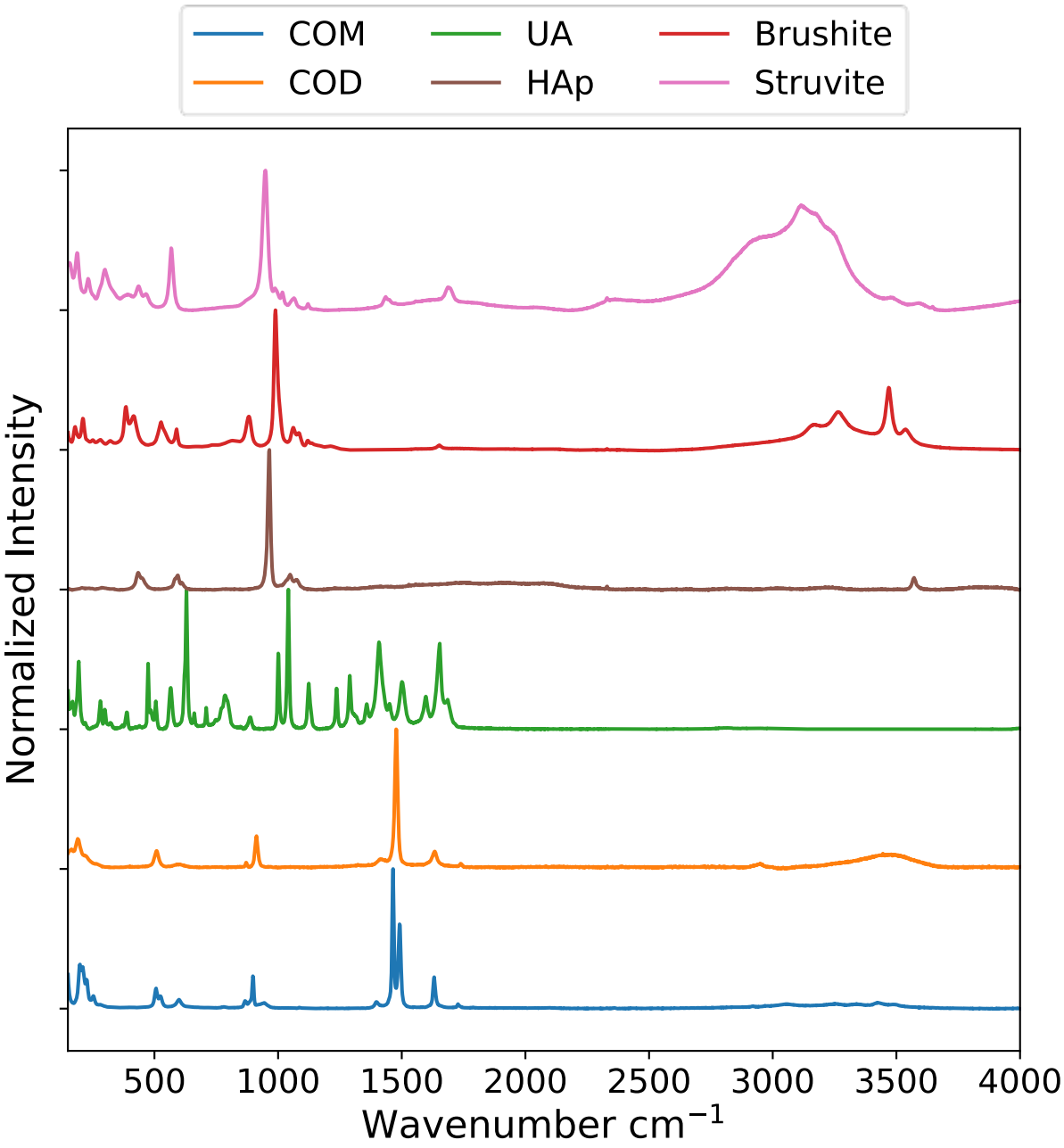

Figure 3.1: Normalized Raman spectra for powdered mineral samples from 150-4000 cm^{-1}.

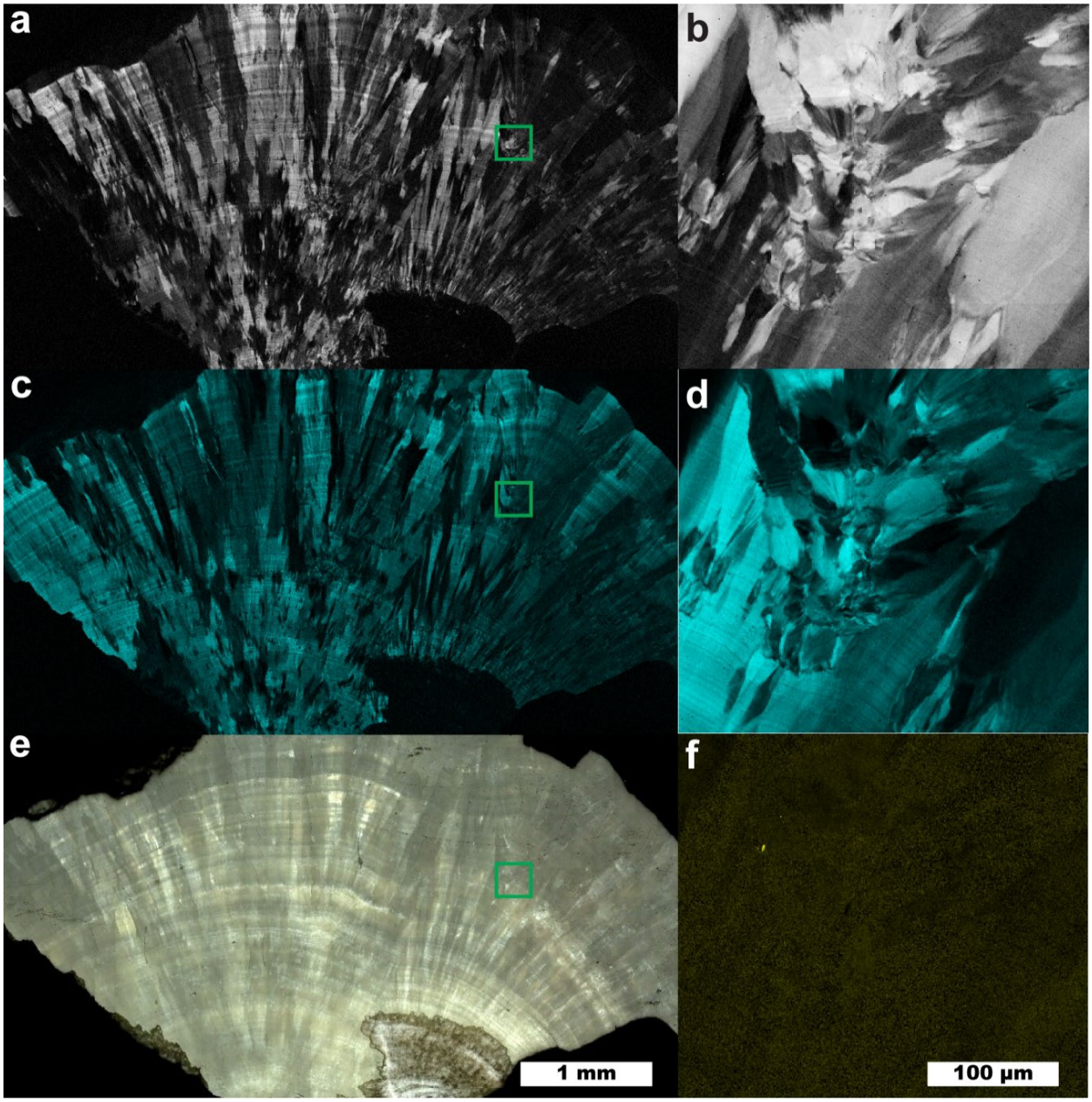

Figure 3.2: Raman map of a COM kidney stone with region of interest marked by green square. (a) 10 µm spatial resolution map of COM sample (1464 cm^{-1} peak dominant). (b) Region of interest at 1 µm spatial resolution (1464 cm^{-1} peak dominant). (c) 10 µm spatial resolution map of COM sample (1490 cm^{-1} peak). (d) Region of interest at 1 µm spatial resolution (1490 cm^{-1} peak). (e) White light image of COM stone sample. (f) Map of COD at 1 µm spatial resolution in region of interest.

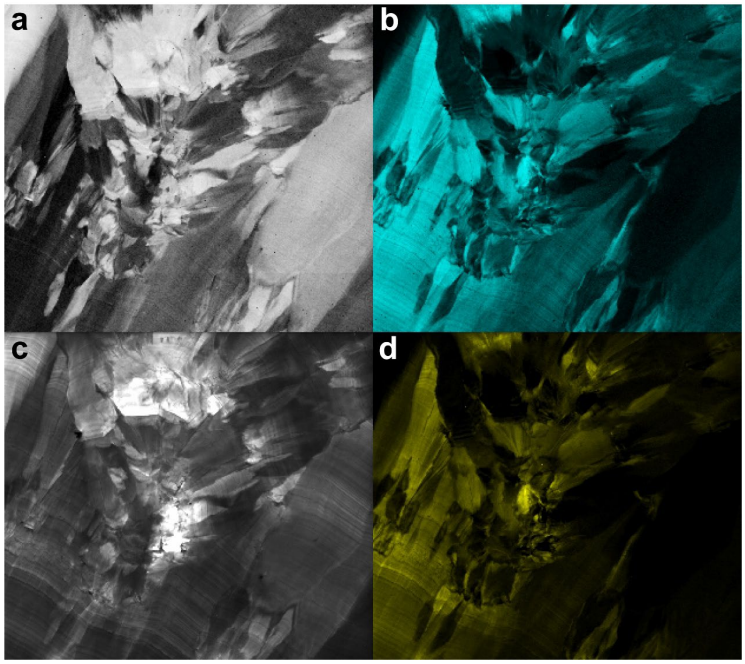

Figure 3.3: Example of improper identification of COD by least-squares methods. (a) COM identified by 1464 cm^{-1} peak as in Figure 3.2. (b) COM identified by 1490 cm^{-1} peak as in Figure 3.2. (c) COM identified by spectrum of COM powder. (d) COD identified by spectrum of COD powder.

3.3.2 COM stone (type 1a)

Figure 3.2 shows Raman maps for a type 1a COM stone with layered spherulitic growth. The maps of COM are separated by their most prominent peaks centered at 1464 or 1490 cm^{-1}; these two peaks originate from stretching modes of oxalates in the (100) and (010) planes, respectively. The relative intensities of the 1464 and 1491 cm^{-1} peaks shift strongly with crystal orientation. Qualitatively, the presence of only one of these two peaks can make the Raman spectrum of COM appear qualitatively similar to that of COD which only has a single oxalate stretching peak at 1475 cm^{-1}. The overlap among the three oxalate peaks can lead to erroneous results when using least-squares methods and Raman spectra of powdered minerals for mapping as shown in Figure 3.3 in which regions with the 1490 cm^{-1} COM peak dominant were misidentified as COD when using isotropic spectra from powdered minerals. Using two COM spectra, one with the 1464 cm^{-1} peak

dominant and one with the 1491 cm^{-1} peak dominant, mitigates this issue leading to the accurate composition maps in Figure 3.2.

The type 1a stone fragment in Figure 3.2 exhibits radially symmetric, layered growth with several regions where radius of curvature abruptly changes indicating a change in growth process. The region mapped at 1 μm spatial resolution in subfigures b, d, and f is located at the epicenter of one such disrupted area. COM in this region appears to be randomly oriented indicating agglomeration of larger COM or COD crystals that did not undergo oriented attachment. The presence of a minute, <3 μm COD crystal was observed in the high-resolution maps near the boundary of the organized, layered region and the randomly oriented region of COM. This indicates nucleation of COD in free-floating solution prior to agglomeration. COM in this region may have nucleated in free-floating solution or converted from COD after agglomeration. The original phase cannot be deduced from crystal morphologies in this case.

3.3.3 Uric acid stone

Raman maps of a primarily uric acid stone are shown in Figure 3.4. The center of the uric acid stone is formed primarily of larger uric acid crystals while the outer regions are primarily formed of concentric rings. Larger crystals likely indicate rapid precipitation and growth due to elevated levels of uric acid in the kidney. Cracking among larger crystals near the stone center could be indicative of initial uric acid dihydrate formation which dehydrates to the more stable anhydrous uric acid via dissolution-reprecipitation or dehydration.[31,119] The ratio of calculated densities between uric acid dihydrate (1.65 g/cm^3) and uric acid anhydrous (1.85 g/cm^3) is 0.89. This would result in a void volume of 11% of the total volume previously occupied by uric acid dihydrate which is well above the ≈2% volume fraction needed for liquid water to be the dominant absorber in anhydrous uric acid stones when using a Tm fiber laser.

Prolonged hyperuricosuria with low uric acid supersaturation overall is likely the cause of the slower growing concentric rings observed in the outer region of the uric acid stone. Among the concentric rings of uric acid are several 2-20 μm thick layers of COM. Unlike the small COD crystal associated with the disruption in ring concentricity in the COM stone shown in Figure 3.2, the rings of COM do not appear to disrupt continuing concentric growth. This suggests that COM and uric acid can nucleate and grow on one another, and known epitaxial relationships between the two compounds further supports this hypothesis.[120]

Uric acid has a notable increase in solubility with increasing basicity starting around pH 5.[28] Though sodium or ammonium urate stones may form in more basic urine, the urate ion is about an order of magnitude more soluble at pH >6.5 than uric acid is at pH 4.5-5.5 making cation-urate stones much rarer than uric acid stones.[25,28,29] In contrast, COM has a relatively constant solubility at typical urine pH.[66,121] This suggests the concentric growth of COM on the surface of uric acid stones may prevent dissolution even when low urine pH is transient as uric acid can deposit at low pH, be coated by COM, and remain unexposed to solution even as pH increases. The Raman images we have collected show COM crystals with sizes of 2-3 μm arranged in ring-like growths, smaller features that may be missed by μCT demonstrating the value of Raman imaging for analysis of kidney stone structure.

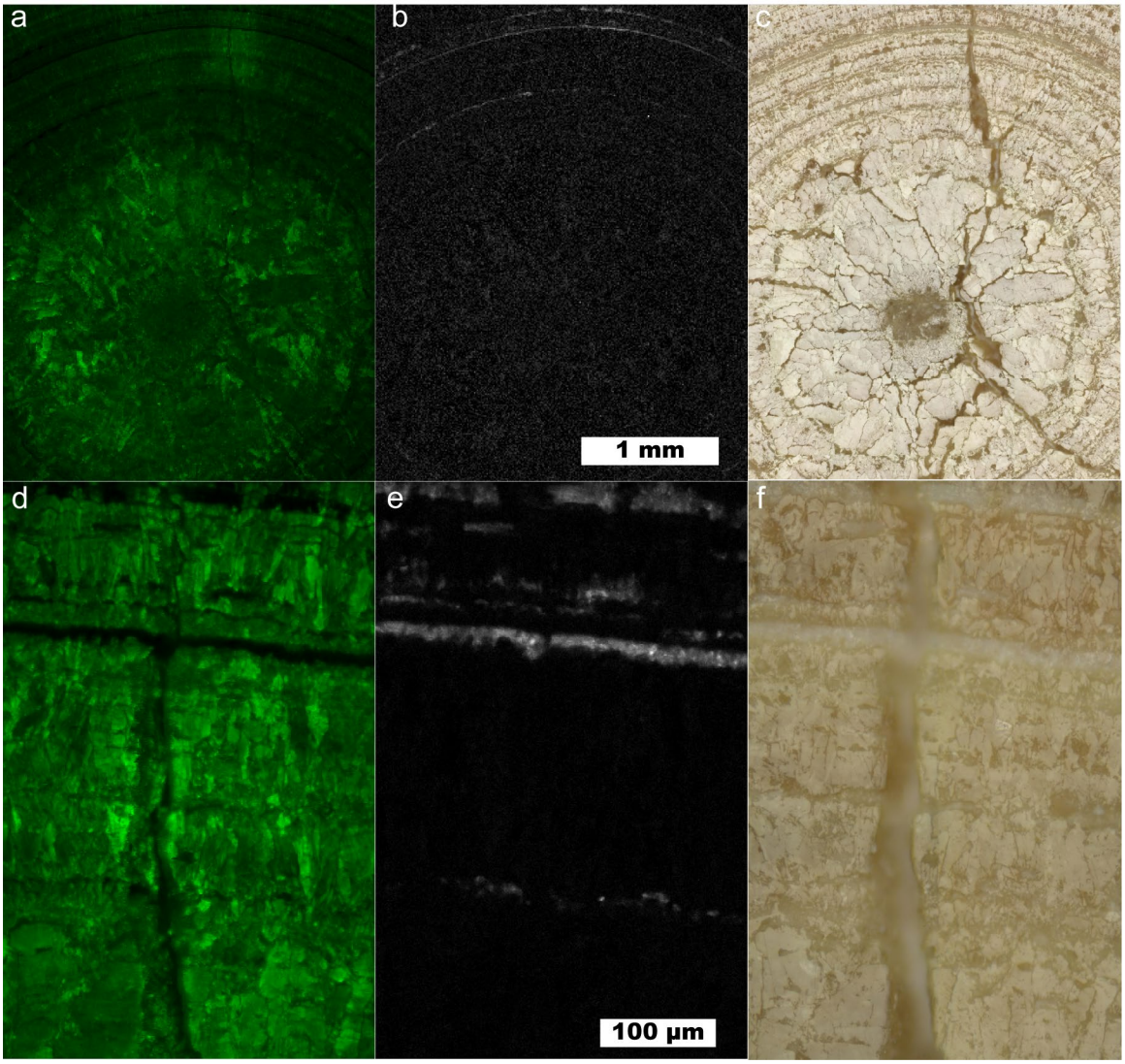

Figure 3.4: Map of a predominantly uric acid stone containing COM lasers using 785 nm laser. (a) Survey map of uric acid at 10 µm spatial resolution. (b) Survey map of COM (1464 cm^{-1} peak). (c) White light image for (a) and (b). (d) 1 µm map uric acid in region of interest. (e) µm map of COM in region of interest. (f) White light image for (d) and (e).

3.3.4 Brushite stone

Brushite stones typically take two morphologies: compact layered growth similar to type 1a COM stones and elongated, radially bundled, interlocking brushite crystals with increased void space.[85,122] Both are classified as type 4d in literature.[11] The stone in Figure 3.5 shows examples of both morphologies with a layer of "classic" radial crystals located between two layers of more compact brushite. Raman microscopy revealed the presence of calcium oxalates within the brushite

stone with more oxalate crystals found within the region of radially bundled brushite. As COM, COD, or brushite formation can be induced by hypercalciuria it seems likely that the radial bundles of brushite are related to high supersaturation with respect to all three minerals. Many of these COM and brushite crystals are only visible using high resolution (0.5 μm) spatial imaging, below the established spatial resolutions for μCT.

Brushite stones have a relatively high rate of recurrence, the highest among stones without genetic origin.[123] Unfortunately, there is no data available about recurrence comparing the two morphologies of brushite stone. Recurrence seems to be more common for faster-growing stones[123] which suggests that the bundled radial growth morphology of brushite would be more likely to recur. Subdividing the type 4d classification of brushite stones may be worthwhile in clinical stone analysis to facilitate comparisons between brushite morphology and recurrence.

Two concentric rings, one of COD and one of apatite, are visible in the survey map of brushite in Figure 3.4a. The deposition of the COD layer appears to coincide with the beginning of elongated, radially bundled brushite. This suggests crystallization of radially bundled brushite and COD crystals began simultaneously from a rapid rise in calcium concentration in urine. In typical urine, calcium concentrations are an order of magnitude higher than oxalate concentrations making oxalate the limiting factor in the growth of COD.[124] In contrast, phosphate concentrations are typically an order of magnitude greater than calcium concentrations allowing sustained growth brushite crystals which can lead to the observed radial bundles of elongated crystals.[124]

As apatite is less soluble than brushite at typical urine pH,[20] the ring of apatite observed in the outer compact region of this brushite stone may have formed through dissolution of brushite at the surface followed by reprecipitation as apatite. Other conditions that may have favored apatite deposition include temporarily higher pH that would disfavor brushite growth. The formation and

prevention of apatite layers in brushite stones may deserve additional attention as the lower solubility of apatite at pH >4.5 could have an outsize impact on stone preservation much like the case of COM rings in uric acid stones.[16]

3.3.5 Struvite stone

Figure 3.6 shows a stone predominantly formed of struvite with a layered structure suggesting even growth. Struvite is always associated with urinary tract infections (UTI) with urease-producing bacteria causing elevated ammonia concentrations and higher pH allowing the formation of struvite. Bacteria are known to colonize on the surface of struvite stones[32,125] creating a localized environment where NH_4^+ concentration is high allowing continuous growth of struvite though other calcium phosphates and magnesium phosphates are more stable.[126,127]

Carbonate apatite is also commonly associated with struvite stones and is difficult to discern from struvite at the Raman mapping settings that were used to prevent struvite degradation. Powdered struvite and hydroxyapatite have their most prominent peaks, a phosphate symmetric stretch, located at 945 and 962 cm^{-1} with full width at half maxima of 21 and 11 cm^{-1}, respectively (Fig. 3.1). Increased carbonate fraction in apatite causes peak broadening and shifts the phosphate symmetric stretch to lower wavenumbers further complicating phase identification.[128] Carbonate apatite is primarily observed near or within voids of the struvite stones. This suggests carbonate apatite either formed through dissolution-reprecipitation or formed in solution and agglomerated disrupting continuous struvite growth.[32,33,111]

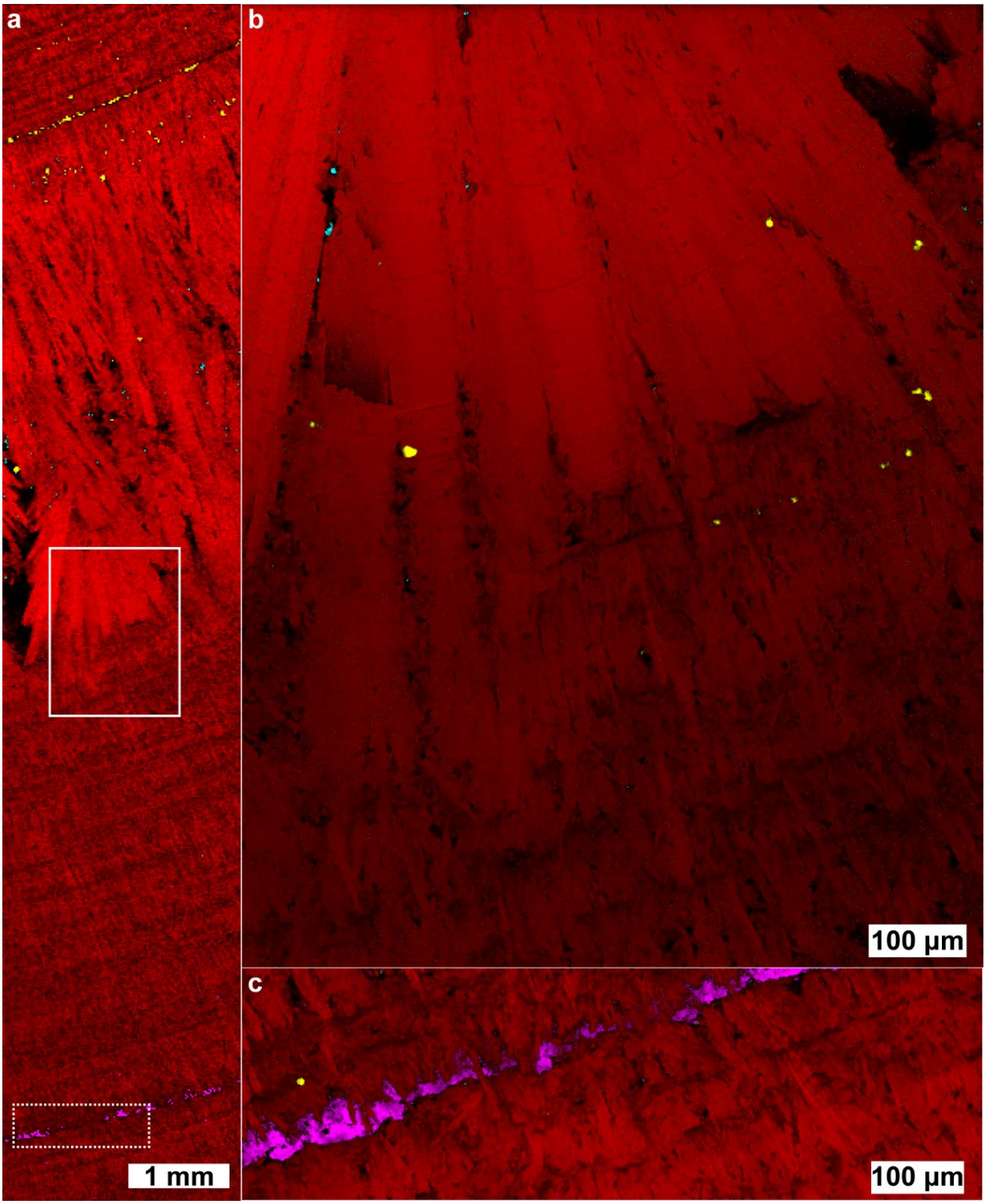

Figure 3.5: (a) Survey map of brushite stone. (b) 0.5 µm spatial resolution map at the transition zone from radial-to-compact brushite crystal organization. (c) Concentric ring of apatite growth.

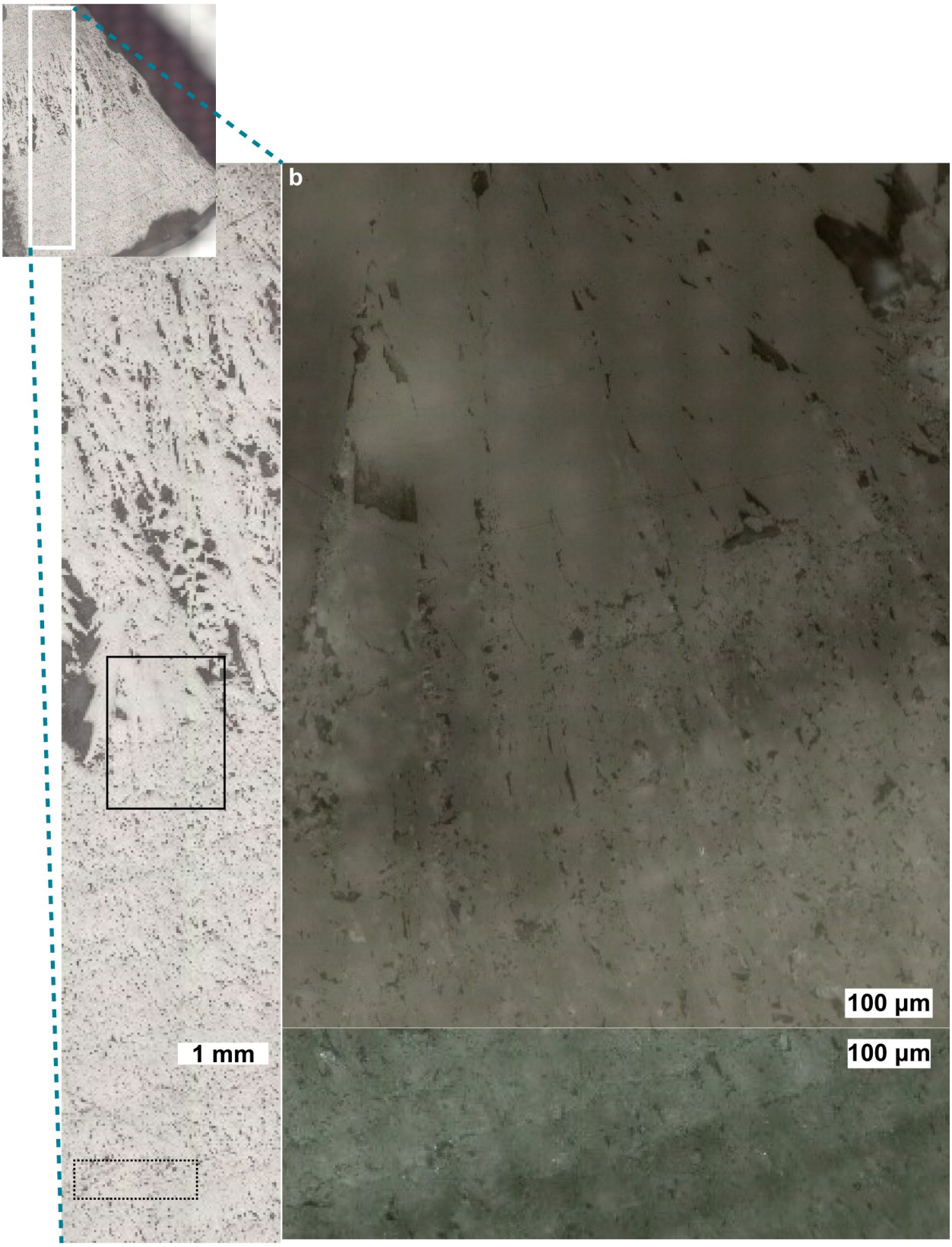

Figure 3.6: White light images of the brushite kidney stone fragment mapped in Figure 3.5.

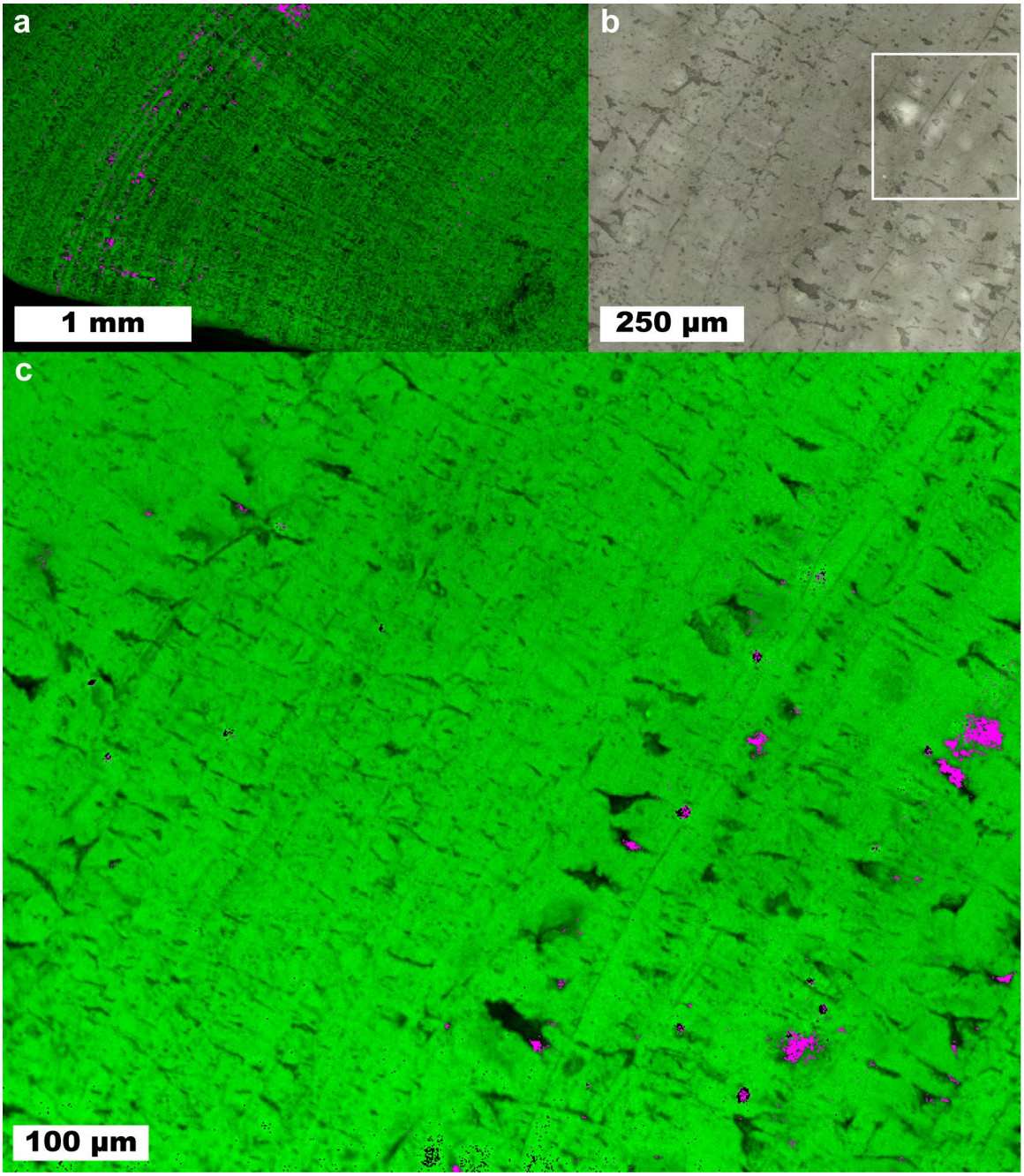

Figure 3.7: Map of a majority-struvite (green) kidney stone containing small amounts of apatite (magenta). (a) 10 µm spatial resolution map. (b) White light image of inset in (a). (c) 1 µm spatial resolution map of inset in (a).

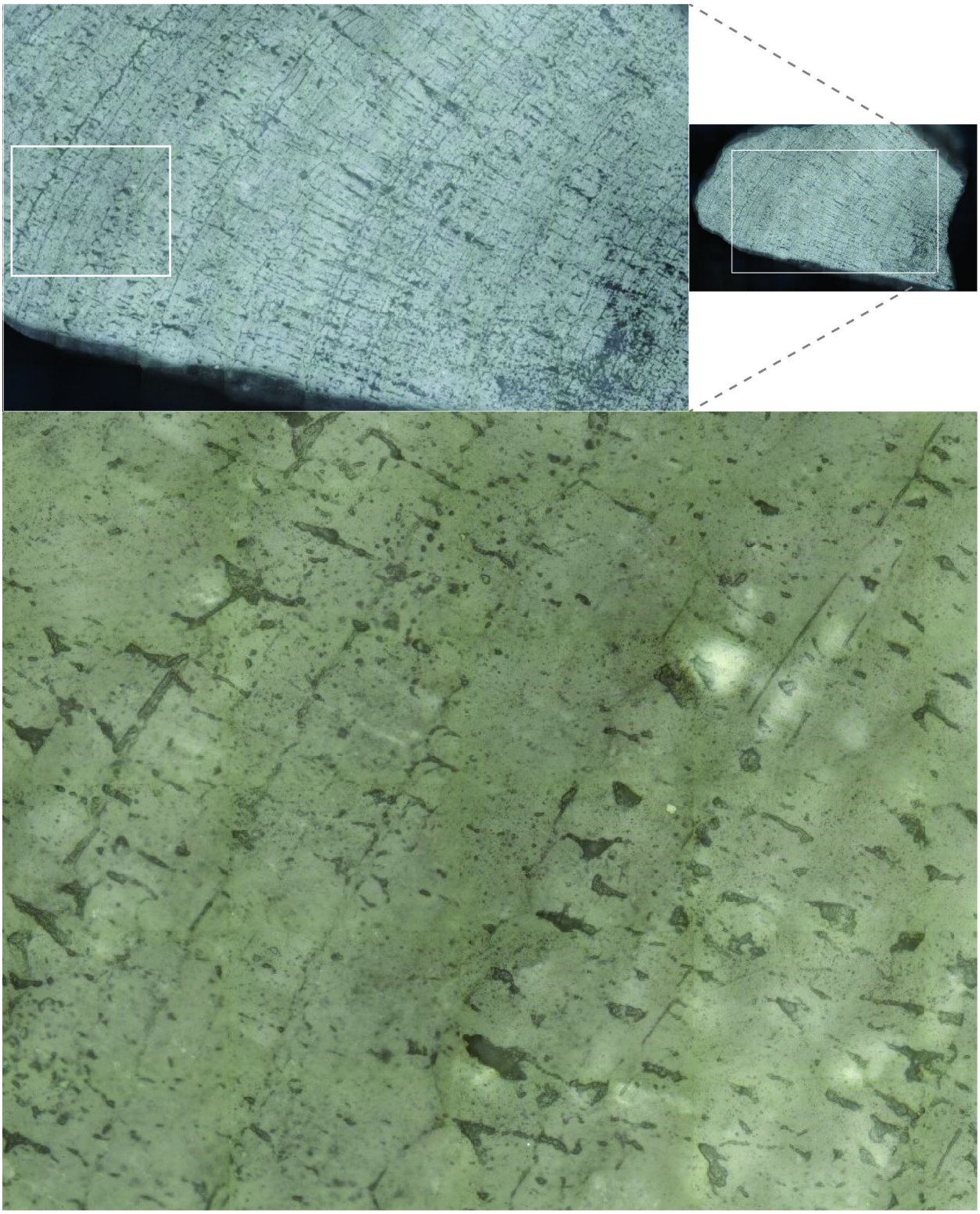

Figure 3.8: White light images of the struvite stone fragment mapped in Figure 3.7.

3.3.6 Mixed calcium oxalate and calcium phosphate stones

Calcium oxalates commonly occur together in stones either due to simultaneous precipitation or by incomplete conversion of COD to COM over time. Co-precipitation of both COM and COD is expected to produce crystals of differing morphologies which can be observed via microscopy or computed tomography.[10,13,84] Figure 3.9 shows a stone fragment containing a mixture of COM, COD, and apatite. Calcium carbonate was also observed, though this was determined to be the product of calcium oxalate degradation by the Raman laser during previous survey maps. Presence of calcium carbonate in stones should be interpreted with care as it is produced by thermal degradation during holmium laser lithotripsy[38,39,56] and rarely if ever contributes to actual stone growth.[106,129]

Sharp, straight features among COD crystals in Figure 3.9 suggests COD was either recently deposited or rapidly coated with biomolecules or other crystals preventing dissolution and reprecipitation to COM. Presence of large (>100 μm) COM crystals with hexagonal plate morphology indicate co-precipitation of both calcium oxalate phases as both of these morphologies are associated with COM.[52] Layering appears within the COM crystal marked by region C of Figure 3.9 with darker regions having higher autofluorescence background potentially indicating higher biomolecule concentrations (Figure 3.10). Layering around the entire crystal indicates symmetric growth despite changing conditions in urine suggesting this COM crystal grew free-floating in urine prior to agglomeration.

The alternating layers of COM and COD marked by region B of Figure 3.9 show hexagonal plates of COM surrounded entirely by COD. COM has been found embedded in COD by others, but this pattern was noted for its resemblance to the COM plates growing on COD crystals in experiments attempting to grow artificial COM stones.

Figure 3.11 appears to show the graduate replacement of COD by COM over time with irregular patches of COD surrounded by radially organized COM. Void space, filled by cyanoacrylate, is found between the two calcium oxalate phases. As COD converts to COM via dissolution-reprecipitation rather than direct conversion,[130,131] this void space likely formed by dissolution of the less-dense COD (1.94 g/cm^3) as it converted to COM (2.21 g/cm^3).

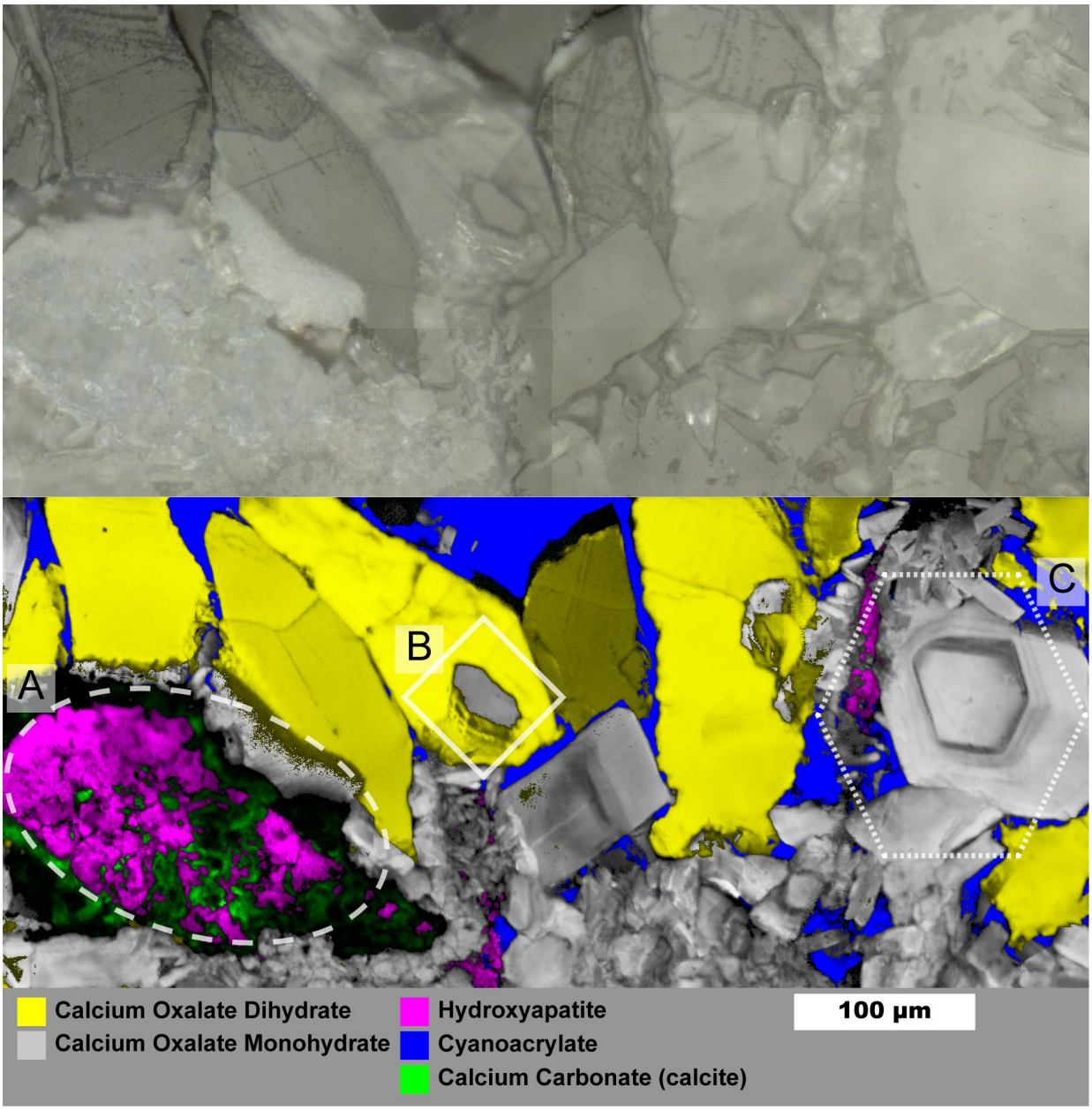

Figure 3.9: Top: White light image of stone fragment. Bottom: 1 µm spatial resolution map of mixed oxalate and apatite stone fragment.

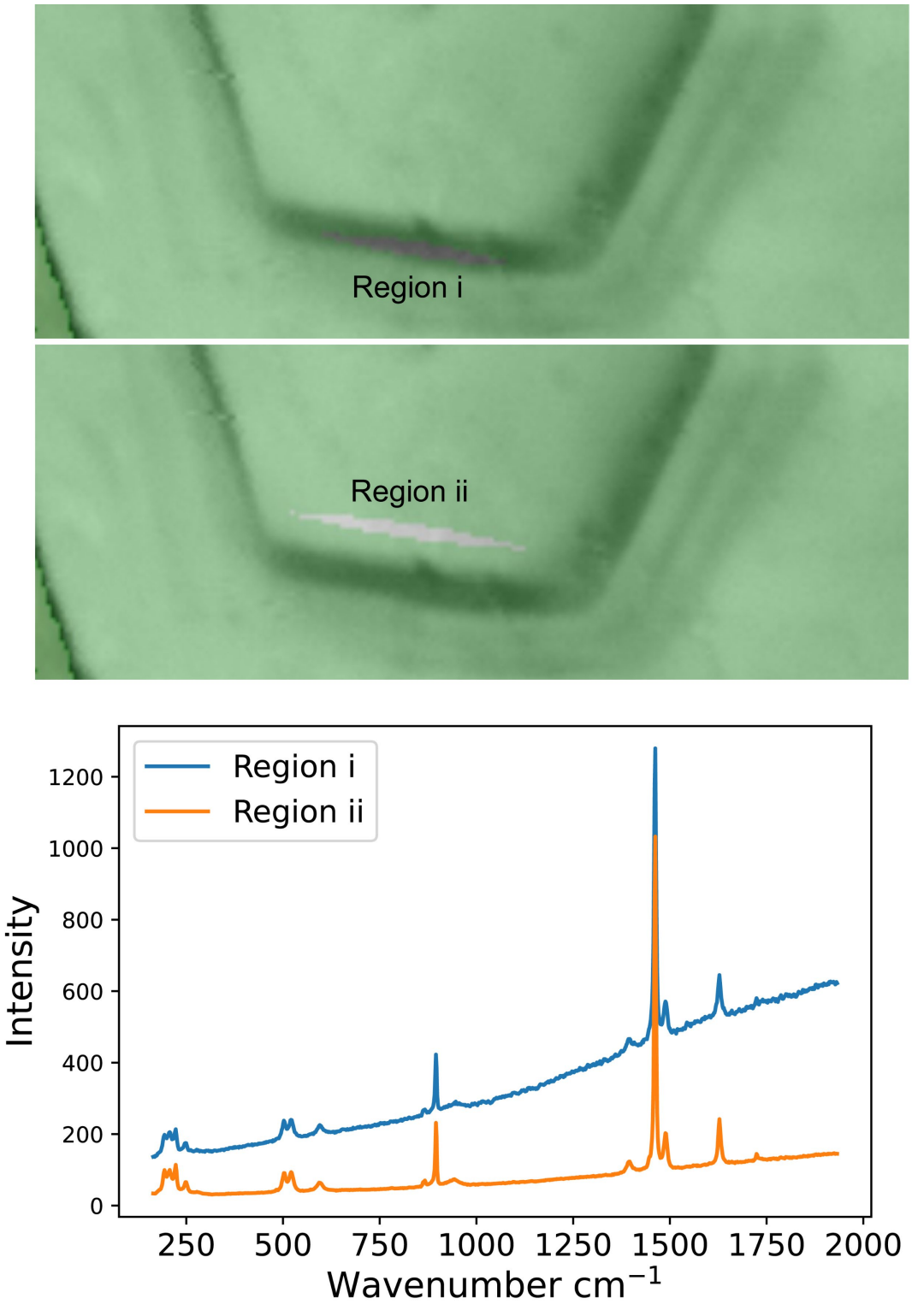

Figure 3.10: Plot showing higher autofluorescence in darker region (i) than in lighter region (ii) of the crystal marked in region (c) Figure 3.9.

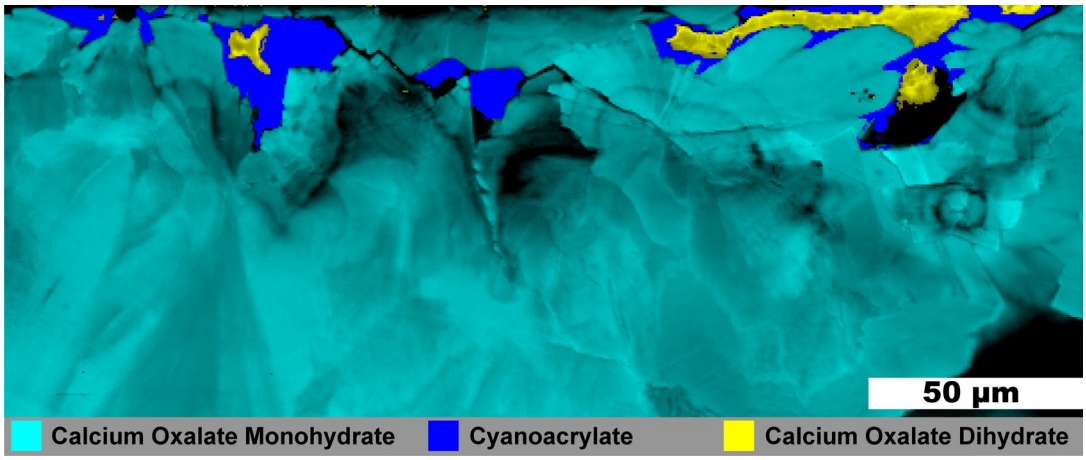

Figure 3.11: Map of stone fragment containing COD and COM at 0.5 µm spatial resolution.

3.4 Conclusions

Raman spectroscopy can chemically map kidney stones and other biomineralizations with <1 µm spatial resolution. Use of hydrogen peroxide combined with LED irradiation successfully decreased autofluorescence in human stones which enabled the use of more sensitive visible-wavelength lasers for Raman mapping. The six most common minerals in kidney stones: COM, COD, apatite, uric acid, brushite, and struvite, could be distinguished from each other using peaks in the 150-1900 cm^{-1} range. Mapping of a type 1a COM stone revealed evidence that free-floating COD and/or COM agglomerates on type 1a stones that primarily undergo concentric layered growth. In a similarly layered uric acid stone, COM occurred in concentric layers, a potential example of uric acid and COM epitaxial relationships allowing for symmetric growth of the uric acid stone despite presence of another mineral. Mapping of a brushite stone revealed compositional differences between regions of compact, layered brushite and regions with long, radially bundled brushite crystals. COM and COD in the region with longer, void-prone brushite crystals may indicate high calcium activity in urine allowing rapid brushite growth. Thus, the presence of COM or COD within brushite stones may be an indicator of higher recurrence risk in brushite stone forming patients as rapidly growing stones are known to recur more often.

The simultaneous chemical and structural information provided by Raman imaging provides a more complete understanding of kidney stone growth than other techniques. Raman imaging of features such as pore size and density prior to ablation may allow insights into the mechanisms of laser lithotripsy, particularly the role of urine vaporization within pores in ablation. Further use of Raman microscopy to study the structure of urinary calculi may offer new insights into their initial formation and growth benefitting urologists and scientists aiming to better understand biomineralization and its treatment.

3.5 Appendix: Additional Raman spectra

Below are Raman spectra from 150-1900 cm^{-1}, the typical range used for during Raman mapping, for each of the six minerals of most interest. Raman spectra for calcite, cured cyanoacrylate, acrylic, CrystalBond 509, and CrystalBond 555 are included as these compounds could be present due to contamination during sample preparation or from laser-induced degradation of the sample.

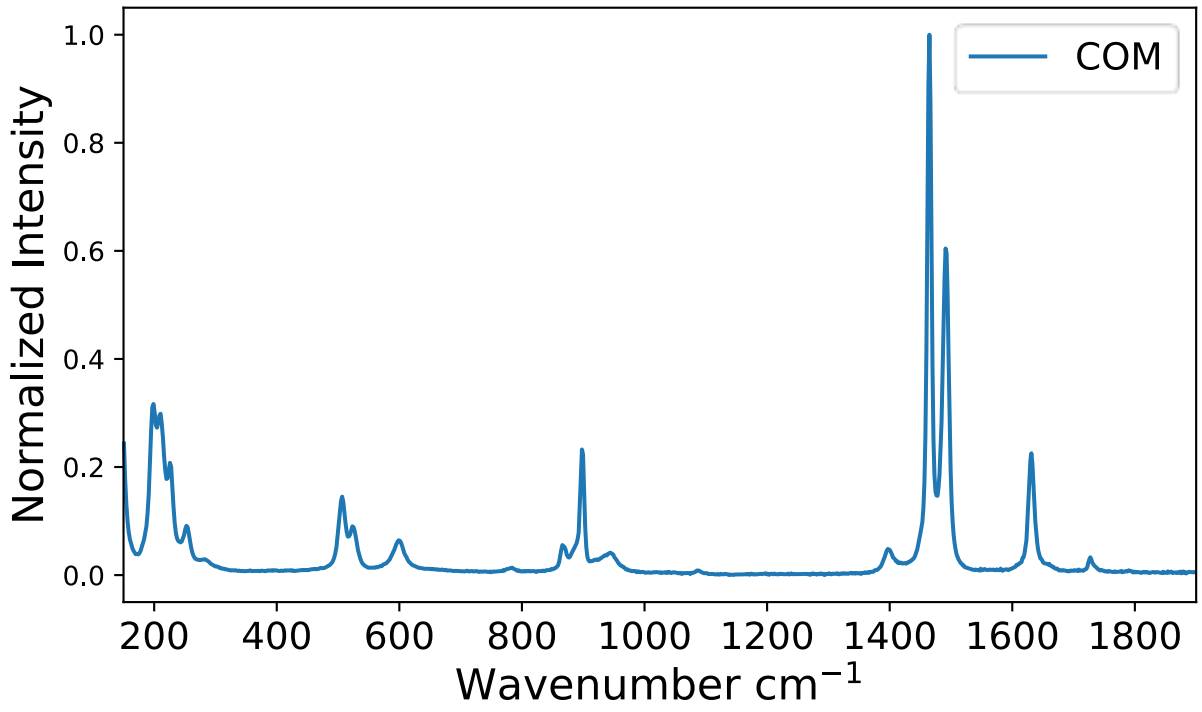

Figure 3.12: Raman spectrum of powdered COM in wavenumber region used for mapping.

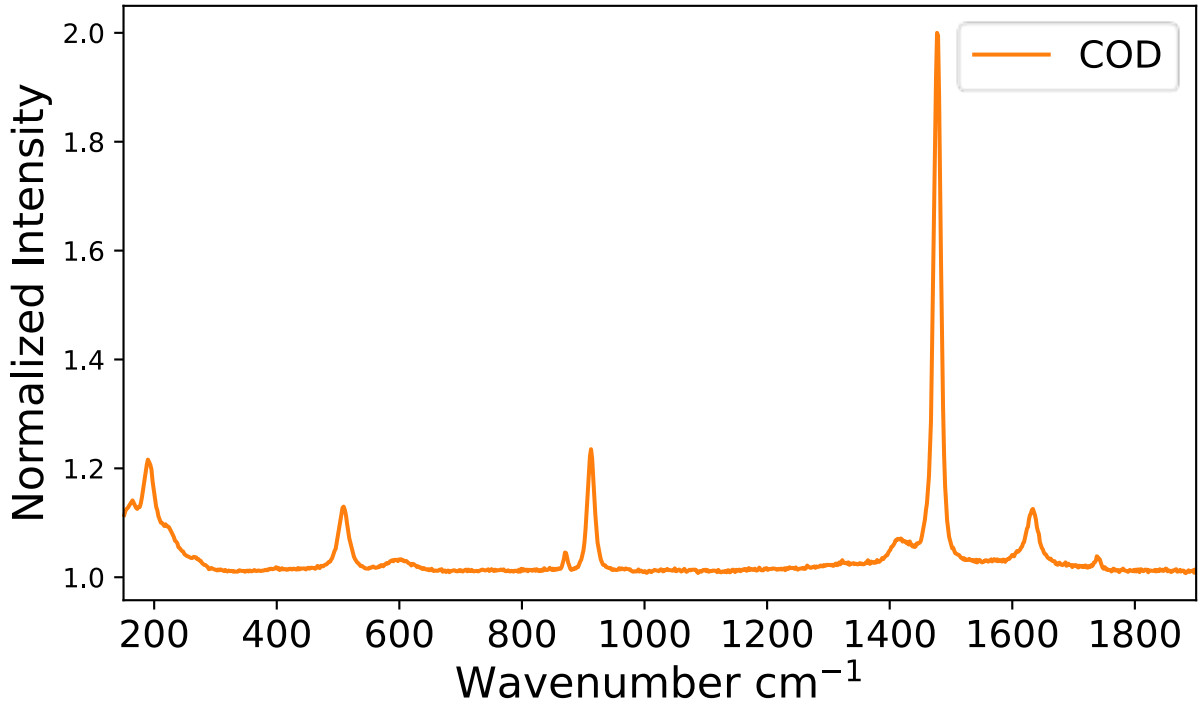

Figure 3.13: Raman spectrum of powdered COD in wavenumber region used for mapping.

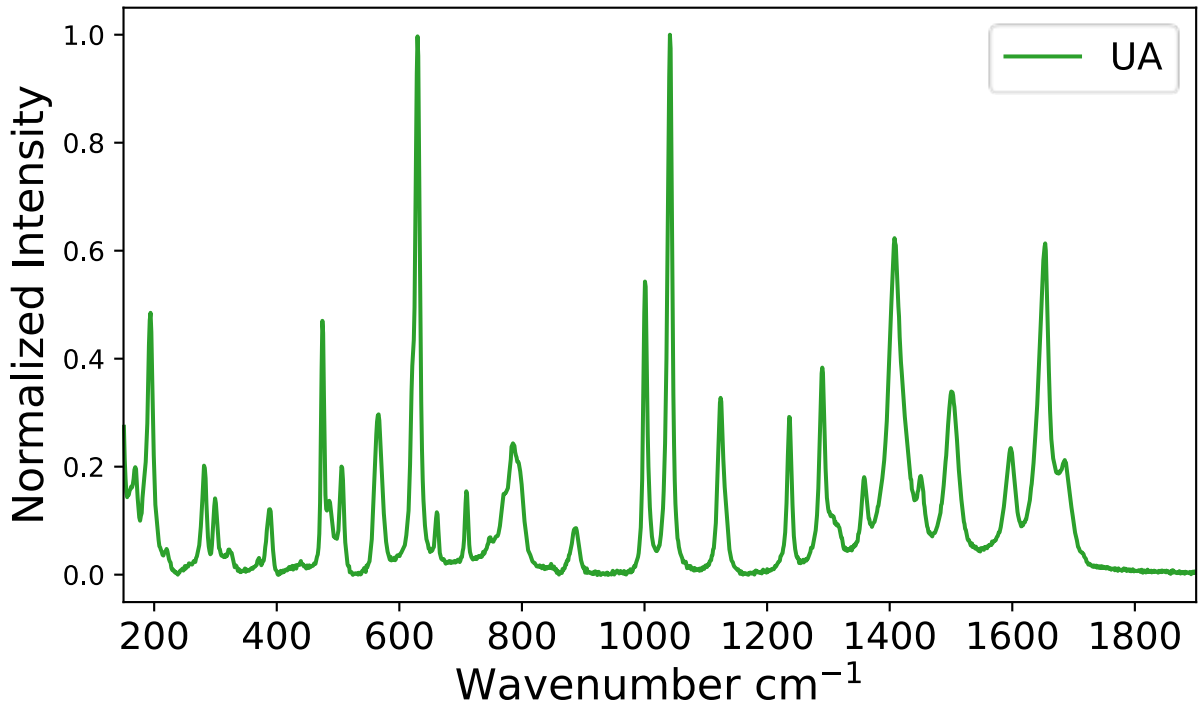

Figure 3.14: Raman spectrum of powdered uric acid in wavenumber region used for mapping.

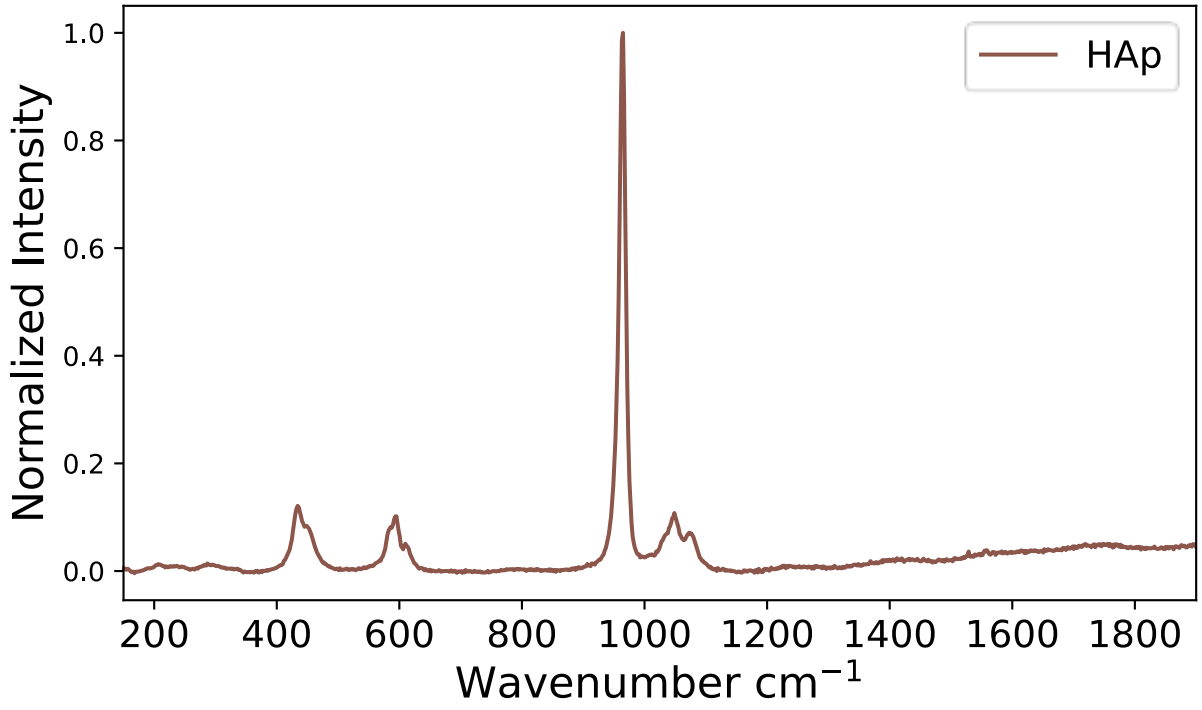

Figure 3.15: Raman spectrum of powdered hydroxyapatite in wavenumber region used for mapping.

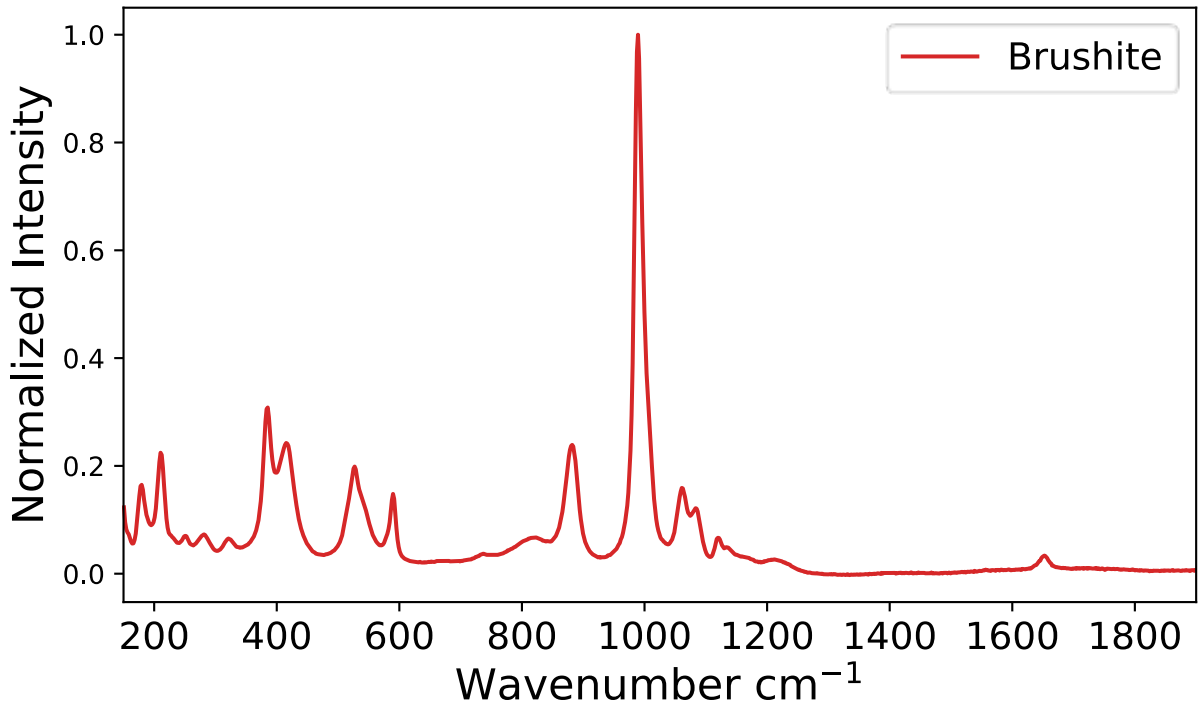

Figure 3.16: Raman spectrum of powdered COD in wavenumber region used for mapping.

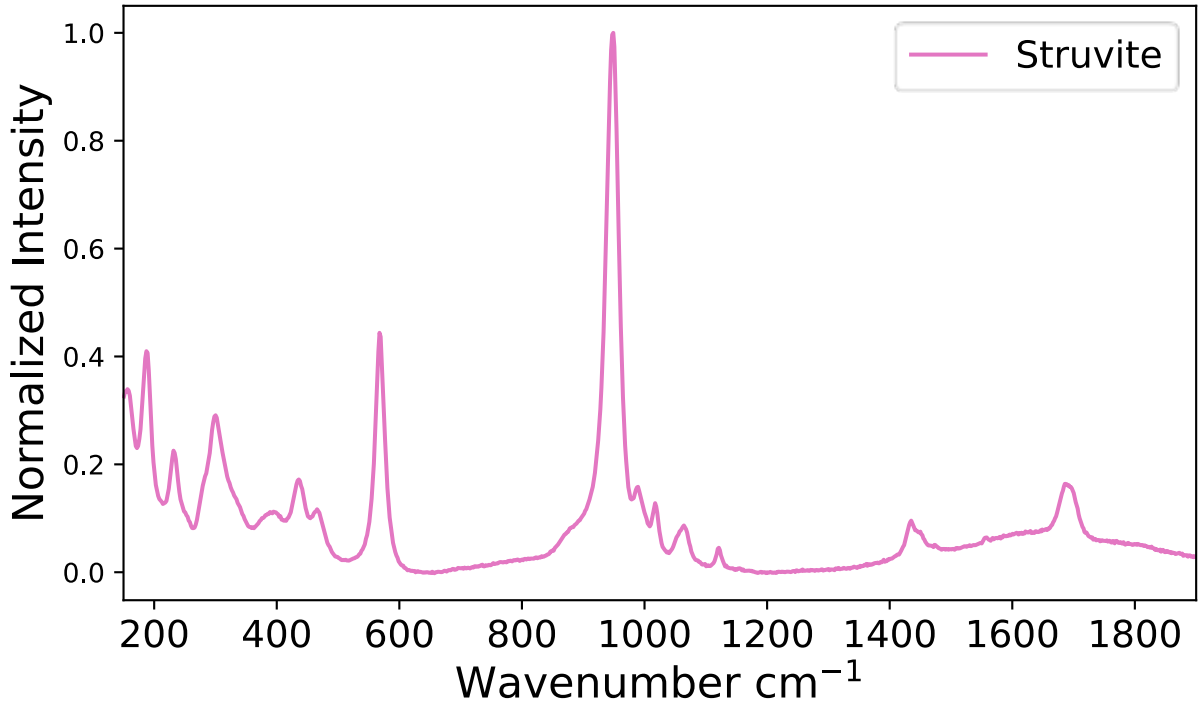

Figure 3.17: Raman spectrum of powdered COD in wavenumber region used for mapping.

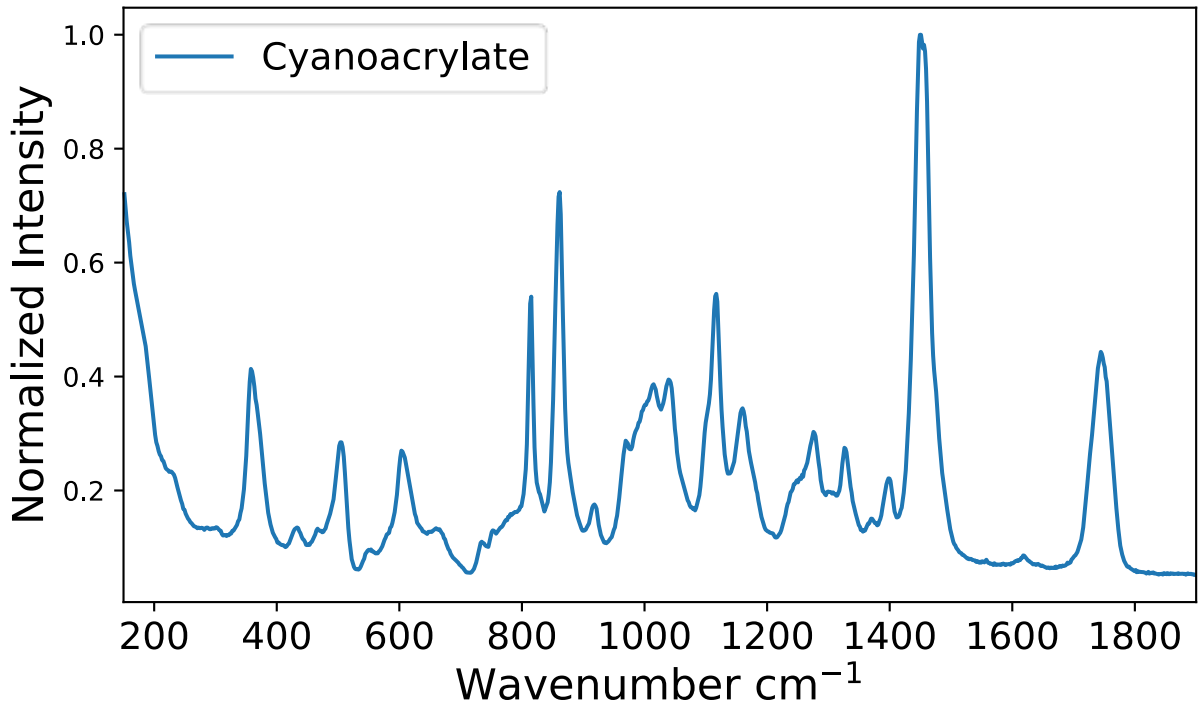

Figure 3.18: Raman spectrum of cyanoacrylate glue, cured and polished.

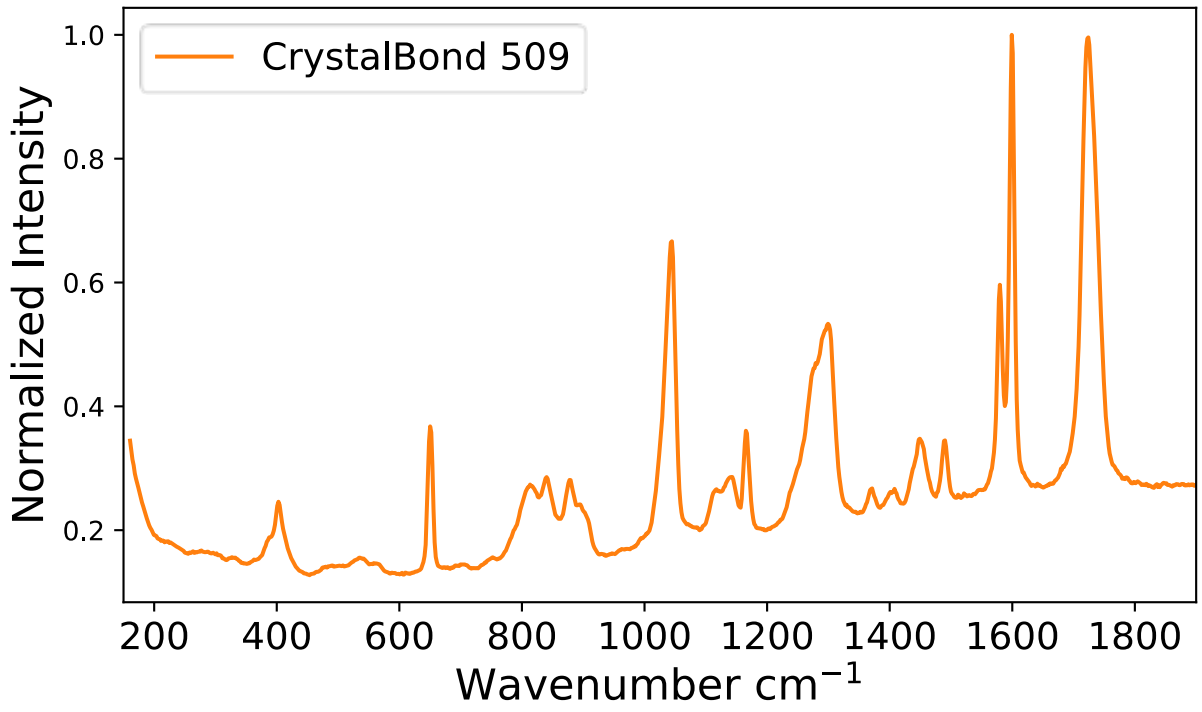

Figure 3.19: Raman spectrum of clear CrystalBond 509, polished.

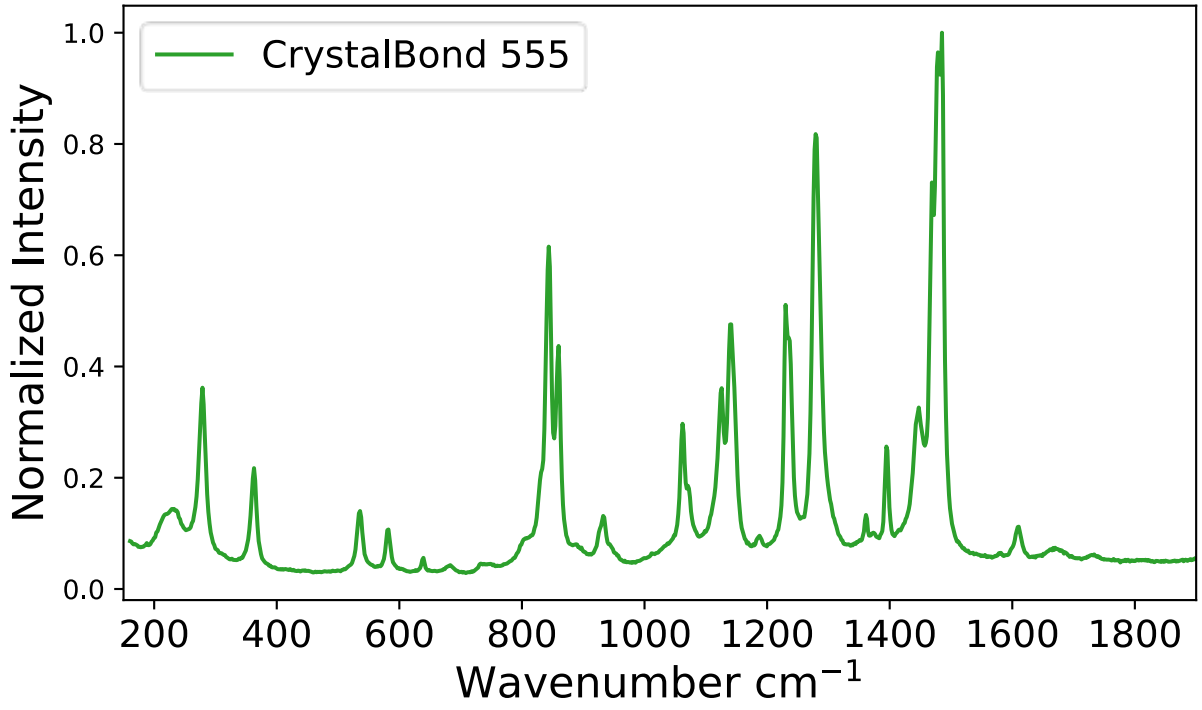

Figure 3.20: Raman spectrum of CrystalBond 509.

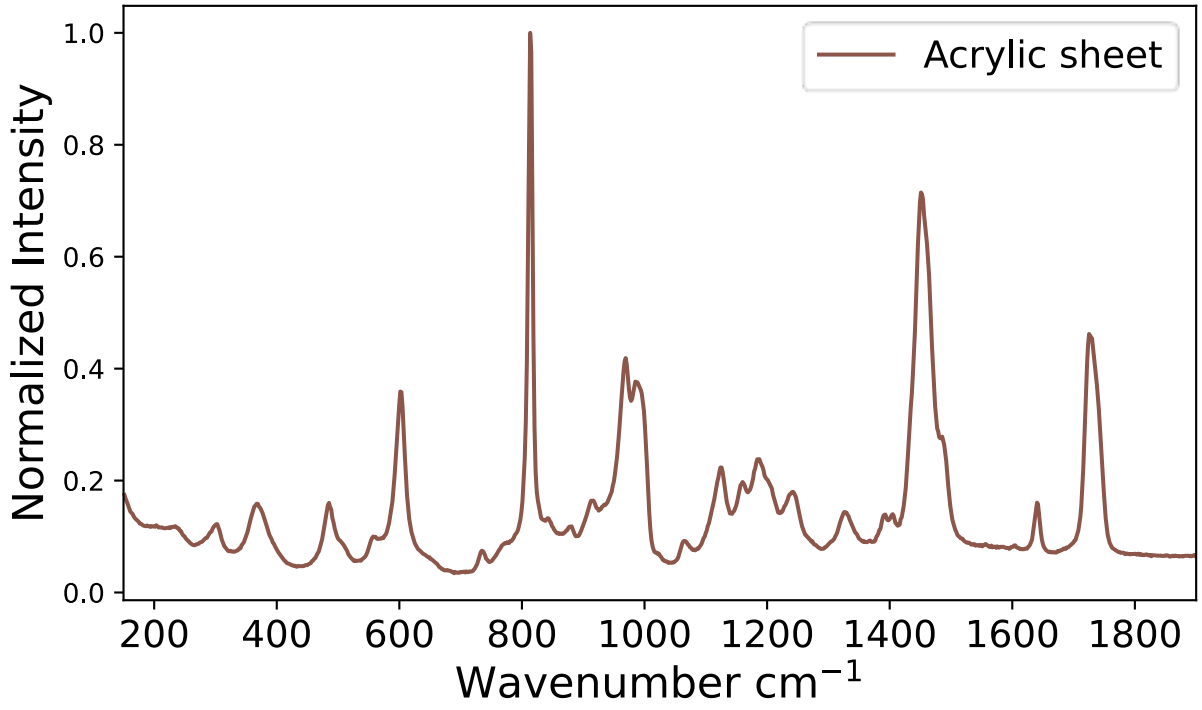

Figure 3.21: Raman spectrum of acrylic sheet, polished

Chapter 4 Improved Kidney Stone Models[A]

Research into the mechanisms of stone ablation by near-infrared (NIR) laser lithotripters often suffers from a lack of quality stone phantoms. Intact human stones removed by percutaneous nephrolithotomy are usually the ideal model for use in lithotripsy studies; however, the inherently heterogeneous nature of stones can make sample-to-sample comparisons difficult. As an alternative to human stones, many researchers use kidney stone models, commonly referred to as phantoms, made of gypsum plasters exemplified by BegoStone, a high-strength plaster originally used for research in extracorporeal shockwave lithotripsy (ESWL).[3,132–135] BegoStone in various formulations can mimic the strength and acoustic properties of human stones which makes it excellent for research in mechanical forms of lithotripsy.[3,132,133] Despite their utility in ESWL research, BegoStone cannot accurately mimic the photophysical, chemical, and thermal properties of the various types of human stone given these properties are inherent to the materials forming stones.[53,57,60,136] As NIR lasers ablate stones via a photothermal mechanism, new phantoms composed predominantly of the minerals found in human stones is essential particularly for research in which chemical composition is central.

The two primary strategies used for artificial phantoms have been plaster development and polymer/mineral composites. The earliest phantoms described were formed of plasters of unspecified composition. Later works used plaster of Paris specifically, indicating a calcium

[A] Adapted from:
Robinson, J. W.; Marom, R.; Ghani, K. R.; Roberts, W. W.; Matzger, A. J. Performance of Brushite Plaster as Kidney Stone Phantoms for Laser Lithotripsy. *Urolithiasis* **2023**, *52* (1), 10. https://doi.org/10.1007/s00240-023-01505-8.

sulfate binder with unknown fractions of silicates as filler. Polymer/mineral composites composed of stone-forming compounds bound by formaldehyde crosslinked gelatin have been formed through pharmaceutical granulation and coating techniques.[3,137] Simpler composites composed of poly(ethylene-co-vinyl acetate) were developed in this lab though these have polymer volume fractions that exceed 20%, much greater than the organic content of typical kidney stones.[60]

A high-quality kidney stone phantom should accurately mimic the behavior of human stones during laser lithotripsy. Ablation volumes should be similar for the same laser settings. Phantoms should have similar bulk composition. Phantoms should produce a range of particle sizes including larger, >1 mm fragments. BegoStone and other gypsum plaster phantoms fail all three criteria for brushite stones, and earlier polymer/mineral composites developed in our lab only reproduce single-pulse ablation volumes. BegoStone typically produces smaller particles than observed in human stones making it unsuitable for testing fragmentation performance of new laser lithotripters.[45,138]

This chapter primarily focuses on work performed developing and characterizing brushite plaster phantoms containing >90% brushite that accurately reproduce single-pulse laser ablation crater volumes of human brushite stones. These brushite phantoms also fragment more readily than BegoStone allowing a greater array of lithotripsy techniques to be studied. Preparation and basic characterization of struvite plaster phantoms and chitosan/COM composites are also discussed with suggestions for improvement in Chapter 5.

4.1 Materials and methods

4.1.1 Brushite plasters

Brushite phantoms for kidney stones were adapted from the many examples of calcium phosphate cement for bone repair.[139–145] Solid components of the plaster formulation include

calcium dihydrogen phosphate monohydrate ($Ca(H_2PO_4)_2 \cdot H_2O$), β-tricalcium phosphate (β-$Ca_3(PO_4)_2$), and sodium pyrophosphate decahydrate ($Na_4P_2O_7 \cdot 10H_2O$). These components must be kept separate until phantoms are prepared as $Ca(H_2PO_4)_2 \cdot H_2O$ slowly forms monetite when mixed with β-tricalcium phosphate. The liquid phase of the phantoms is an aqueous solution of phosphorous acid, H_2PHO_3 (note this is *phosphorous* acid not *phosphoric* acid which causes rapid setting of these plaster formulations). β-Tricalcium phosphate was synthesized from brushite and calcium carbonate as described below; all other reagents were purchased.

A complete listing of brushite plaster formulations is included in Table 4.1. Typical plasters were formed using a 10:9 mole ratio of β-Ca_3PO_4:$Ca(H_2PO_4)_2 \cdot H_2O$ with masses of 2.31 ± 0.01 g β-$Ca_3(PO_4)_2$ and 1.69 ± 0.01 g $Ca(H_2PO_4)_2 \cdot H_2O$. Sodium pyrophosphate decahydrate was added to most formulations at 1 wt. % total solid mass to increase setting time of the plasters. To form the plaster, solid $Na_4P_2O_7 \cdot 10H_2O$ and 1.60 mL of phosphorous acid solution were added to $Ca(H_2PO_4)_2 \cdot H_2O$ powder and stirred for 30 seconds. This completely dissolved sodium pyrophosphate and partially dissolved $Ca(H_2PO_4)_2 \cdot H_2O$ resulting in a suspension of mixed calcium phosphates. β-$Ca_3(PO_4)_2$ was then added to the suspension in ≈1/4 volume increments with ≈15 s of stirring for each increment to form a uniform paste. A folding action was used rather than stirring as the paste thickened. After β-$Ca_3(PO_4)_2$ was fully incorporated, the plaster was loaded into the plunger end of disposable plastic syringes by spatula. For formulations with 4 g solid and 1.6 mL liquid a 3 mL syringe was typically used. A 0.8×50 mm needle was attached to the end of the syringe after loading and the plunger was depressed to expel air until the plaster visibly reached the metal needle of the syringe. The needle was capped, and with the plunger in place, the plaster-filled syringe was left in a 37° C oven to set overnight. After setting overnight, the needle and

plunger were removed from the syringe and the plaster was allowed to air dry for an additional day before being cut by band saw into 1 cm length phantoms.

4.1.1.1 β-Tricalcium phosphate synthesis

β-$Ca_3(PO_4)_2$ was synthesized via a solid-state reaction carried out at 900 °C. The precursor powders, brushite and calcium carbonate, were weighed into a 500 mL jar in a 2:1 mole ratio (3.439:1 mass ratio) with final masses 171.94 g brushite and 50.00 g calcium carbonate. To ensure mixing, brushite and calcium carbonate were layered in increments of ≈17.2 g of brushite and ≈5 g of calcium carbonate with 10 layers for each compound. The jar was then shaken by hand for at least one minute. The jar was then placed on rollers (Ika Roller 6 Basic) to continue mixing overnight, followed by an additional one minute of shaking to ensure thorough mixing.

Powders were finely ground using a ball mill (mixing-type, Quantachrome MillPrep) to improve intimate contact between brushite and calcium carbonate for the solid-state reaction. Milling cups (50 mL volume) were filled approximately halfway with the mixed brushite + calcium carbonate powders. Two 1 cm steel balls were then placed in the milling cup for grinding at 20 Hz for 30 minutes. The powder was transferred to alumina boats and compacted for better contact. For the solid-state reaction, the powders were heated in a muffle furnace to 900 °C at 5 °C/minute, held at 900 °C for 16 hours, and cooled to room temperature at 5 °C/minute. Only β-$Ca_3(PO_4)_2$ is detectable by X-ray diffraction for carefully prepared samples. In cases where intimate contact between calcium carbonate and brushite powder is poor in the alumina boats, calcium pyrophosphate and calcium oxide are observed in the final mixture.

Attenuated total reflectance infrared (ATR IR) spectroscopy was used to measure composition of phantoms. Calcium phosphate composition was calculated using partial least squares method in the TQ Analyst software from Thermo Scientific using gravimetrically prepared standards. Crater

volumes were measured using images taken by a Hirox RH-2000 microscope which were assembled into 3D reconstructions by the Hirox's software suite. Statistical tests were performed using Python (v3.11.4) and SciPy (1.11.1).

Crater volume measurements for human brushite stones were conducted on fragments from a single human stone with n=12 total craters measured. This stone had a reported composition of 94% brushite, 3% hydroxyapatite, and 3% protein from bulk analysis performed externally and included as a part de-identified stone library. This is the same brushite stone measured in Section 3.3.4 (Figure 3.5) which clearly contains COM and COD in addition to brushite and apatite indicating poor accuracy in the bulk composition measurement.

Table 4.1: Brushite plaster formulations.

Sample	β-$Ca_3(PO_4)_2$ / g	$Ca(H_2PO_4)_2 \cdot H_2O$ / g	$Na_4P_2O_7 \cdot 10\ H_2O$ / g	$[H_2PHO_3]$ / M	Additional Brushite / g	Liquid volume / mL
$A_{0.60}$	2.31	1.69	0.04	0.60	0	1.60
$A_{0.80}$	2.31	1.69	0.04	0.80	0	1.60
$A_{1.20}$	2.31	1.69	0.04	1.20	0	1.60
$A_{1.79}$	2.31	1.69	0.04	1.79	0	1.60
$A_{2.39}$	2.31	1.69	0.04	2.39	0	1.60
$B_{2.39}$	1.16	0.84	0.08	2.39	1.00	1.20

4.1.2 Single-pulse lithotripsy

Single-pulse craters were produced using a Lumenis Pulse 120H Ho:YAG laser with a Flexiva 200 μm nominal diameter fiber. Prior to ablation, samples were placed in water until bubbling from air displacement was no longer observed, usually about 5 minutes. For single-pulse crater measurements, laser settings were set to an energy of 1 J in short pulse mode. The laser fiber tip cleaved after every 5 craters to reduce variability from damage to the fiber tip.

Fragmentation studies were conducted on model stone cylinders with 10 mm diameter and 10 mm length cut from molded rods. Cylindrical phantoms were held lengthwise by rubber tubing

that was cut lengthwise to remove 10-40% of tubing radially. To induce fragmentation, laser fibers were manually held in contact with the phantoms as the laser was fired with 1 J pulses at 10 Hz for an average power of 10 W. With the fiber in near-continuous contact with the phantoms, holes were drilled along the diameter of the cylinders. The first hole was drilled at the center (x=5 mm) of each phantom with subsequent holes drilled at 2.5 and 7.5 mm, respectively. If fragmentation occurred, drilling was halted and the total energy required to induce fragmentation was recorded along with the number of holes drilled.

4.2 Results and Discussion

4.2.1 Quantitative ablation performance

Ablation volumes from 1 J, single-pulse experiments are summarized in Figure 4.1. A human brushite stone had average crater volumes of 0.128 ± 0.015 mm^3 (n=12). Uncertainties are reported as ± 1 standard deviation). Phosphorous acid concentration was found to be directly related with crater ablation volume. One-way ANOVA of crater volumes suggests the means differ for the various formulations (p=0.00005). Brushite formed an average of 90±2% of stone mass for formulation A samples with $Ca(H_2PO_4)_2 \cdot H_2O$, β-$Ca_3(PO_4)_2$), and monetite ($CaHPO_4$) forming the remainder of the stone mass (Table 4.2). Higher phosphorous acid concentration leads to a higher fraction of the more acidic $Ca(H_2PO_4)_2 \cdot H_2O$ compared to tricalcium phosphate.

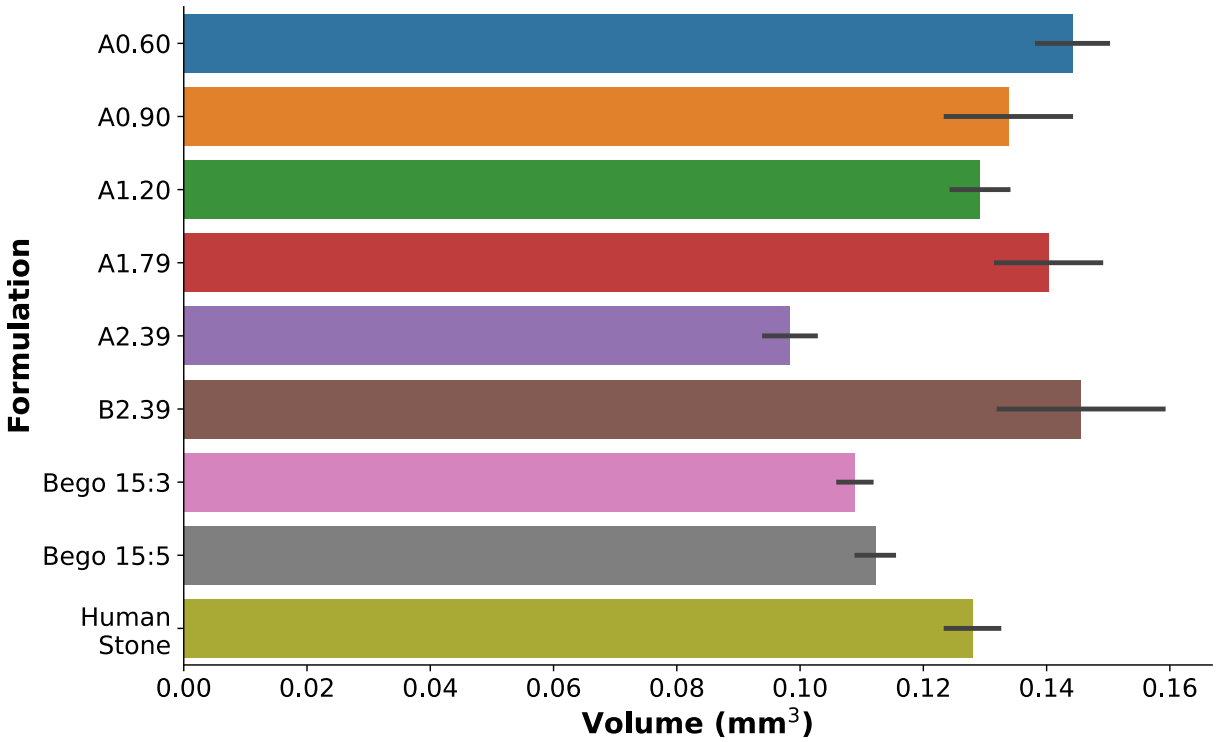

Figure 4.1: 1 J, single-pulse crater volumes for differing plaster formulations. Error bars indicate ±1 standard devation.

Table 4.2: Table of ablated crater volumes and mole fractions of calcium phosphates. Composition percentages may not add up to 100% due to rounding or presence of unidentified compounds.

Formulation	Crater volume	Brushite	β-$Ca_3(PO_4)_2$	$Ca(H_2PO_4)_2 \cdot H_2O$	$CaHPO_4$
	(mm^3, ±1σ)	%	%	%	%
$A_{0.60}$	0.144±0.028	90	7	1	1
$A_{0.80}$	0.134±0.023	89	7	2	2
$A_{1.20}$	0.129±0.018	89	5	5	2
$A_{1.79}$	0.140±0.027	91	4	5	0
$A_{2.39}$	0.098±0.014	90	3	9	0
$B_{2.39}$	0.146±0.042	83	0	14	2

All samples of formulation $A_{0.60}$-$A_{1.20}$ fractured into large, >1 mm fragments during the drilling procedure. Phantoms from formulations A1.79, A2.39, and BegoStone did not always fracture (Figure 4.3-Figure 4.9). Fragmentation was more likely to occur during drilling of the second hole for 10 mm samples. For 5 mm samples all samples fragmented while drilling suggesting fracture is more likely for smaller phantoms. For 10 mm phantoms, the cumulative energy required for

fracture averaged 0.17±0.08 kJ. These energies were not significantly different from the amount of energy needed to fracture BegoStone phantoms (0.25±0.11 kJ).

The variation in number of drilled holes and energy required for stone fracture reflects the heterogeneity among phantoms. This is not unexpected, as loading a solidifying plaster into syringe bodies does not result in perfectly uniform phantoms. As kidney stones themselves are heterogeneous, variation in phantoms is not considered problematic.

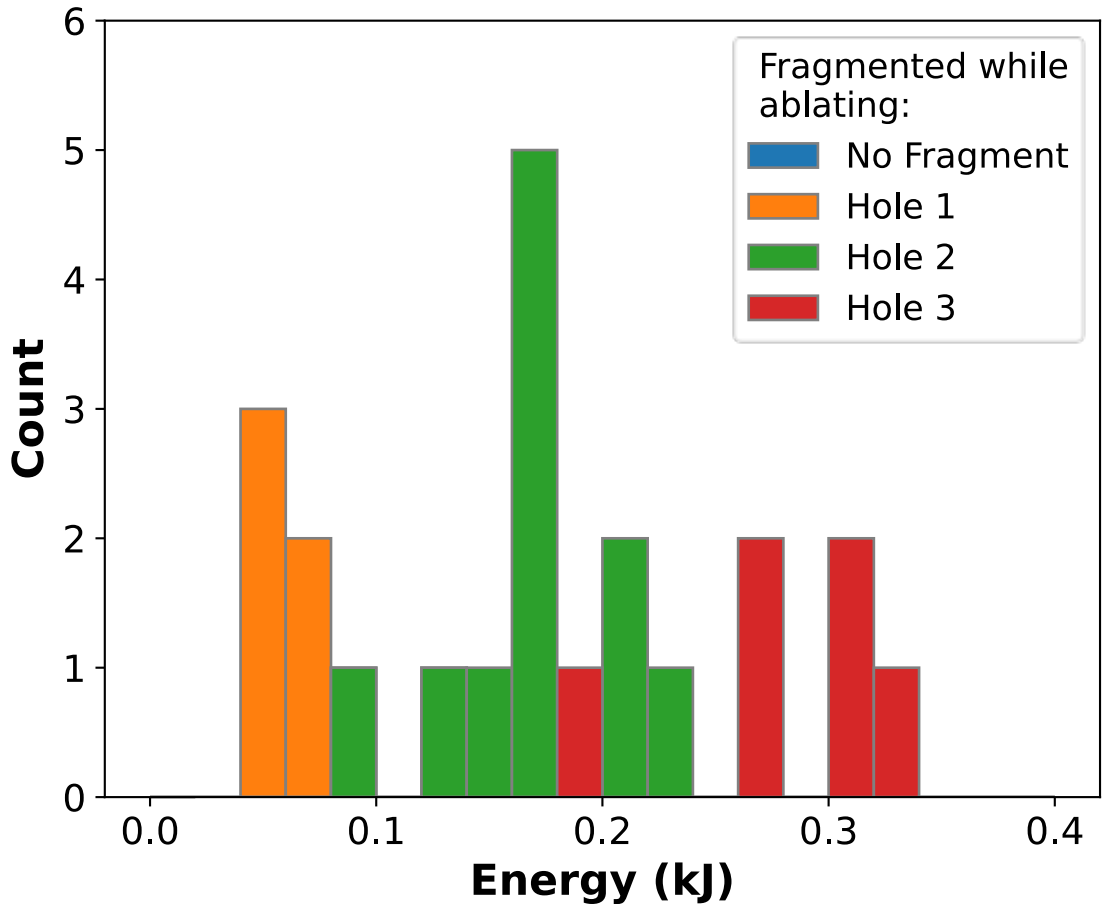

Figure 4.2: Summary histogram of fragmentation occurrence compared to laser energy required for formulations ($A_{0.60}$, $A_{0.90}$, and $A_{1.20}$).

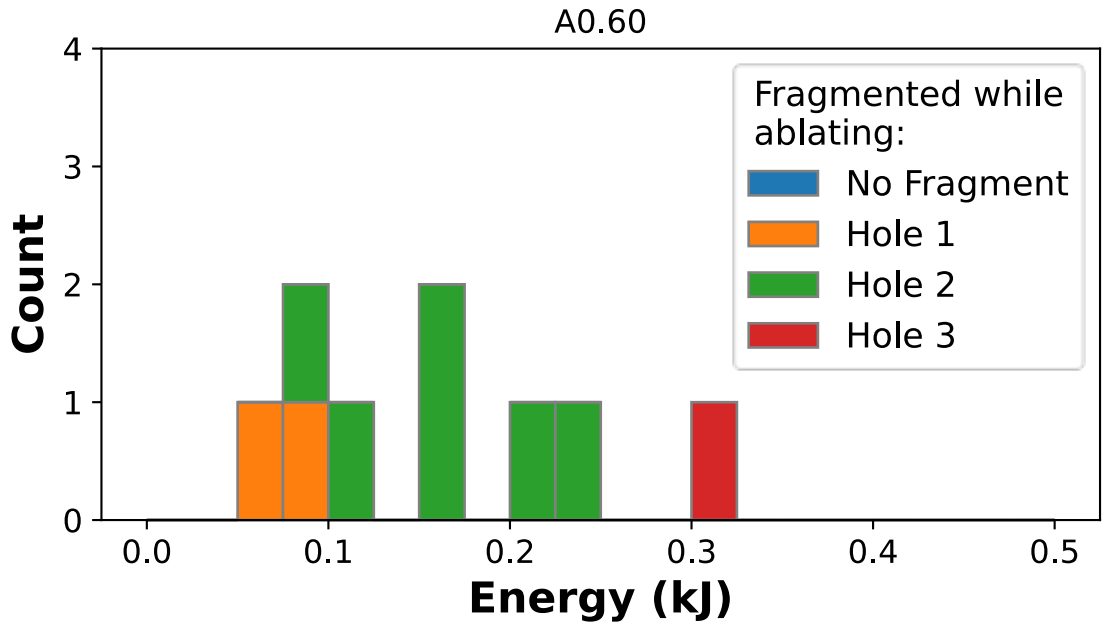

Figure 4.3: Histogram of energy required to fragment stone for formulation A0.60 The number of drilled holes is indicated by color.

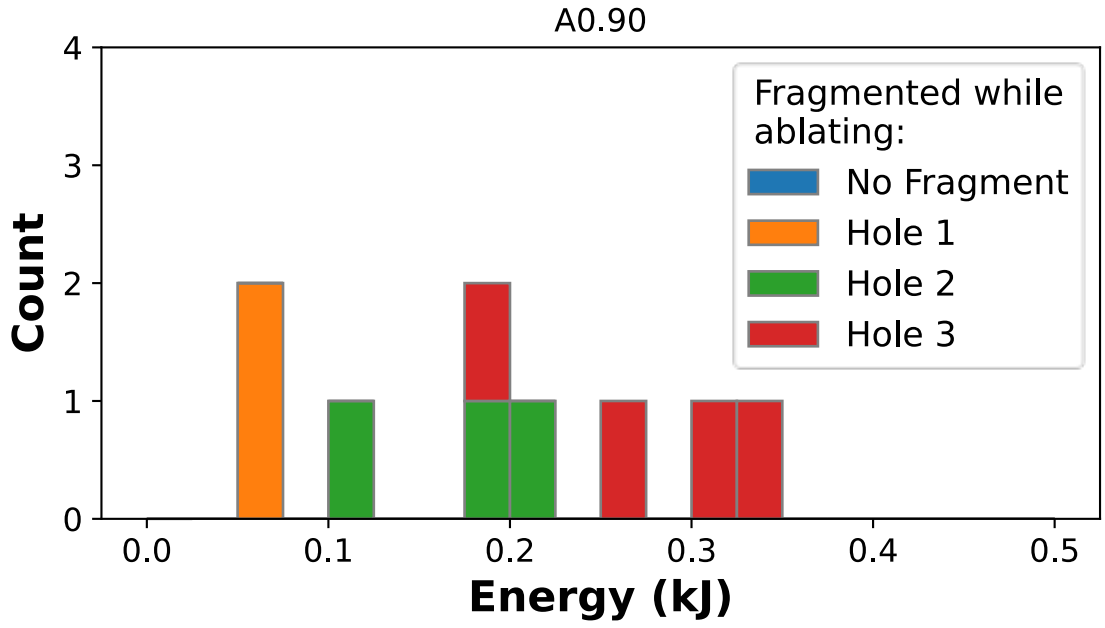

Figure 4.4: Histogram of energy required to fragment stone for formulation A0.90 The number of drilled holes is indicated by color.

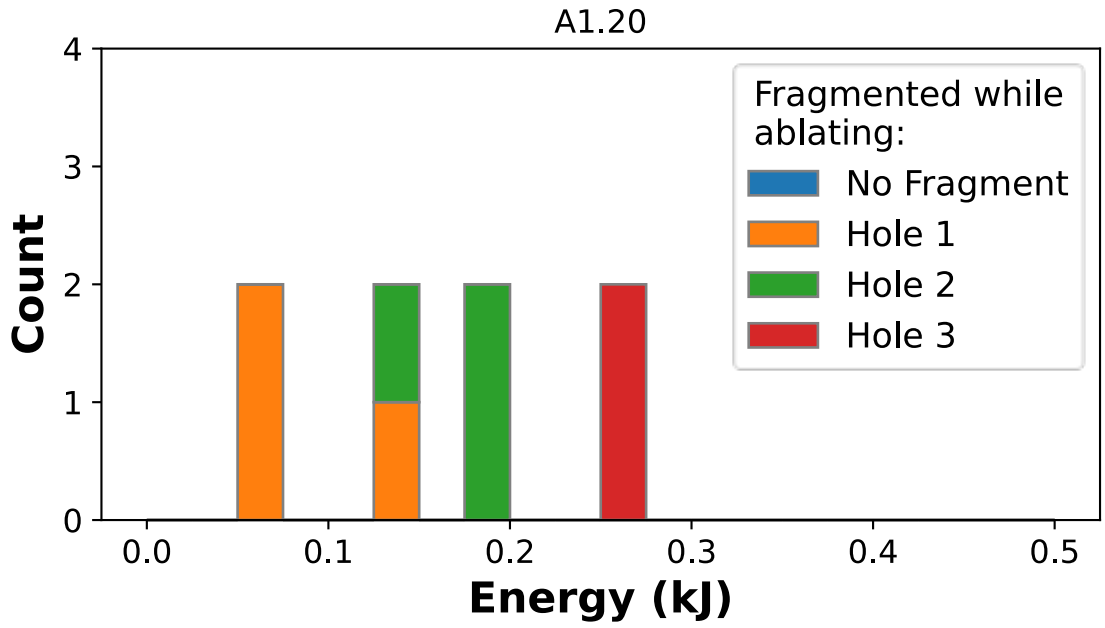

Figure 4.5: Histogram of energy required to fragment stone for formulation A1.20 The number of drilled holes is indicated by color.

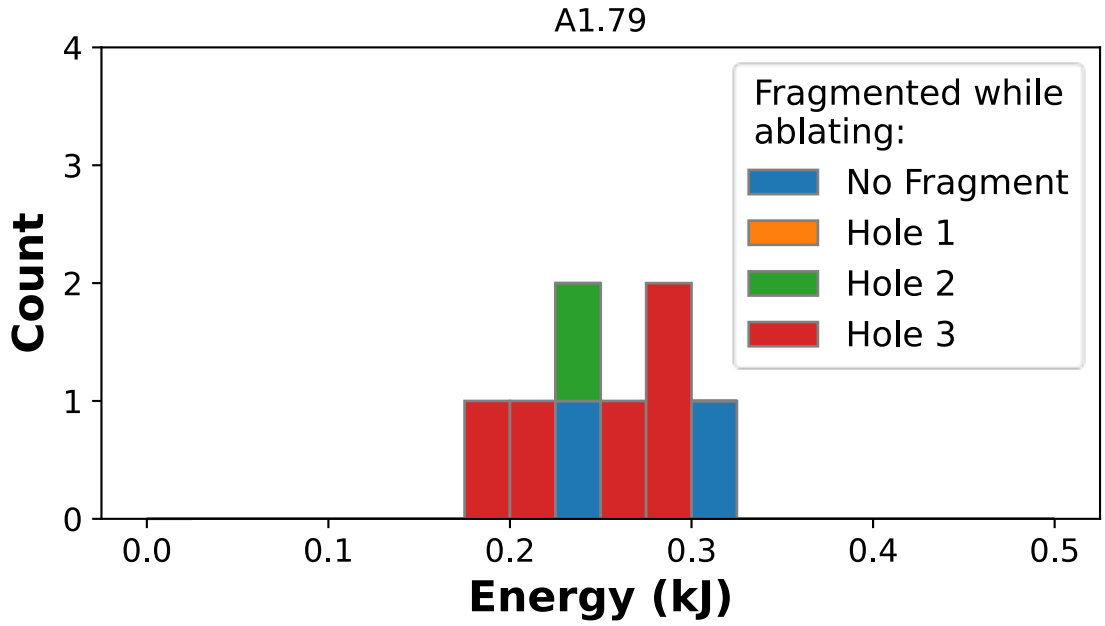

Figure 4.6: Histogram of energy required to fragment stone for formulation A1.79 The number of drilled holes is indicated by color.

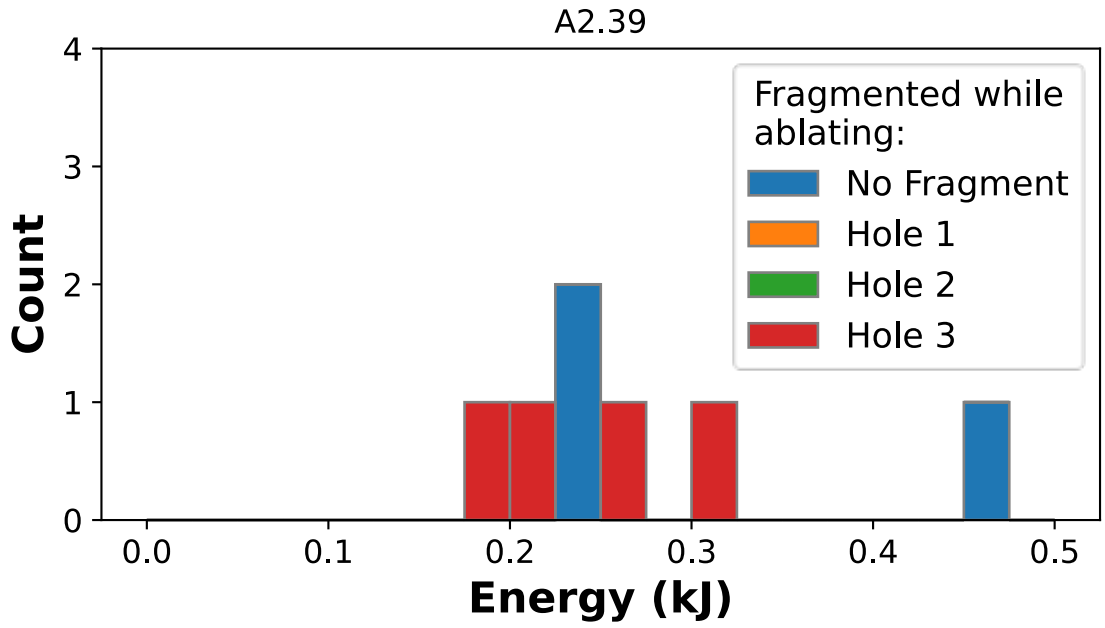

Figure 4.7: Histogram of energy required to fragment stone for formulation A2.39 The number of drilled holes is indicated by color.

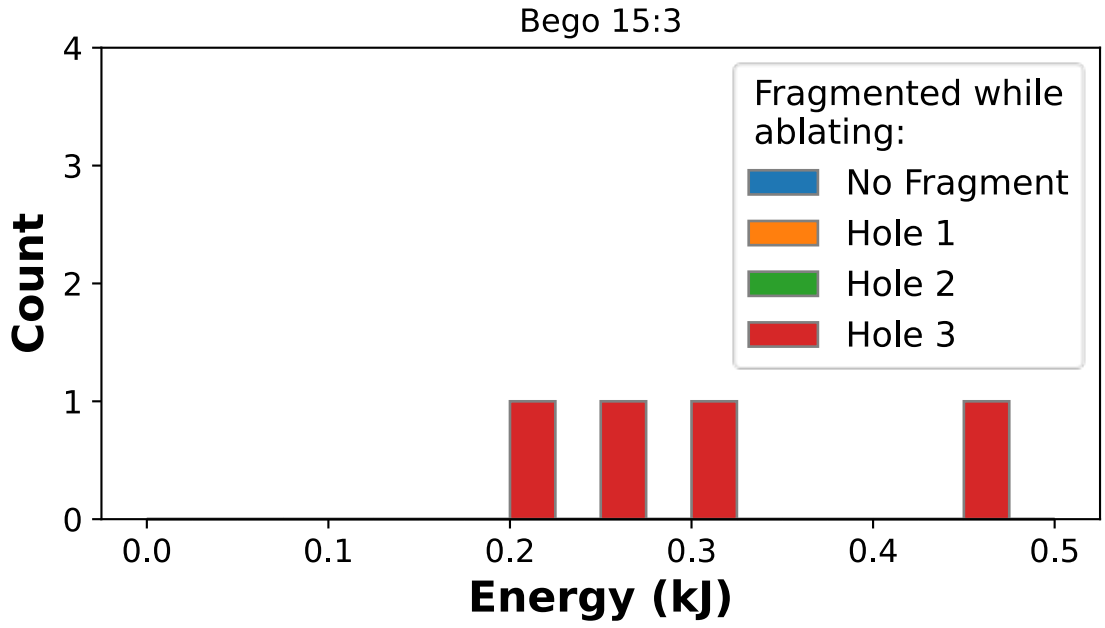

Figure 4.8: Histogram of energy required to fragment stone for BegoStone with a 15:3 ratio of powder:water. The number of drilled holes is indicated by color.

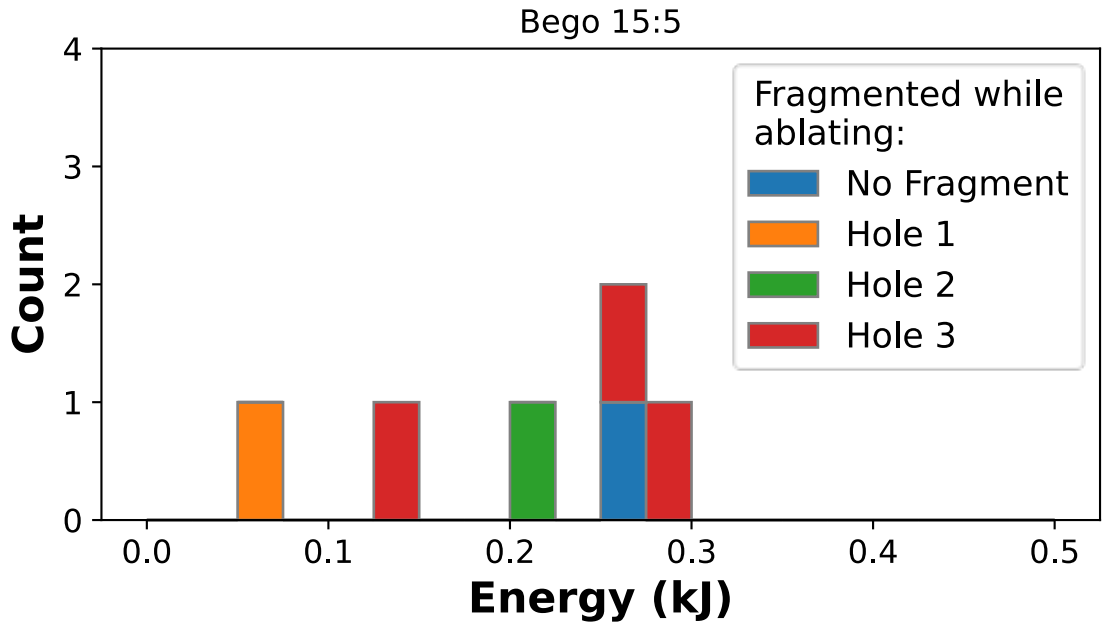

Figure 4.9: Histogram of energy required to fragment stone for BegoStone with a 15:5 ratio of powder:water. The number of drilled holes is indicated by color.

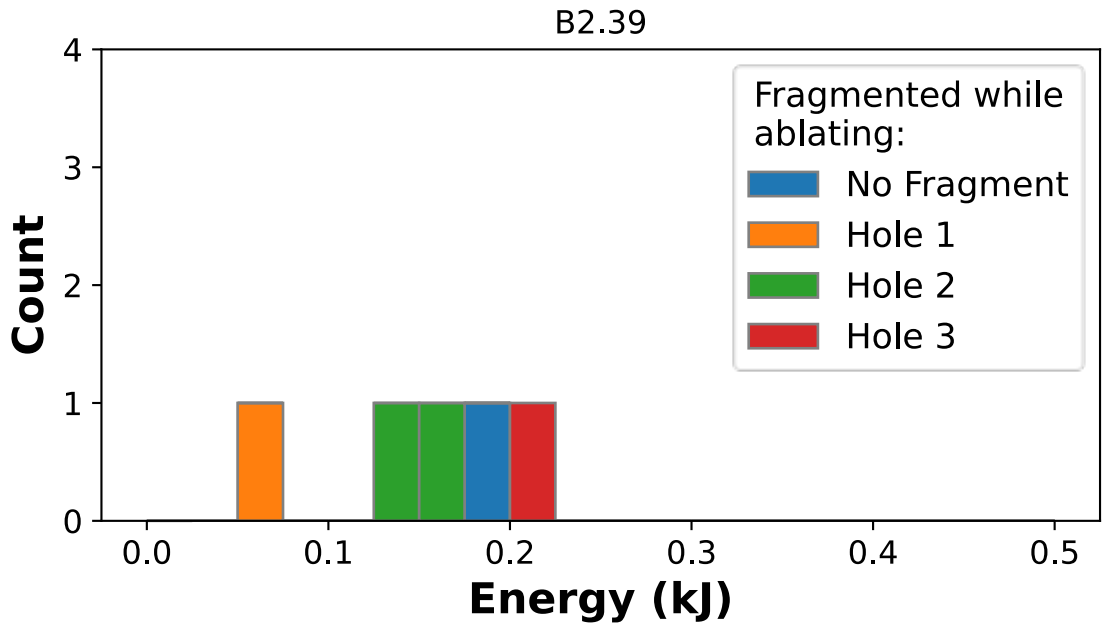

Figure 4.10: Histogram of energy required to fragment stone for phantoms of formulation $B_{2.39}$. The number of drilled holes is indicated by color.

4.2.2 Microstructure

SEM images of brushite stones and phantoms are shown in Figure 4.11 to demonstrate differences in microstructure. Brushite kidney stones often show radial organization and alignment of crystals while plasters result in random crystal orientations (Figure 4.11a). Slow-growing, compact stones will tend have pores filled in via dissolution-redeposition to minimize surface area while solvents evaporation in plaster formulations tends to leave an open pore structure behind (Figure 4.11c).

Anecdotally, urologists try to target visible boundaries within stones to encourage breakage. Fractures are believed to travel along visible boundaries more easily, perhaps due to relatively poor binding strength between layers. In contrast to human stones, plasters mostly lack clear boundaries as they are composed of small, randomly oriented crystallites that leading to phantoms with more uniform strength than human stones. To introduce artificially boundaries where cracks might propagate more effectively, longer brushite crystals 1-3 mm in length were added to the $B_{2.39}$ formulation. Higher phosphorous acid concentrations were required for this formulation to increase working time. Phantoms of $B_{2.39}$ did fragment more readily that phantoms of $A_{2.39}$, suggesting this approach may be viable with further testing, ideally using formulations $A_{0.60}$-$A_{1.20}$ as a basis due to their better performance and higher brushite concentrations compared to $A_{2.39}$. The mechanically fractured samples in Figure 4.11b shows the exposed (010) planes of added brushite crystals suggesting crack propagation did occur along elongated crystals.

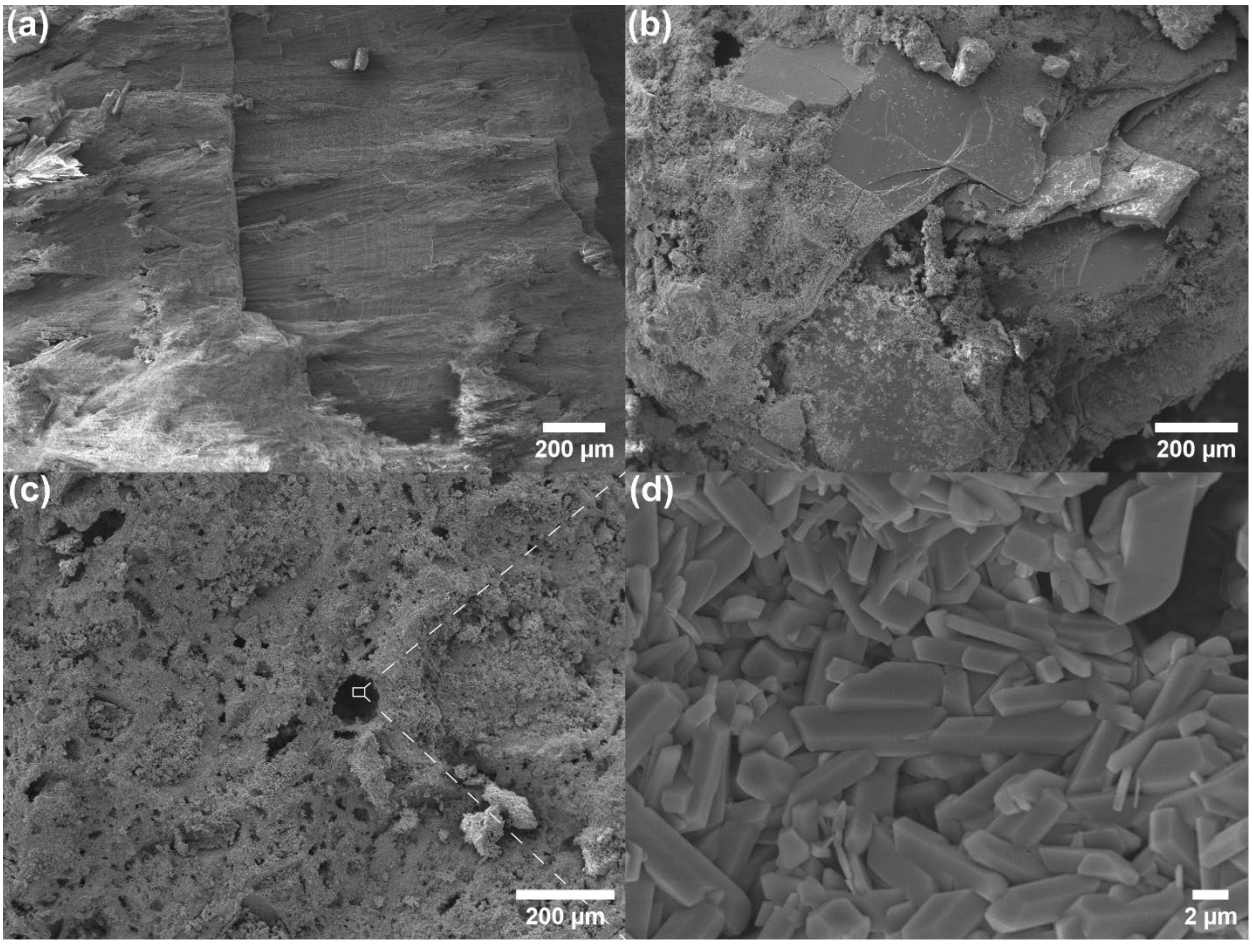

Figure 4.11: SEM images of brushite stone and plaster. (a) Human brushite stone. (b) Formulation $B_{2.39}$. (c) Formulation $A_{1.20}$. (d) Image of region of interest indicated in (c).

4.2.3 Examples of fracture

Figure 4.12 shows two examples of brushite phantom fracture through high-speed imagery with (a) showing fracture for a phantom of formulation $A_{1.20}$ and (b) showing fracture at the edge of a phantom of formulation $B_{2.39}$. At 50 µs after t=0, the last frame at which no laser-induced motion is apparent, phantoms appear bright due to luminescence produced by an undetermined mechanism believed to be incandescence or triboluminescence. Cracks are visible by 100 µs, a time scale shorter than laser pulse duration for both Ho:YAG lasers and Tm fiber lasers.[146] Bubble expansion continues until 250 µs, a similar time frame as the pulse duration of 1 J, short pulses from the Lumenis Pulse 120H Ho:YAG used for fragmenting. Bubble collapse from 500-1250 µs

draws fragments closer together which is potentially advantageous during surgery due to lower retropulsion.

Crack propagation leading to fragment formation occurred on <100 μs time scale for all fragmentations observed by high-speed imagery strongly suggesting mechanical failure during bubble expansion rather than subsequent cavitation. Thulium fiber lasers tend to increase single-pulse energies by increasing pulse duration rather than increasing peak power. If fragmentation is primarily caused by high power or pressure transients, increasing pulse energy by increasing pulse length may be detrimental to patients as energy deposited by laser pulses after ≈100 μs will likely increase fluid temperatures without a significant change in fragmentation performance.

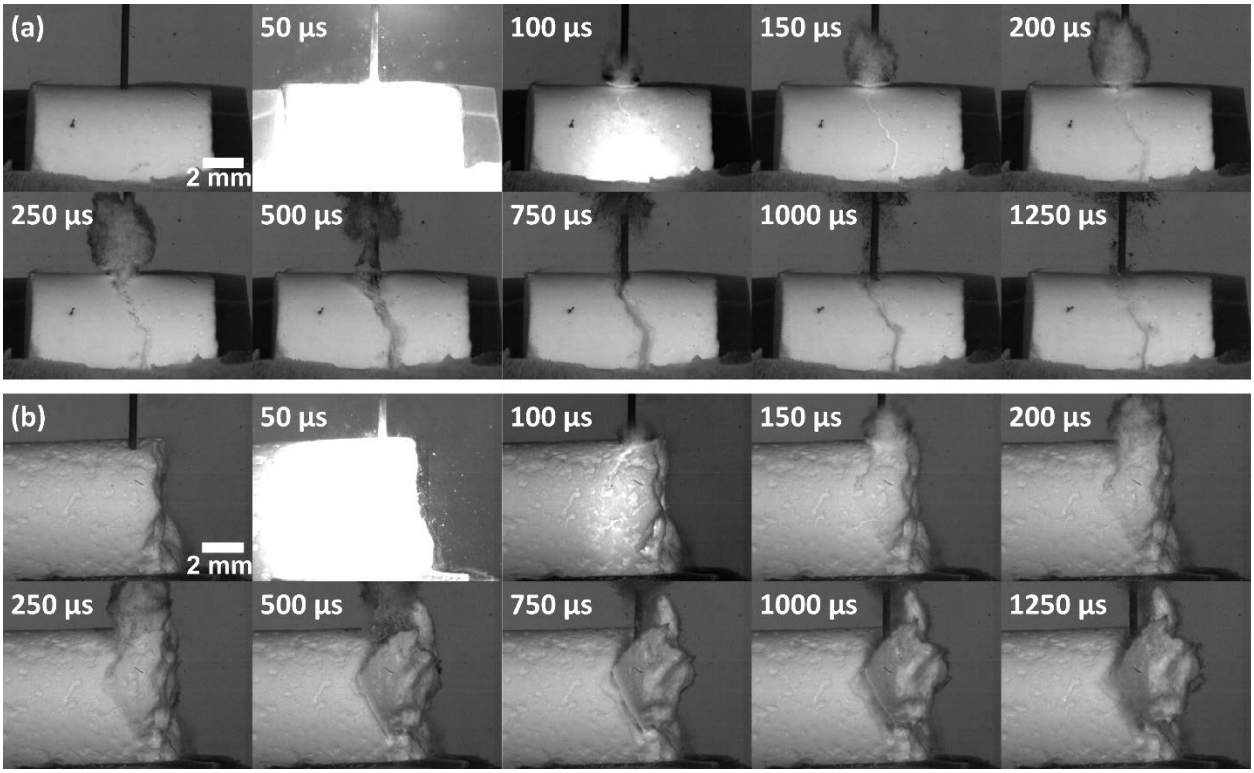

Figure 4.12: High-speed imagery of brushite phantoms fragmenting during laser ablation. (a) Full cross-sectional fracture of formulation $A_{1.20}$. (b) Edge fragmentation of formulation $B_{2.39}$.

4.3 Conclusions

The brushite plasters developed here have superior composition and laser ablation performance compared to existing artificial kidney stone models. Brushite plaster phantoms fragment more easily than gypsum-based BegoStone phantoms and ablation characteristics can be adjusted through variations in the plaster formulation. High-speed imaging of brushite phantom fragmentation demonstrated that fracture occurs on <100 μs time scales. This suggests increasing laser pulse energy by increasing laser pulse duration will not lead to improved stone fragmentation though some thulium lasers have adopted this approach. Further development of phosphate plasters may lead to new struvite and hydroxyapatite phantoms that will provide urology researchers with a larger library of artificial models to study near-infrared laser lithotripsy and post-surgical dissolution of stone fragments to reduce stone recurrence.

Chapter 5 Future Work

Future work at the intersection of chemistry and urolithiasis has several possible directions. Among these, research focusing on patient outcomes after surgery and prevention of stones should be kept foremost. To address these general areas, I believe development of new, more accurate kidney stone phantoms is most important as these are a necessary precursor for testing post-surgical dissolution therapies that show promise in reducing stone recurrence.[147] Fundamental insight into stone growth may also aid in this endeavor, especially in the context of dissolution therapy without surgical intervention. Developing new mineral imaging techniques is not likely to yield much new information, though orientation-dependent Raman microscopy is discussed further as it may be useful in the analysis of calcium oxalate kidney stones. Potential future applications of this work via computation modeling are also briefly discussed.

5.1 Additional phantoms

Beyond the most successful brushite phantoms, numerous trials have been performed with struvite and COM, and uric acid plasters and/or polymer composites. Of these, struvite plasters and COM composites are the best developed and are discussed below.

5.1.1 Struvite plaster

Of the various struvite plasters I have developed and tested, the best performing are formed from a mixture of 2:1 $Mg_3(PO_4)_2$:$(NH_4)_2HPO_4$ by mass (≈1:1 mole ratio), typically 1.6 g $Mg_3(PO_4)_2$ and 0.8 g $(NH_4)_2HPO_4$. The mixed solids are ground together in an agate mortar and

pestle along with 3.3 mL of deionized water to form a homogeneous suspension. 1.04 mL 30% ammonia solution (concentrated ammonium hydroxide) is then added. This leads to rapid seizing at the surface of the suspension which must be ground until it is workable and homogeneous again, ≈1 minute, at which the suspension can be placed in molds to set overnight.

The struvite phantoms have single-pulse crater ablation volumes (0.22±0.01 mm^3) that are not significantly different from those of human stones (0.20±0.01 mm^3) for 1 J, short pulses from a Ho:YAG laser. Despite success in single-pulse experiments, the molar composition is only 77±2% $MgNH_4PO_4 \cdot 6H_2O$ with 5±1% $Mg_3(PO_4)_2$ and 18±2% $MgHPO_4 \cdot 3H_2O$ by powder X-ray diffraction, a much lower struvite percentage than expected in near-pure struvite stones (>90% struvite).

As noted earlier, many struvite stones contain carbonate apatite in addition to struvite. Like apatites, anhydrous trimagnesium phosphate lacks water in its structure and likely has similarly low absorption at NIR laser wavelengths (water adsorption on $Mg_3(PO_4)_2$ powders has made this difficult to verify). Thus, the presence of unreacted $Mg_3(PO_4)_2$ in this plaster is not considered a major problem. In contrast, $MgHPO_4 \cdot 3H_2O$ is expected to have an impact on NIR absorption and its presence needs to be reduced for successful application of struvite plasters.

$MgHPO_4 \cdot 3H_2O$ precipitation competes with struvite precipitation during plaster setting and, as a less soluble product, can form from dissolving struvite.[126,148,149] Addition of struvite crystals offers one route to higher struvite fraction. Phantoms have been formed with up to 50 wt. % commercial struvite powder; unfortunately, some commercial struvite powder contains >5% combined mass of hannayite ($Mg_3(NH_4)_2(HPO_4)_4 \cdot 8H_2O$) and dittmarite ($MgNH_4PO_4 \cdot H_2O$). Efforts toward synthesis of large amounts of pure struvite are ongoing for this use though struvite fraction is only expected to rise to ≈88% via addition of pure struvite crystals. Borax (sodium

tetraborate) was shown to inhibit $MgHPO_4 \cdot 3H_2O$ formation in some struvite-based plasters with higher fractions of trimagnesium phosphate.[150] Borax and other potential selective inhibitors of $MgHPO_4 \cdot 3H_2O$ growth should also be explored.

5.1.2 COM/chitosan composites

Polymer/mineral composites have been considered for use as kidney stone phantoms beginning with mineral/cross-linked gelatin composites in the late 1990s.[3,137,151,152] These early "Bon-N" stones showed promise in study of shockwave lithotripsy and produced some early results for dissolution therapy (chemolitholysis).[127,151] Despite their early promise, these gelatin composites never saw widespread adoption like gypsum plasters and their utility for laser lithotripsy is unexplored or unpublished.

For COM phantoms, chitosan/mineral composites developed during my research have shown the best agreement with human stones in terms of single-pulse ablation and composition. Composites were formed by first dissolving 2-4 wt. % high molecular weight chitosan in 0.1 M acid solutions. Dissolved chitosan solutions are then mixed with COM in equal masses to form composites that dry over several days with 2-4 wt. % chitosan. Chitosan shrinks as it dries, decreasing void volume in the final composites. Without further treatment, COM/chitosan composites from 3 wt. % chitosan dissolved in 0.1 M oxalic acid show similar single-pulse crater volumes to human stones. The 3 wt. % chitosan in the final composites is similar to the fraction of organic material in human stones.[25]

Despite the apparent success, these untreated chitosan phantoms have several problems that make them inadequate for urology experiments. The two most obvious problems are the trapping of air bubbles within the composites and the swelling of chitosan in water (Figure 5.1). As high molecular weight chitosan solutions are viscous, air entrained during mixing is trapped leaving

numerous 100-1000 μm diameter air bubbles in the phantoms which interfere with precise crater volume measurements. Swelling of chitosan leads to softening of phantoms underwater which makes models unrealistic when compared to mechanically hard COM stones.

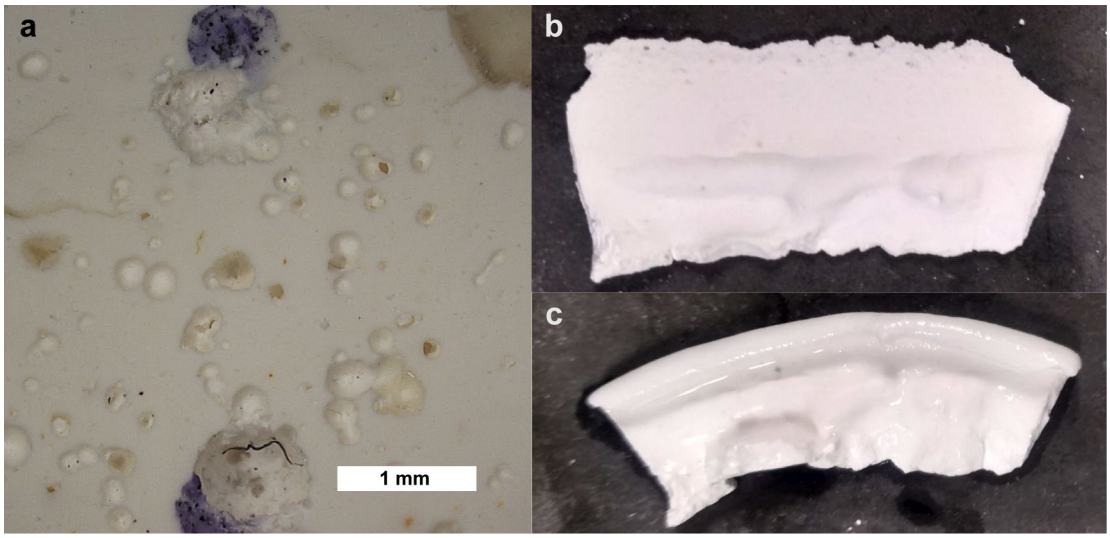

Figure 5.1: Examples of COM/chitosan composites. (a) Trapped air bubbles alongside craters. (b) Dried composite. (c) Sample from (b) after soaking in water 15 minutes.

Trapped air bubbles may be addressed in the future by degassing and rapid re-pressurization of the composites. Though this is a well-established technique for removing air in materials like epoxies, the potential for freezing and localized dehydration of the composites under vacuum is likely to result in increasingly heterogenous stones. Such vacuum equipment, though common in chemistry laboratories, may be inaccessible to urologists who would be preparing these phantoms. Swelling reduction can be accomplished by conversion of chitosan or by waterproofing of composites. Waterproofing by CrystalBond 509 was tested but led to increased ablation volumes and higher organic fraction in composite stones. Conversion of chitosan to chitin in hot acetic anhydride was also tested but this led to “crumbly” phantoms.

Other methods of waterproofing or swelling reduction may be worth pursuing in the absence of other promising COM phantoms. However, it is my opinion that polymer/mineral composites will always be inadequate if there is an overreliance on polymer-mineral bonding over mineral-

mineral bonding. Therefore, I would focus research into COM plasters or layered, nacre-like growth of COM rather than simple polymer/mineral mixtures.

5.2 Orientation effects in the Raman spectrum of calcium oxalates

As noted in Chapter 3, the differing crystallographic orientations of the oxalate molecules within COM lead to observable variation in relative Raman peak intensity. While Figure 3.2 shows maps with either the 1464 or 1490 cm^{-1} dominant, Figure 5.2 shows a map using Raman spectra from four orthogonal crystal orientations with respect to laser polarization. This includes spectra in which both peaks at 1464 and 1490 cm^{-1} are weaker than those near 500 and 900 cm^{-1}.

The peak at 1464 cm^{-1} originates from the oxalate lying in the (100) plane, while the peak at 1490 cm^{-1} originates form the oxalate lying in the (010) plane. Figure 5.3 and Figure 5.4 show that excitation of the stretching modes at 1464 and 1490 cm^{-1} are highly dependent on polarization alignment with oxalate molecules in the crystal structure of COM. Only polarization parallel to the length of the oxalate molecules results in excitation of the C-C and C-O symmetric modes results in intense peaks at 1464 and 1490 cm^{-1}, matching assignments from literature. Peaks near 900, 500, and 200 cm^{-1} also show variability with polarization. In contrast, the bending mode attributed to water at 1650 cm^{-1} shows little variation in intensity based on polarization. Orientations with low-intensity oxalate stretches at 1464 and 1490 cm^{-1} have apparently led to misidentification of COM as COD in literature (Sivaguru et al. 2021, Supplementary Figure 6) suggesting better understanding of orientation effects on the Raman spectrum of COM will be helpful for accurate application of Raman spectroscopy to kidney stone mapping. Future work should use additional crystal orientations and a polarizer between the sample and detector to gain additional information about the dependence of Raman spectra on crystal orientation. With sufficient information about the Raman tensor, it should be possible to determine COM crystal

orientation with high-quality Raman spectra which can be compared to crystal orientations determined by diffraction techniques.

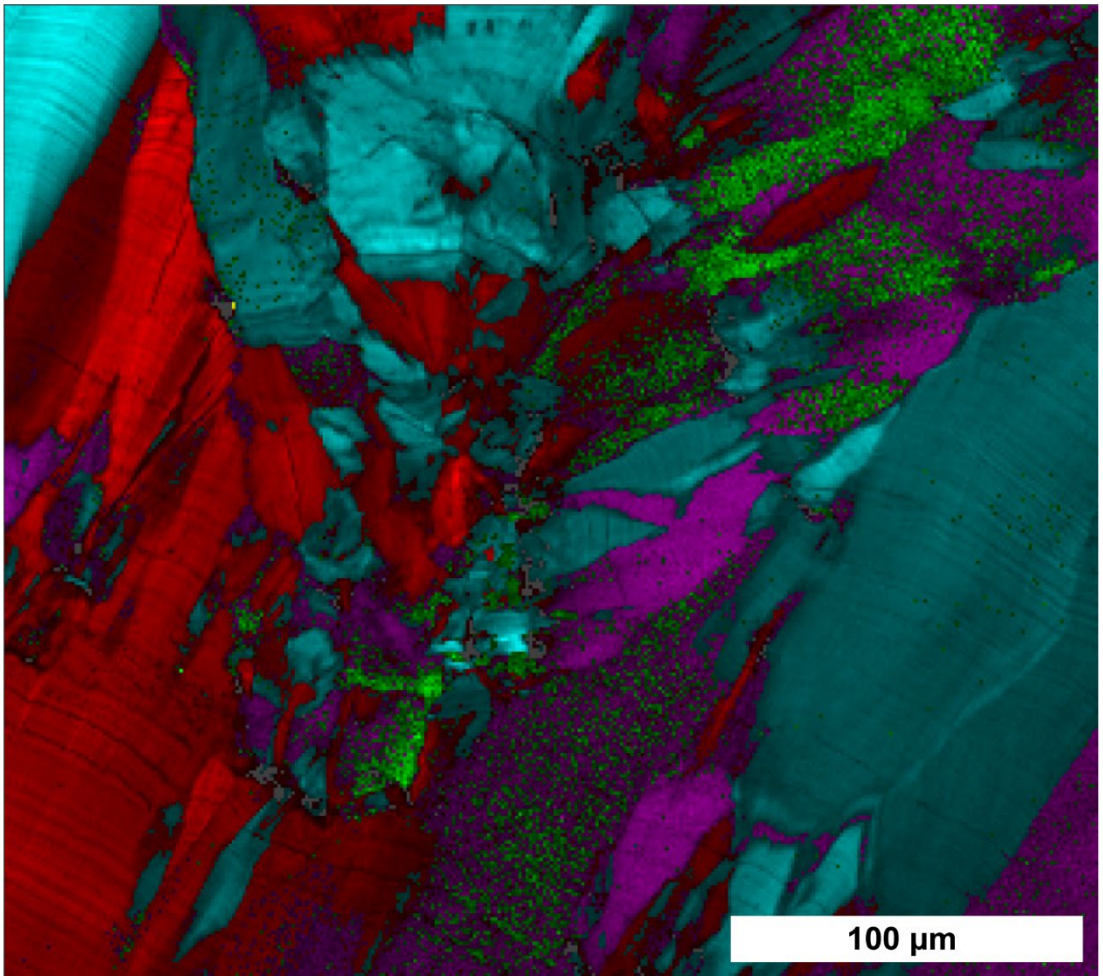

Figure 5.2: Remapped image of Figure 3.2b,d,f using additional COM orientations.

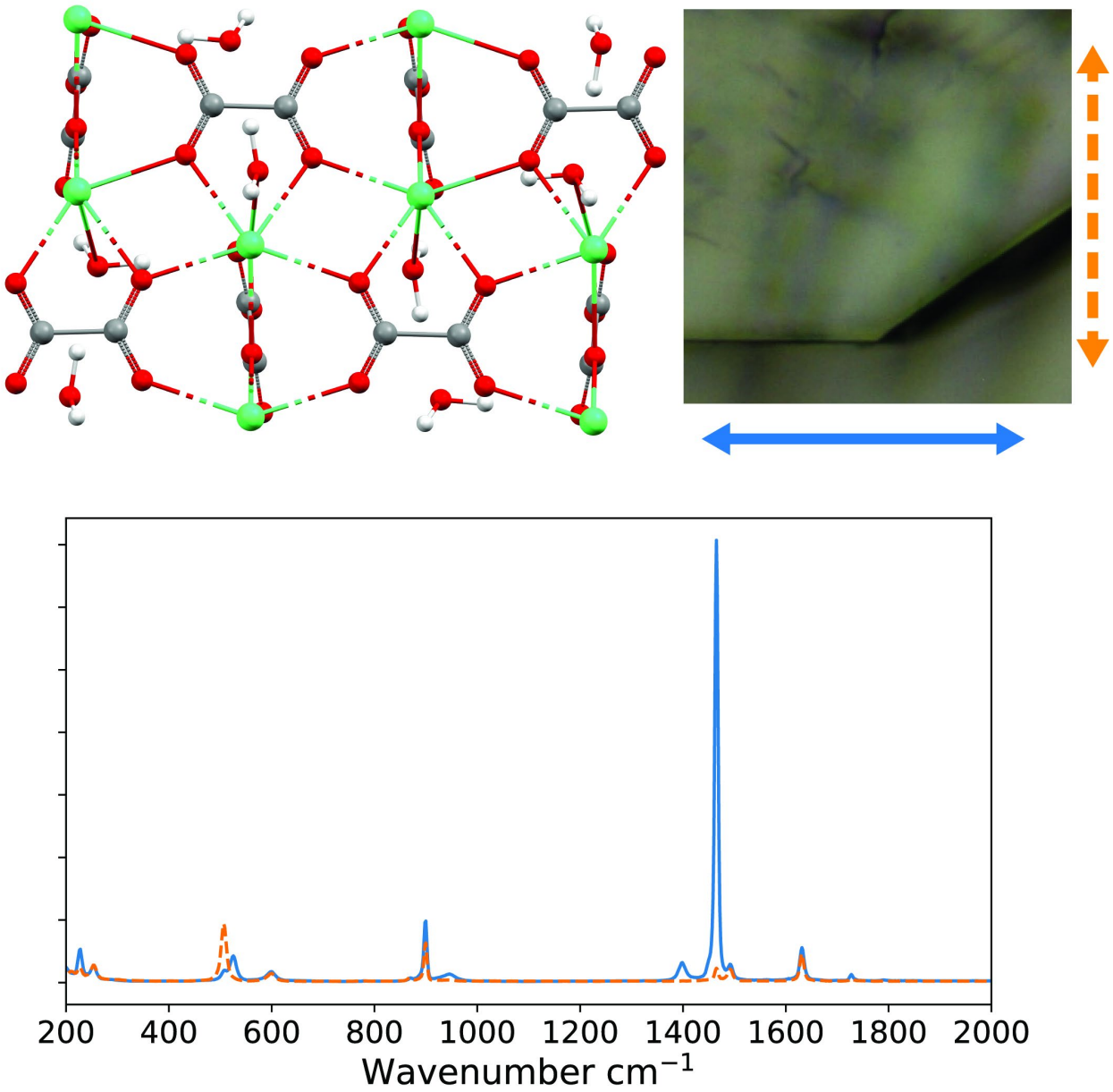

Figure 5.3: Raman spectra of calcium oxalate monohydrate perpendicular to the (100) plane with laser polarization oriented (blue) parallel to the [010] direction and (orange) perpendicular to the [010] direction.

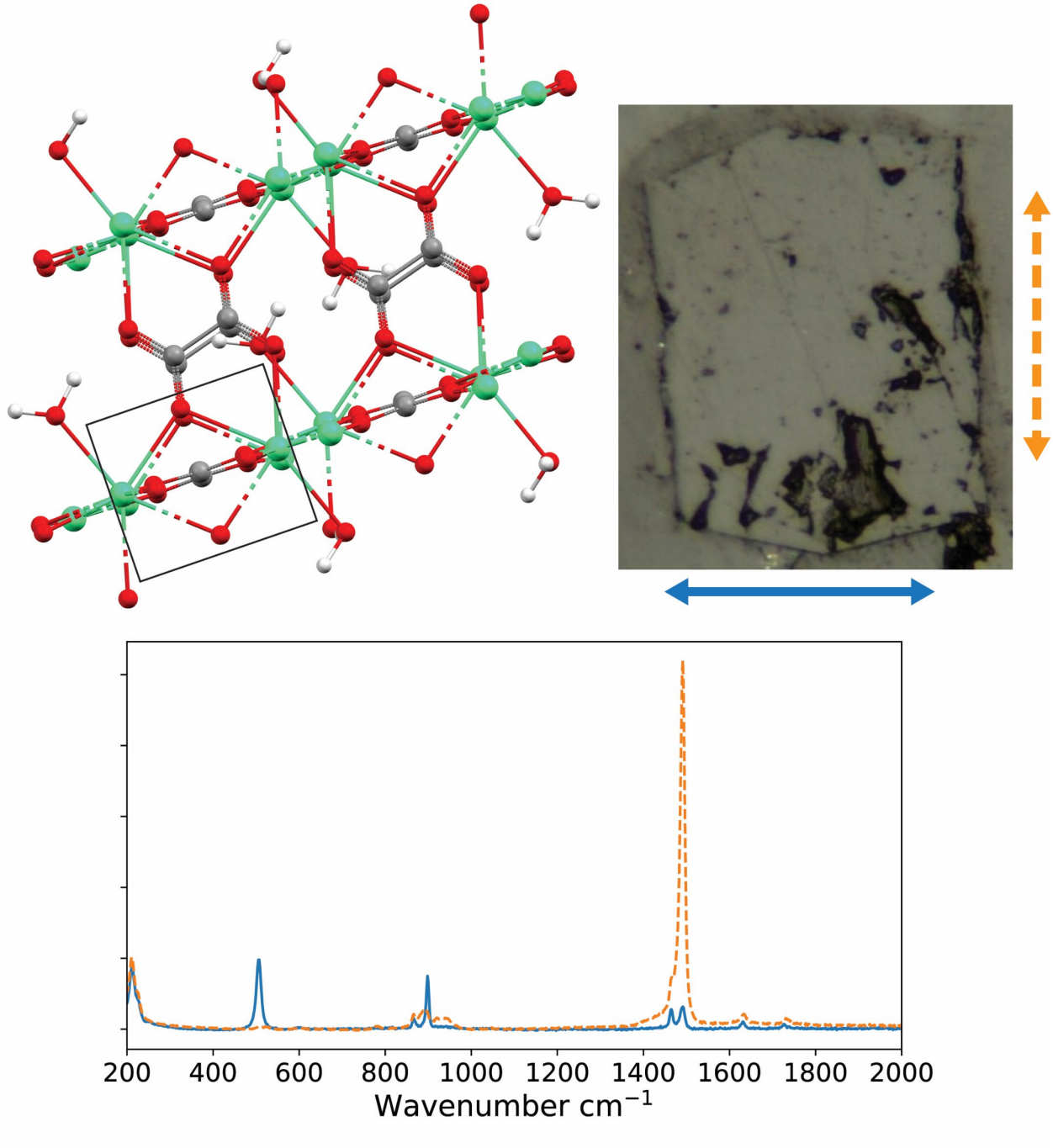

Figure 5.4: Raman spectra of calcium oxalate monohydrate perpendicular to the (010) plane with laser polarization oriented (blue) perpendicular to the [001] direction and (orange) parallel to the [001] direction.

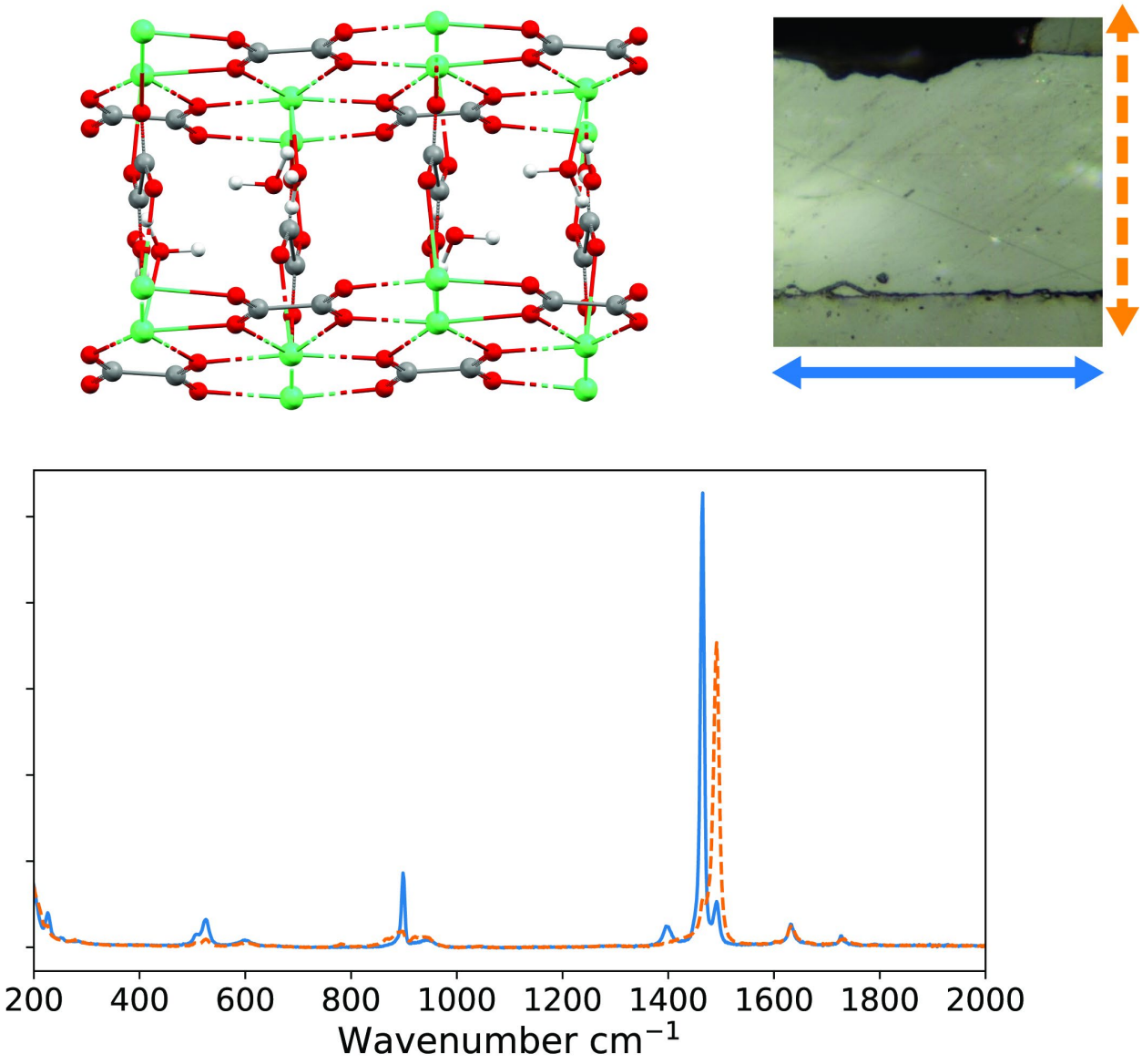

Figure 5.5: Raman spectra of calcium oxalate monohydrate perpendicular to the (001) plane with laser polarization oriented (blue) parallel to the [010] direction and (orange) perpendicular to the [010] direction

5.3 Growing kidney stones in vitro

As kidney stones cannot be studied in vivo, the ability to grow accurate kidney stone models has been a long-sought goal of scientists seeking to understand their nucleation and growth.[153–155] Phantoms grown artificially are likely to have advantages over plaster or composite based phantoms especially in terms of void space and direct mineral-mineral binding. Below, I describe

attempts at growing artificial COM stones with layered spherulitic growth like type 1a COM stones and make suggestions for future researchers attempting to growth their own stones.

COM and COD crystals with morphologies resembling those found in human stones are most easily grown in artificial urine[124] using flow cells. The artificial urine formula used for flow cell experiments is outlined in Table 5.1 with calcium chloride and sodium oxalate concentrations varied to promote growth or dissolution. For initial growth of COM and COD, two 500 mL artificial urine solutions with calcium oxalate precursors were prepared, one containing 10 mM sodium oxalate and the second containing 10 mM calcium chloride. Peristaltic pumps were used to move these solutions at a rate of 1 mL/minute each (2 mL/minute total) for 8 hours through custom-made flow cells (Figure 5.6). A mixture of COD and COM results with several morphologies present (**Error! Reference source not found.**). After initial nucleation, artificial urine with ≤1 mM $CaCl_2$ and $Na_2C_2O_4$ can be passed through the flow cell to dissolve COD leaving primarily COM. As saturation ratio is always higher for COM than COD, presence of COD prevents dissolution and may allow for slight growth of COM.

Table 5.1: Concentration of artificial urine components. Adapted from Sarigul et al.[124]

Compound	Formula	Concentration
Sodium sulfate	Na_2SO_4	11.965 mM
Sodium citrate	$Na_3C_6H_5O_7$	2.450 mM
Urea	CH_4N_2O	249.75 mM
Potassium chloride	KCl	30.953 mM
Sodium chloride	NaCl	30.053 mM
Magnesium sulfate	$MgSO_4$	4.389 mM
Ammonium chloride	NH_4Cl	23.667 mM
Sodium phosphate monobasic	NaH_2PO_4	18.667 mM
Sodium phospahte dibasic	Na_2HPO_4	4.667 mM
Calcium chloride	$CaCl_2$	0-10 mM
Sodium oxalate	$Na_2C_2O_4$	0-10 mM
Sodium alginate		0.02 % weight/volume

To achieve observable growth in COM spherulites after initial nucleation and COD dissolution, oxalate and calcium ion concentrations in artificial urine precursor solutions need to be raised to 5 mM each. Alternating between artificial urine solutions with 5 mM calcium and oxalate ions and artificial urine solutions without calcium or oxalate allows further growth of COM and COD and ultimately results in mixed COM/COD aggregates. Layering in COM spherulites can be seen in both optical and electron microscopy images suggesting this approach may be viable for producing larger stone-like aggregates though these remain too friable for use as phantoms.

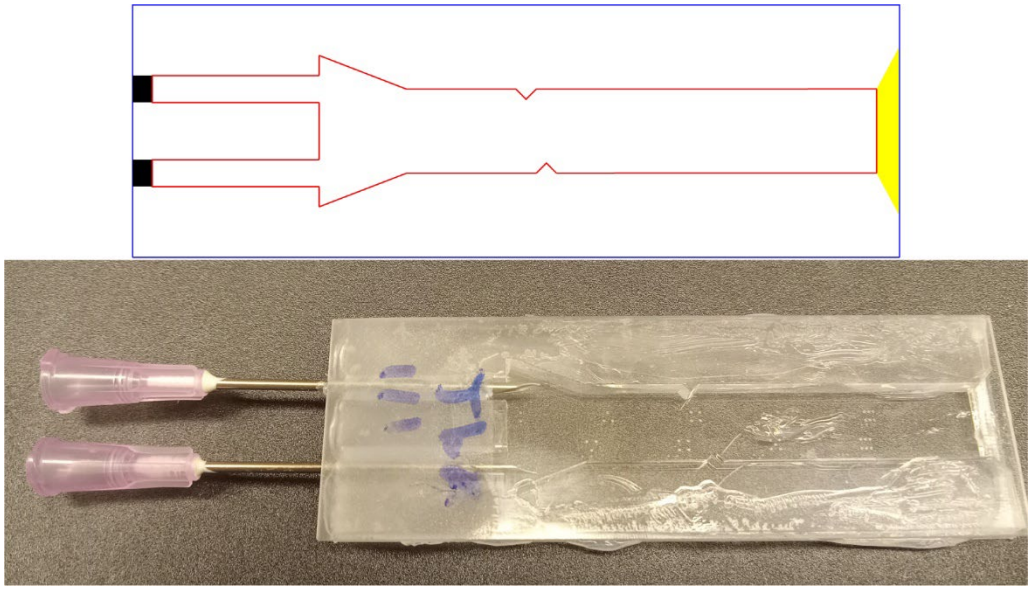

Figure 5.6: Schematic and image of flow cells used for artificial stone growth.

With existing flow cells, nucleation and growth takes place over most of the glass microscope slides used to seal the top and bottom of the flow cell. To form an artificial stone, it would be ideal to have nucleation occur at a localized point to allow layered spherulitic growth on millimeter scales. This may be accomplished via nucleation promoters coupled with precursor solutions with lower calcium and oxalate concentrations. Drilling a small air hole in the slides or acrylic used to construct the flow cell may also be viable as evaporation will lead to higher supersaturation locally. Reintroducing and updating the methods of Vermeulen et al.[153–155] who

grew stone-like concretions on wire loops at the end of stirring rods also deserves investigation.

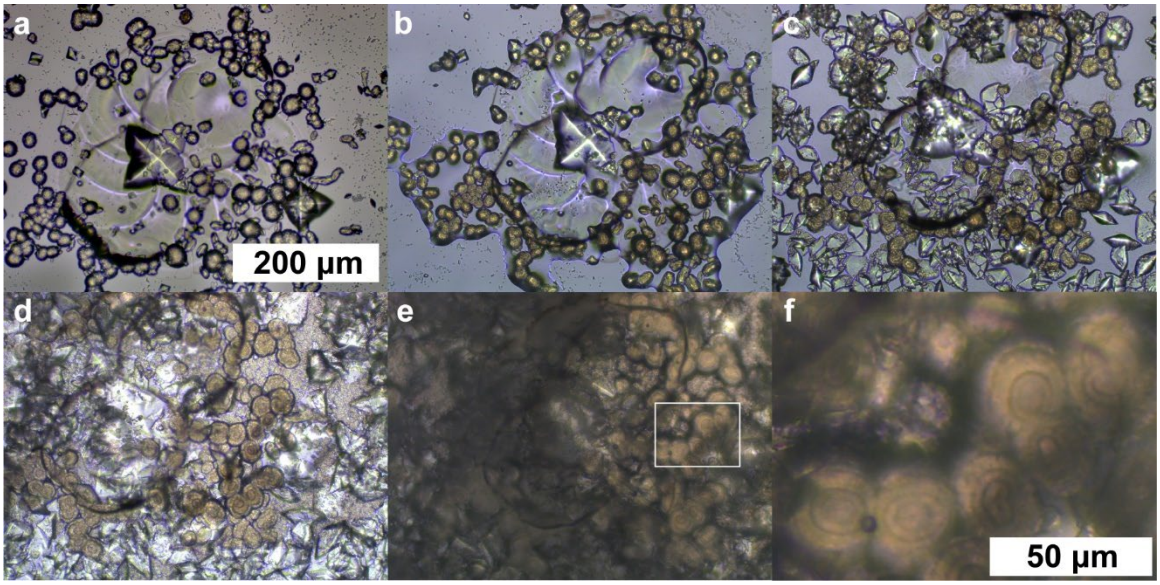

Figure 5.7: Growth of a mixed COM/COD artificial stone.

The effect of increased flow rates on nucleation and growth should be studied to understand whether higher growth rates can be achieved for COD/COM stones. As brushite and struvite stones are believed to grow faster than calcium oxalate stones on average, artificial stones from these minerals may be better targets for flow cell growth. Ultimately, any research into artificial stone growth should be conducted with long time scales in mind as takes weeks or months perform many of the experiments that will ultimately lead to artificial stones.

5.4 Modeling kidney stone fragmentation

Developing computational models of kidney stone ablation would be advantageous for studying the effect of laser lettings on stone destruction, particularly controlling dusting vs. fracture of stones. Figure 5.9 summarizes the properties of kidney stones that impact ablation that will need to be measured to develop an accurate numerical model of ablation. Thermal properties and radiative transfer are discussed with relation to computational modeling below.

5.4.1 Radiative transfer

Radiative transfer modeling will likely take two steps: the first for radiative transfer in urine from the optical fiber to the stone surface with bubble formation and the second for radiative transfer in stones. Modeling radiative transfer from fiber tip to stone surface can be accomplished using high-speed imagery and optical modeling software (e.g. Zemax). This method was tested using Ho:YAG lasers firing 1 J pulses (Figure 5.8) which demonstrated minor beam diffraction at the vapor/water interface. Experiments will need to be repeated for each pulse setting of interest. Backlighting of vapor bubbles is the ideal orientation for high-speed camera imagery as total reflection at the water/vapor interface leads to a sharp contrast at the leading edges of the vapor bubble allowing easy tracing of its outline.

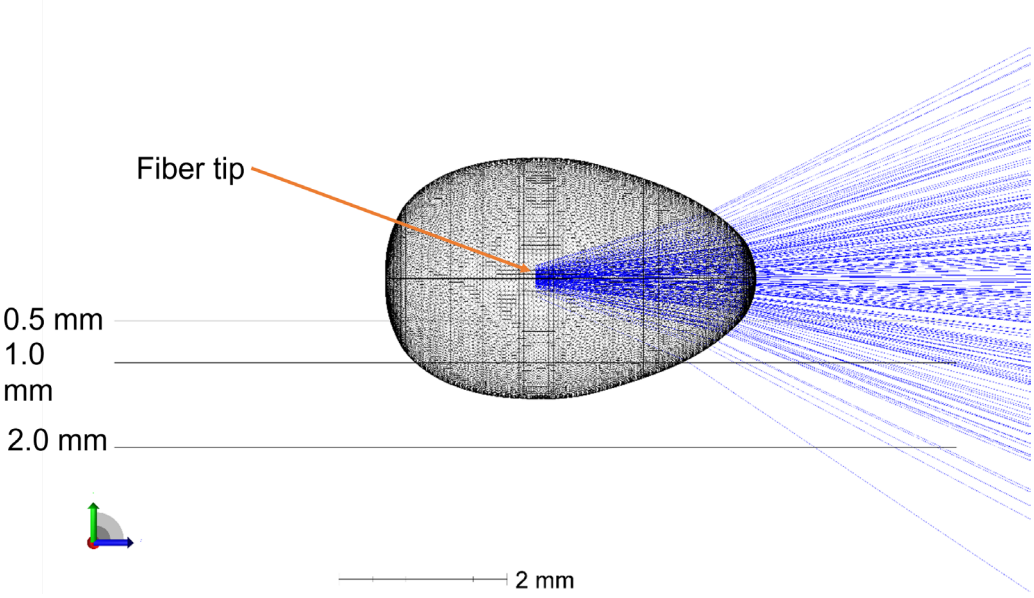

Figure 5.8: Optical modeling of a vapor bubble generated by a 1 J short pulse from a Ho:YAG laser.

As scattering is complex in kidney stones, a parameterized model will likely be preferable to the ray-tracing models that can be used in urine. Ideally, the multiphysics simulation tool used for thermal and mechanical modeling would be able to solve radiative transfer equations. In lieu of simulation within multiphysics software, various radiative transfer models for snow/atmospheric

problems could potentially be adapted for use in kidney stone models (i.e. DISORT[156] or TARTES[157]). A range of scattering properties will need to be tested for kidney stones due to their natural structural variability. With absorption coefficients now measured, scattering parameters can be measured using thin-sectioned stone samples. Thin sections of human stones, ≈100 µm thick, should be prepared in an embedding medium with little NIR absorption and polished on both sides. An IR microscope or FTIR spectrometer can then be used to measure total extinction coefficient from which scattering coefficients can be derived.

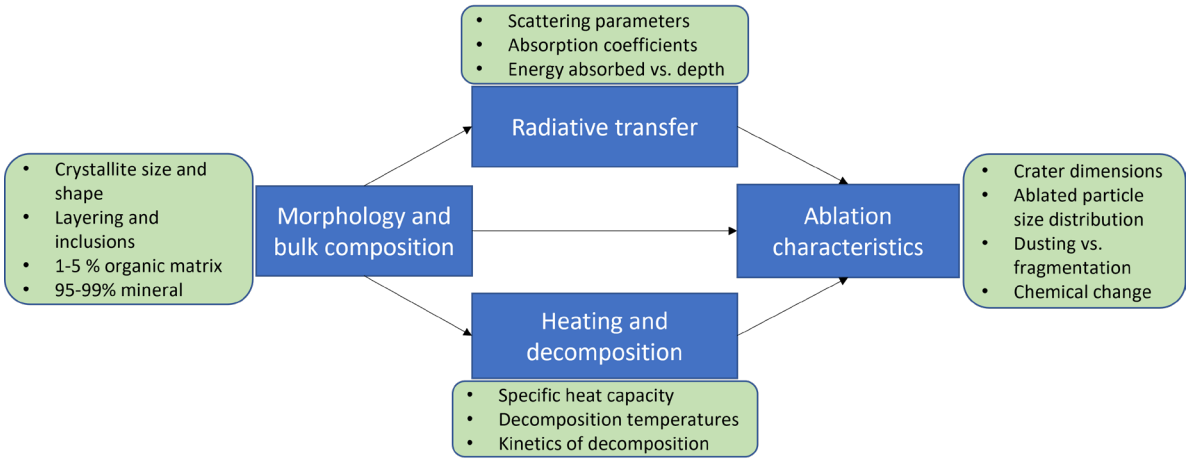

Figure 5.9: Overview of parameters impacting ablation.

5.4.2 Thermal properties

Table 5.1 below contains (incomplete) information and references to data needed for thermal modeling of kidney stones. This includes heat expansion coefficients, room-temperature specific heat capacities, and activation energies for thermal decomposition. For all minerals, heat capacities need to be measured from 37 °C to the thermal decomposition temperature (excluding hydroxyapatite as it degrades at >1000 °C). Degradation has been studied via thermogravimetric analysis for many minerals with activation energy and enthalpy of decomposition measured in some cases. Activation energy can be used for modeling of degradation kinetics though it is uncertain whether the decomposition mechanism of minerals measured via TGA with heating rates

on the order of 0.01-1 K/s will be the same as decomposition when heating rates are closer to 10^5-10^6 K/s under laser ablation.

Table 5.2: Table of available thermal data for kidney stone minerals.

Mineral	Specific heat capacity (J g^{-1} K^{-1})	Activation energy (kJ mol^{-1})	Enthalpy of dehydration	Decomposition temperature (°C)
Calcium oxalate monohydrate	1.04 (at 300 K)[158]	81[159]	66.5[160]	130-220°C[160]
Calcium oxalate dihydrate	-	-	83.6	≈125-210 °C[160]
Hydroxyapatite	1.488 (at 300 K)[161]	-	-	-
Uric acid	0.99 (at 297 K)[162]	-	-	>300 °C[163]
Brushite	-	-	-	≈111 °C[164]
Struvite	-	-	-	≈85 °C*

* For water loss at higher heating rates. Ammonia loss may occurs at ≈40 °C at lower heating rates.[165]

5.4.3 Computational modeling of mechanical destruction

With thermal and radiative transfer properties measured, stone destruction becomes primarily a mechanical engineering problem. Mechanical strength of kidney stones will need to be measured and, based on observations during lithotripsy, will likely be variable throughout different stone layers. Commercial finite element analysis software from companies like Ansys or COMSOL are capable of modeling mechanical fracture and failure of concrete and may be adaptable for use with kidney stones in partnership with mechanical engineers who study such phenomena.

Appendix: Additional Raman Images

Below are additional Raman chemical images of kidney stone samples. For COM-containing stones, three spectra were used for least-squares fitting to account for different COM orientations. The three COM spectra are shown in Figure A.1. Spatial resolution is noted for each Figure. All images were collected using a 532 nm laser unless otherwise noted.

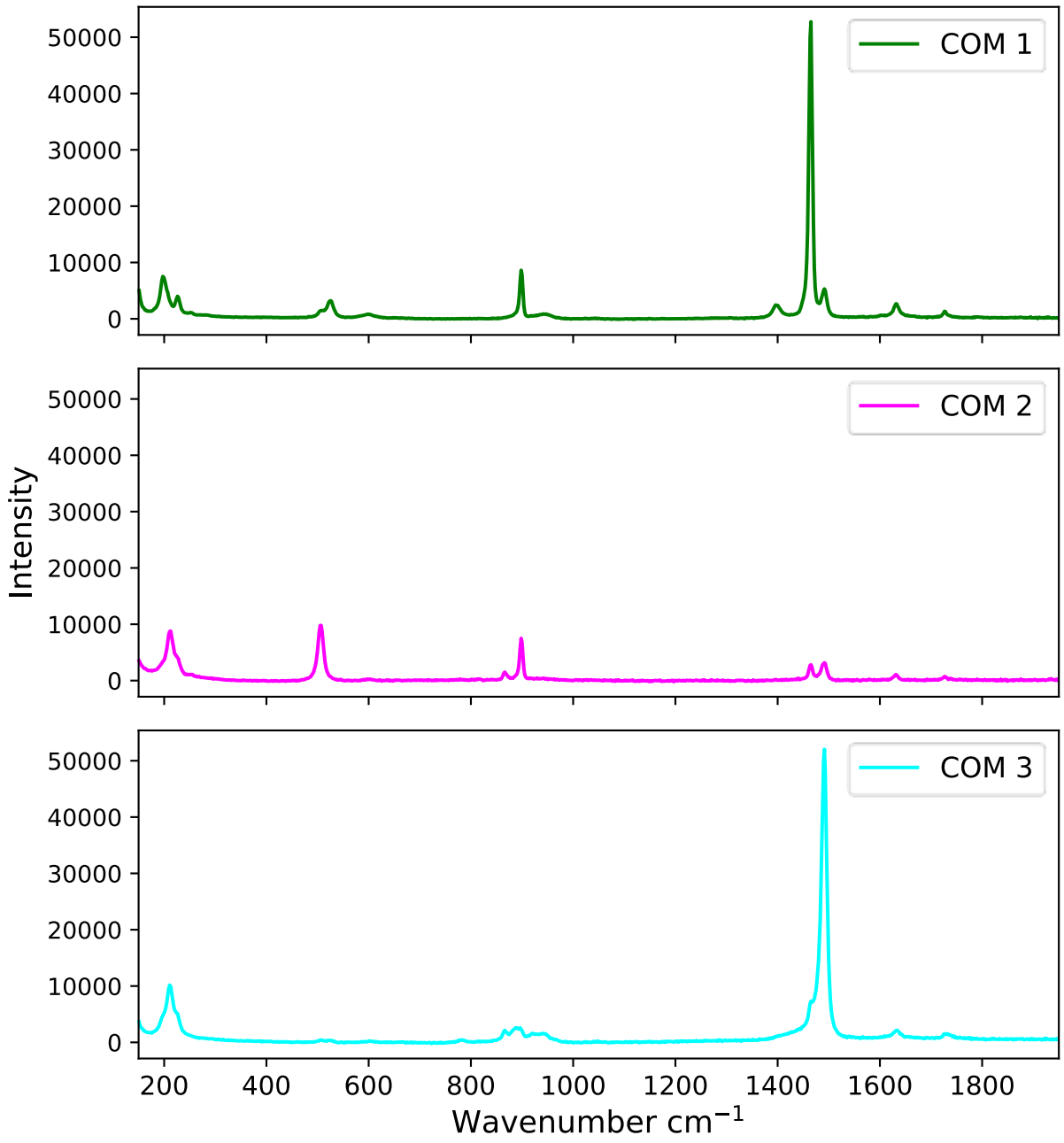

Figure A.1: Raman spectra of COM used for least-squares fitting in Raman maps below. COM 1 was taken normal to the (001) plane with polarization oriented parallel to the [010] axis. COM 2 and COM 3 were taken along the [010] axis parallel and perpendicular to the [001] direction, respectively.

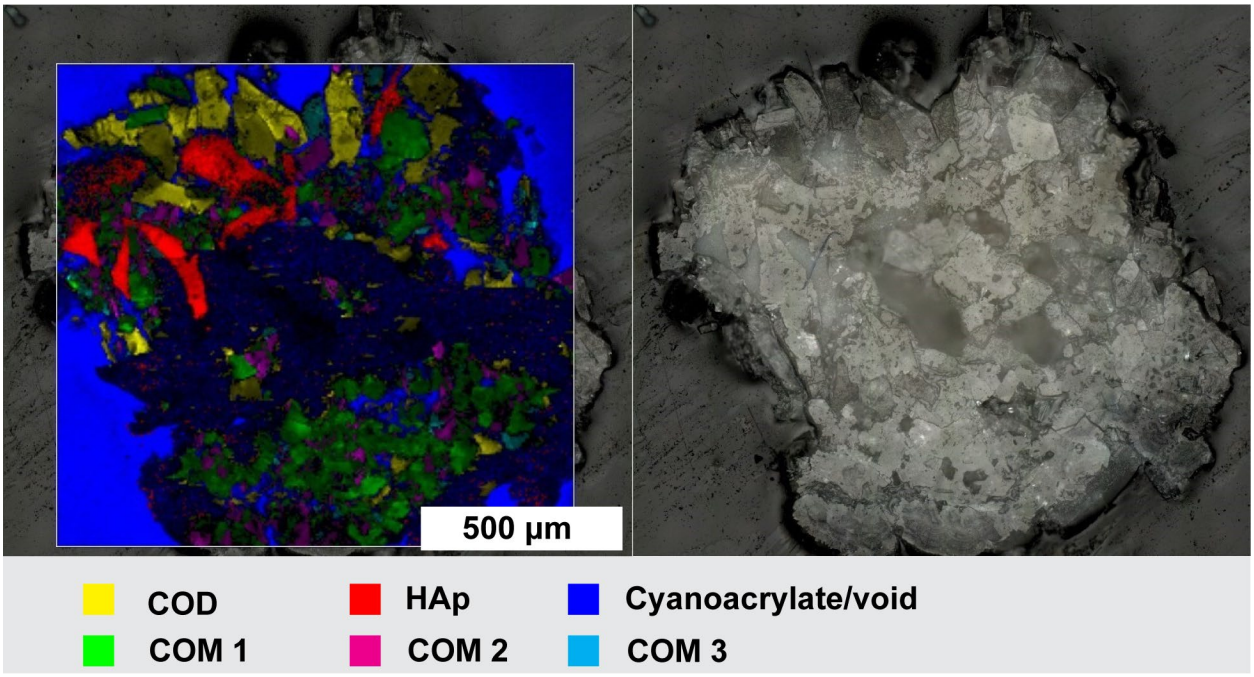

Figure A.2: Additional fragment originating from the mixed calcium oxalate and calcium phosphate stone imaged in Figures 3.9 and 3.11.

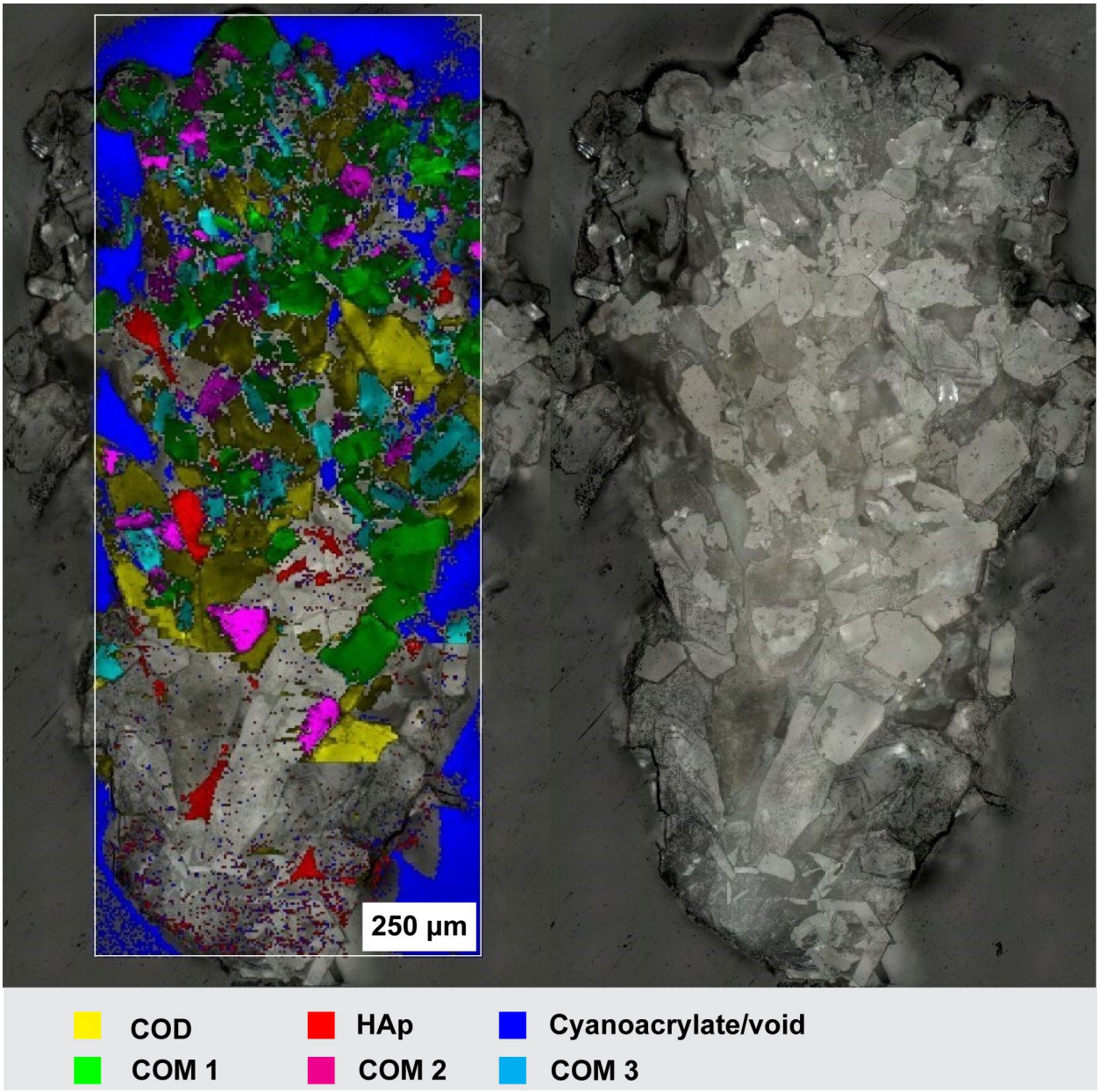

Figure A.3: Additional fragment originating from the mixed calcium oxalate and calcium phosphate stone imaged in Figures 3.9 and 3.11.

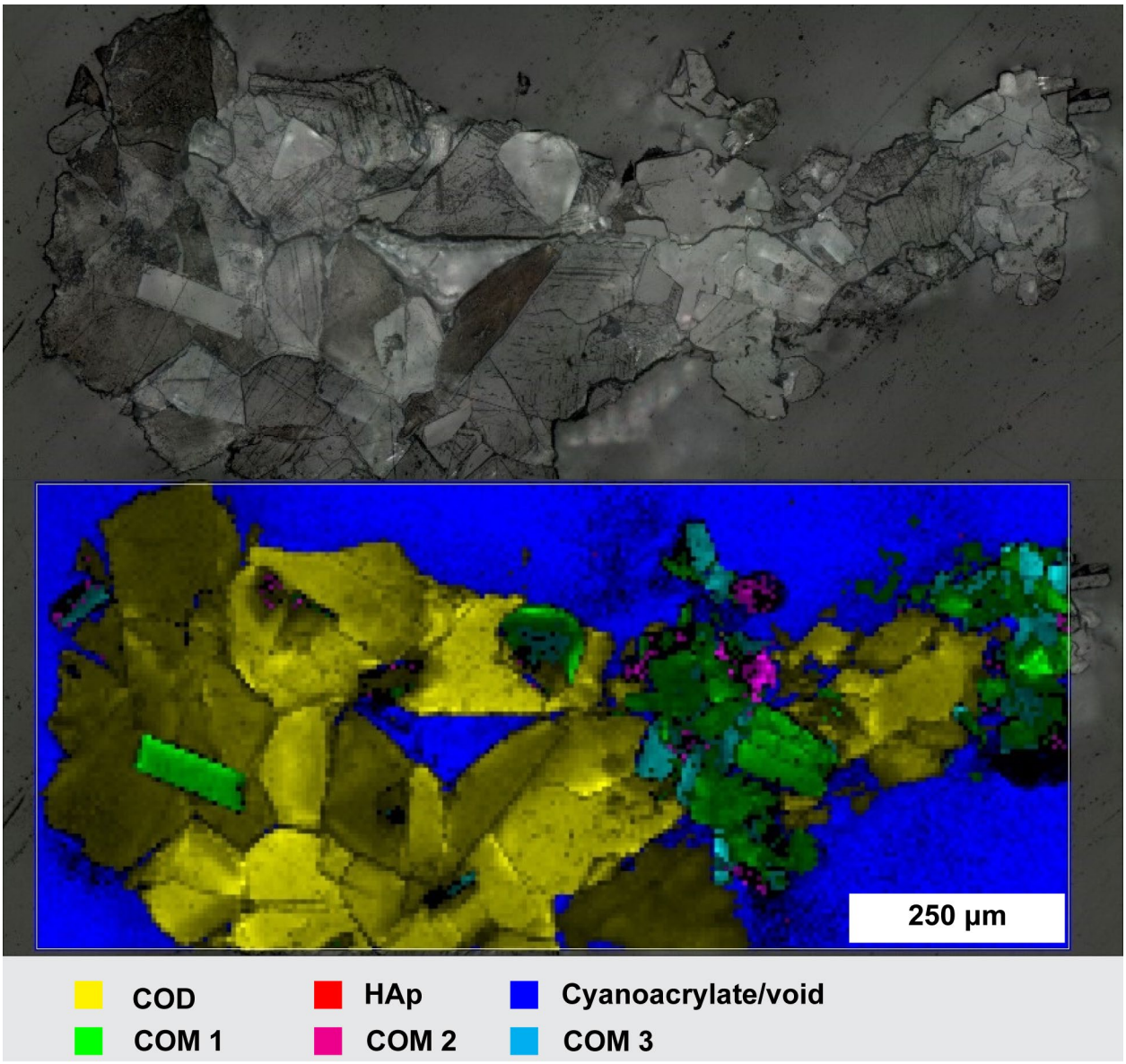

Figure A.4: Additional fragment originating from the mixed calcium oxalate and calcium phosphate stone imaged in Figures 3.9 and 3.11.

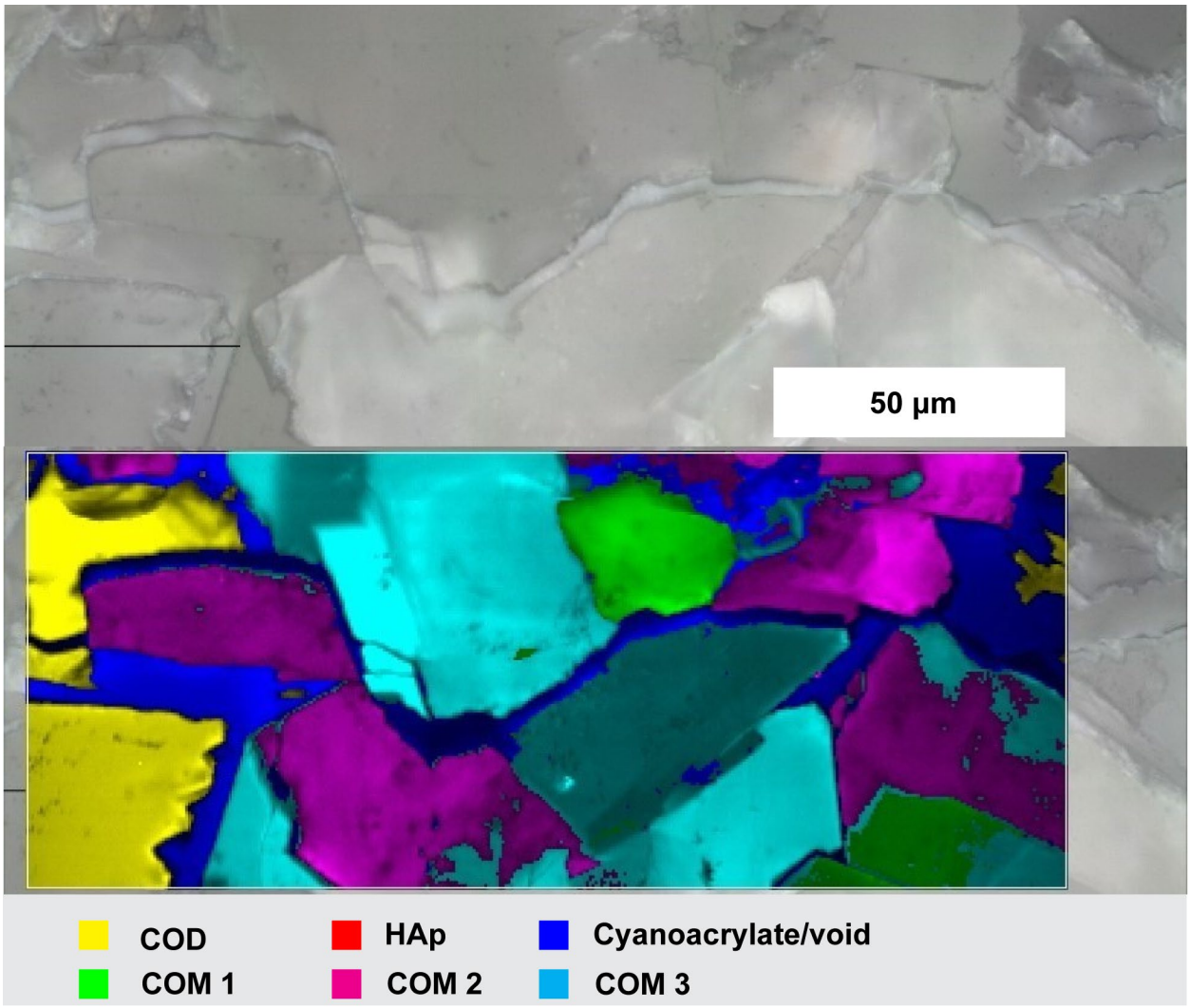

Figure A.5 High (0.5 µm) spatial resolution map of fragment originating from the mixed calcium oxalate and calcium phosphate stone imaged in Figures 3.9 and 3.11.

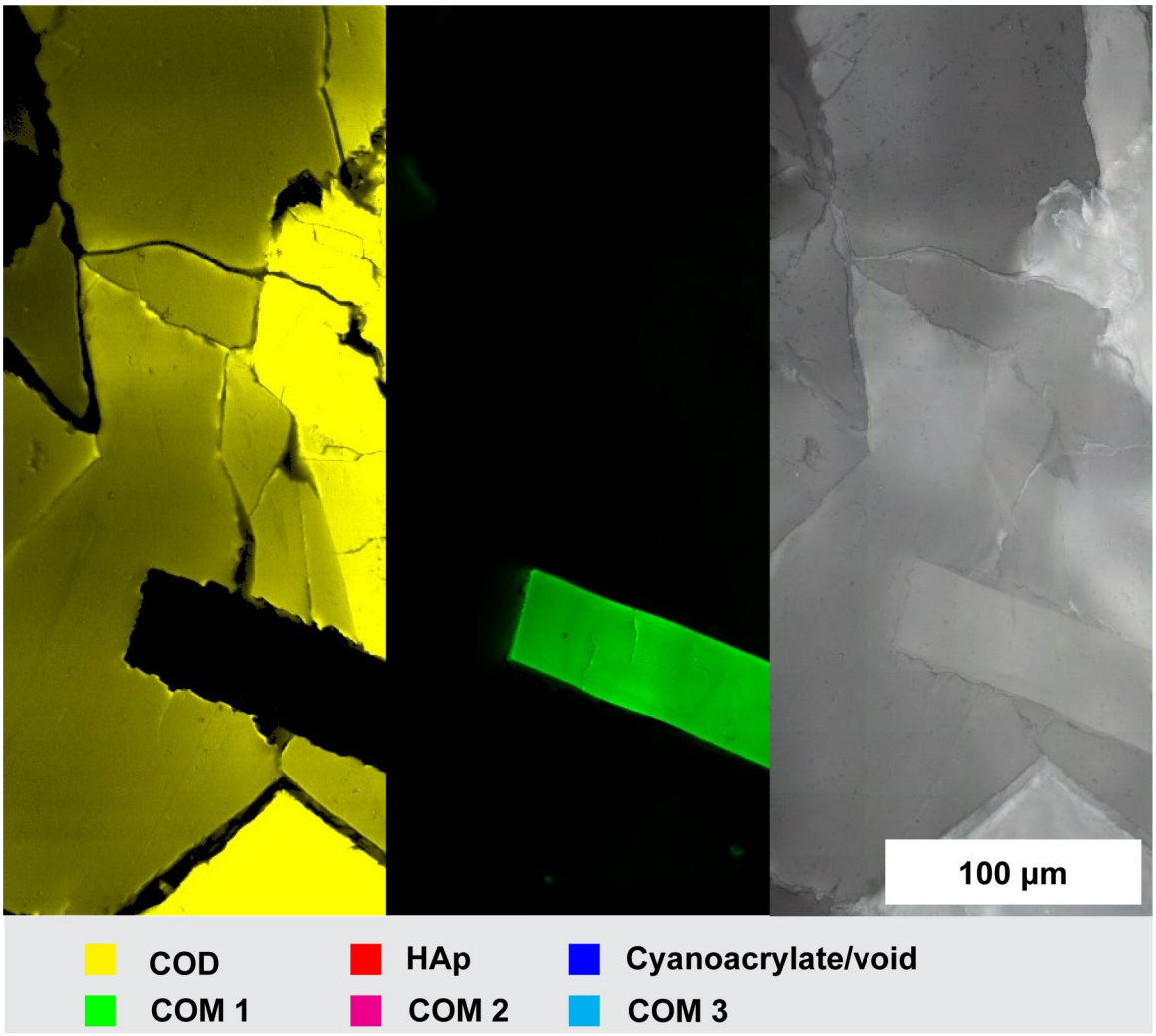

Figure A.6: High (0.5 µm) spatial resolution Raman map of calcium oxalate/phosphate fragment shown in Figure A.4.

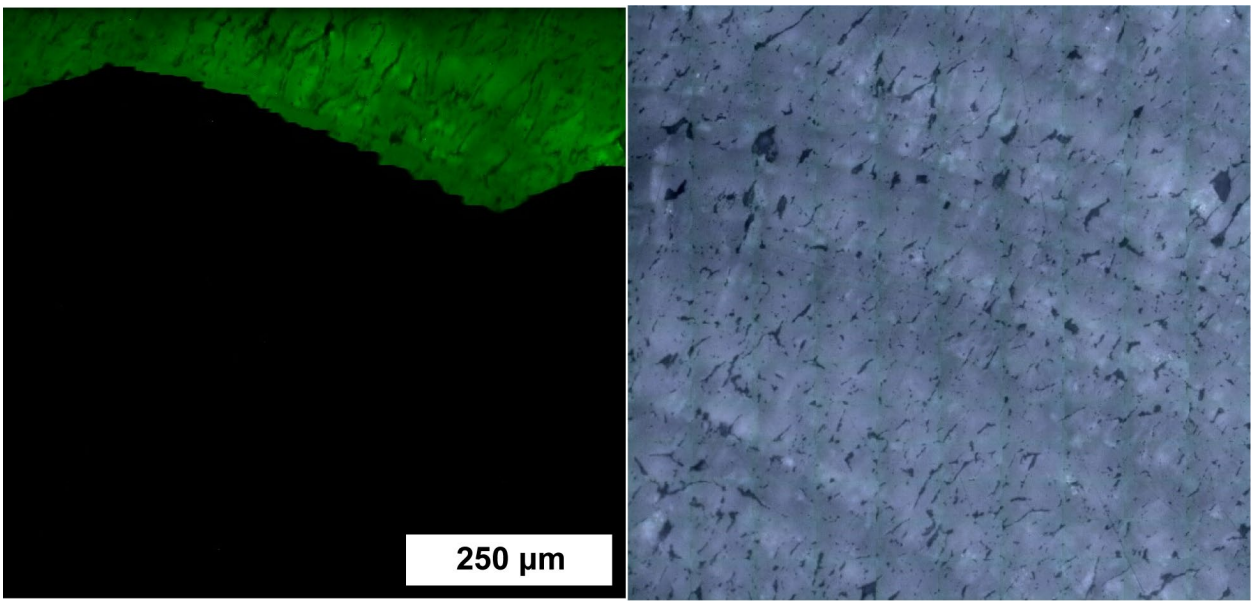

Figure A.7: Map of struvite stone using a violet (405 nm) laser. Green indicates struvite, while black regions indicate laser damage and burning. The laser is scanned from left to right. In many samples, once damage occurs along a raster line it continues as burned, darkened surfaces absorb more light making damage easier to cause. However, for this struvite sample, damage seems to follow the contours of layering in the stone. This could indicate higher presence of organic matter in the burned areas. This would be a case where observation via fluorescence microscopy prior to Raman mapping may benefit Raman users as regions with higher organic matter could be avoided or scanned with lower laser power.

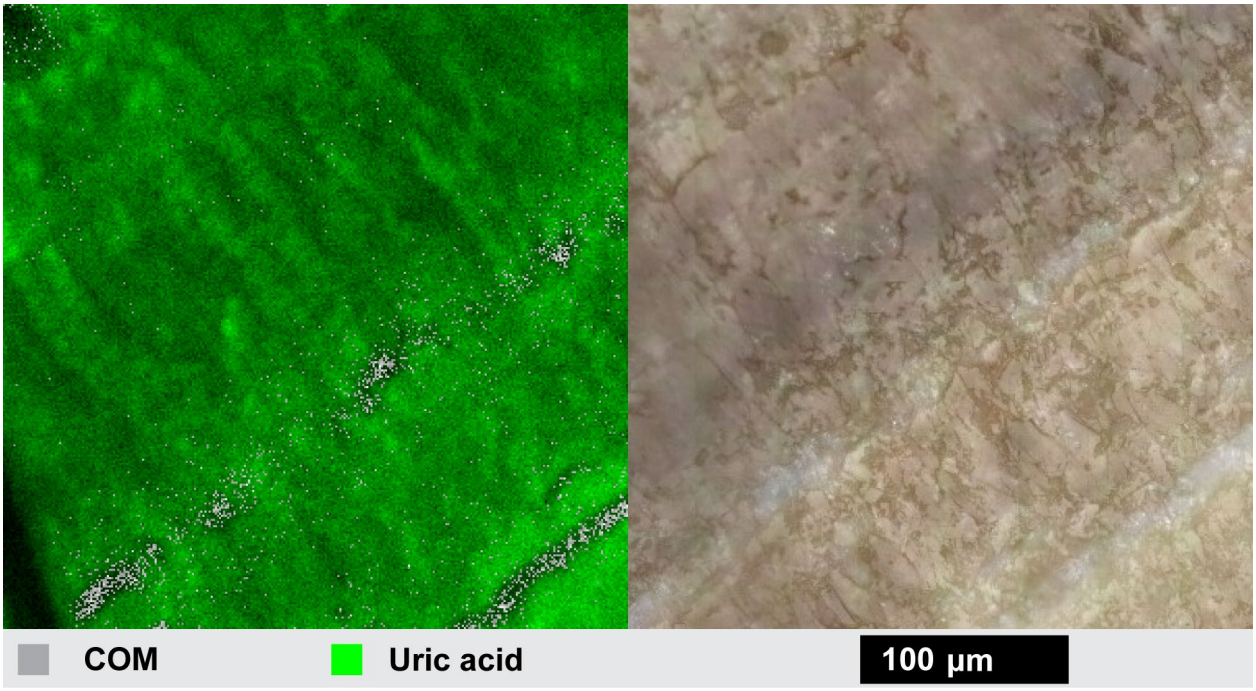

Figure A.8: Example of uric acid stone mapped using a 405 nm laser.

References

(1) Daudon, M.; Bazin, D.; André, G.; Jungers, P.; Cousson, A.; Chevallier, P.; Véron, E.; Matzen, G. Examination of Whewellite Kidney Stones by Scanning Electron Microscopy and Powder Neutron Diffraction Techniques. *J Appl Crystallogr* **2009**, *42* (1), 109–115. https://doi.org/10.1107/S0021889808041277.

(2) Simmons, W. N.; Cocks, F. H.; Zhong, P.; Preminger, G. A Composite Kidney Stone Phantom with Mechanical Properties Controllable over the Range of Human Kidney Stones. *Journal of the Mechanical Behavior of Biomedical Materials* **2010**, *3* (1), 130–133. https://doi.org/10.1016/j.jmbbm.2009.08.004.

(3) Heimbach, D.; Munver, R.; Zhong, P.; Jacobs, J.; Preminger, G. M. ACOUSTIC AND MECHANICAL PROPERTIES OF ARTIFICIAL STONES IN COMPARISON TO NATURAL KIDNEY STONES. 8.

(4) Thongprayoon, C.; Krambeck, A. E.; Rule, A. D. Determining the True Burden of Kidney Stone Disease. *Nat Rev Nephrol* **2020**, *16* (12), 736–746. https://doi.org/10.1038/s41581-020-0320-7.

(5) Singh, P.; Harris, P. C.; Sas, D. J.; Lieske, J. C. The Genetics of Kidney Stone Disease and Nephrocalcinosis. *Nat Rev Nephrol* **2022**, *18* (4), 224–240. https://doi.org/10.1038/s41581-021-00513-4.

(6) Jeong, I. G.; Kang, T.; Bang, J. K.; Park, J.; Kim, W.; Hwang, S. S.; Kim, H. K.; Park, H. K. Association Between Metabolic Syndrome and the Presence of Kidney Stones in a Screened Population. *American Journal of Kidney Diseases* **2011**, *58* (3), 383–388. https://doi.org/10.1053/j.ajkd.2011.03.021.

(7) Brikowski, T. H.; Lotan, Y.; Pearle, M. S. Climate-Related Increase in the Prevalence of Urolithiasis in the United States. *Proceedings of the National Academy of Sciences* **2008**, *105* (28), 9841–9846. https://doi.org/10.1073/pnas.0709652105.

(8) Castiglione, V.; Sacré, P.-Y.; Cavalier, E.; Hubert, P.; Gadisseur, R.; Ziemons, E. Raman Chemical Imaging, a New Tool in Kidney Stone Structure Analysis: Case-Study and Comparison to Fourier Transform Infrared Spectroscopy. *PLOS ONE* **2018**, *13* (8), e0201460. https://doi.org/10.1371/journal.pone.0201460.

(9) Streit, J.; Tran-Ho, L.-C.; Königsberger, E. Solubility of the Three Calcium Oxalate Hydrates in Sodium Chloride Solutionsand Urine-Like Liquors. *Monatshefte fuer Chemie* **1998**, *129* (12), 1225–1236. https://doi.org/10.1007/PL00010134.

(10) Sivaguru, M.; Saw, J. J.; Wilson, E. M.; Lieske, J. C.; Krambeck, A. E.; Williams, J. C.; Romero, M. F.; Fouke, K. W.; Curtis, M. W.; Kear-Scott, J. L.; Chia, N.; Fouke, B. W. Human Kidney Stones: A Natural Record of Universal Biomineralization. *Nat Rev Urol* **2021**, *18* (7), 404–432. https://doi.org/10.1038/s41585-021-00469-x.

(11) Corrales, M.; Doizi, S.; Barghouthy, Y.; Traxer, O.; Daudon, M. Classification of Stones According to Michel Daudon: A Narrative Review. *European Urology Focus* **2021**, *7* (1), 13–21. https://doi.org/10.1016/j.euf.2020.11.004.

(12) Al-Atar, U.; Bokov, A. A.; Marshall, D.; Teichman, J. M. H.; Gates, B. D.; Ye, Z.-G.; Branda, N. R. Mechanism of Calcium Oxalate Monohydrate Kidney Stones Formation: Layered Spherulitic Growth. *Chem. Mater.* **2010**, *22* (4), 1318–1329. https://doi.org/10.1021/cm901751g.
(13) Sivaguru, M.; Saw, J. J.; Williams, J. C.; Lieske, J. C.; Krambeck, A. E.; Romero, M. F.; Chia, N.; Schwaderer, A. L.; Alcalde, R. E.; Bruce, W. J.; Wildman, D. E.; Fried, G. A.; Werth, C. J.; Reeder, R. J.; Yau, P. M.; Sanford, R. A.; Fouke, B. W. Geobiology Reveals How Human Kidney Stones Dissolve in Vivo. *Sci Rep* **2018**, *8* (1), 13731. https://doi.org/10.1038/s41598-018-31890-9.
(14) Daudon, M.; Réveillaud, R. J.; Levasseur, H.; Jungers, P. Combined Influence of Urinary Calcium and Oxalate Concentrations on Crystal Formation in Stone Formers. In *Urolithiasis*; Walker, V. R., Sutton, R. A. L., Cameron, E. C. B., Pak, C. Y. C., Robertson, W. G., Eds.; Springer US: Boston, MA, 1989; pp 155–157. https://doi.org/10.1007/978-1-4899-0873-5_43.
(15) Sivaguru, M.; Lieske, J. C.; Krambeck, A. E.; Fouke, B. W. GeoBioMed Sheds New Light on Human Kidney Stone Crystallization and Dissolution. *Nat Rev Urol* **2020**, *17* (1), 1–2. https://doi.org/10.1038/s41585-019-0256-5.
(16) Wang, L.; Nancollas, G. H. Calcium Orthophosphates: Crystallization and Dissolution. *Chem. Rev.* **2008**, *108* (11), 4628–4669. https://doi.org/10.1021/cr0782574.
(17) Brown, P. W. Phase Relationships in the Ternary System CaO─P2O5─H2O at 25°C. *Journal of the American Ceramic Society* **1992**, *75* (1), 17–22. https://doi.org/10.1111/j.1151-2916.1992.tb05435.x.
(18) Williams, J. C.; Lingeman, J. E.; Coe, F. L.; Worcester, E. M.; Evan, A. P. Micro-CT Imaging of Randall's Plaques. *Urolithiasis* **2015**, *43* (1), 13–17. https://doi.org/10.1007/s00240-014-0702-z.
(19) Williams, J. C.; Worcester, E.; Lingeman, J. E. What Can the Microstructure of Stones Tell Us? *Urolithiasis* **2017**, *45* (1), 19–25. https://doi.org/10.1007/s00240-016-0944-z.
(20) Martin, R. I.; Brown, P. W. Phase Equilibria Among Acid Calcium Phosphates. *Journal of the American Ceramic Society* **1997**, *80* (5), 1263–1266. https://doi.org/10.1111/j.1151-2916.1997.tb02973.x.
(21) Rumble, J. R. *CRC Handbook of Chemistry and Physics, 101st Edition (Internet Version 2020)*, 101st ed.; CRC Press/Taylor & Francis.
(22) Wang, L.; H. Nancollas, G. Pathways to Biomineralization and Biodemineralization of Calcium Phosphates: The Thermodynamic and Kinetic Controls. *Dalton Transactions* **2009**, *0* (15), 2665–2672. https://doi.org/10.1039/B815887H.
(23) Daudon, M.; Bouzidi, H.; Bazin, D. Composition and Morphology of Phosphate Stones and Their Relation with Etiology. *Urol Res* **2010**, *38* (6), 459–467. https://doi.org/10.1007/s00240-010-0320-3.
(24) Krambeck, A. E.; Handa, S. E.; Evan, A. P.; Lingeman, J. E. Profile of the Brushite Stone Former. *Journal of Urology* **2010**, *184* (4), 1367–1371. https://doi.org/10.1016/j.juro.2010.05.094.
(25) Cloutier, J.; Villa, L.; Traxer, O.; Daudon, M. Kidney Stone Analysis: "Give Me Your Stone, I Will Tell You Who You Are!" *World J Urol* **2015**, *33* (2), 157–169. https://doi.org/10.1007/s00345-014-1444-9.
(26) Ames, B. N.; Cathcart, R.; Schwiers, E.; Hochstein, P. Uric Acid Provides an Antioxidant Defense in Humans against Oxidant- and Radical-Caused Aging and Cancer: A

Hypothesis. *Proceedings of the National Academy of Sciences* **1981**, *78* (11), 6858–6862. https://doi.org/10.1073/pnas.78.11.6858.
(27) Simic, M. G.; Jovanovic, S. V. Antioxidation Mechanisms of Uric Acid. *J. Am. Chem. Soc.* **1989**, *111* (15), 5778–5782. https://doi.org/10.1021/ja00197a042.
(28) Wang, Z.; Königsberger, E. Solubility Equilibria in the Uric Acid–Sodium Urate–Water System. *Thermochimica Acta* **1998**, *310* (1), 237–242. https://doi.org/10.1016/S0040-6031(97)00230-X.
(29) Wang, Z.; Königsberger, L.; Königsberger, E. Solubility Equilibria in the Uric Acid–Ammonium Urate–Water System. *Monatsh Chem* **2018**, *149* (2), 327–332. https://doi.org/10.1007/s00706-017-2107-5.
(30) Pak, C. Y. C.; Sakhaee, K.; Fuller, C. Successful Management of Uric Acid Nephrolithiasis with Potassium Citrate. *Kidney International* **1986**, *30* (3), 422–428. https://doi.org/10.1038/ki.1986.201.
(31) Presores, J. B.; Swift, J. A. Solution-Mediated Phase Transformation of Uric Acid Dihydrate. *CrystEngComm* **2014**, *16* (31), 7278–7284. https://doi.org/10.1039/C4CE00574K.
(32) Prywer, J.; Sadowski, R. R.; Torzewska, A. Aggregation of Struvite, Carbonate Apatite, and Proteus Mirabilis as a Key Factor of Infectious Urinary Stone Formation. *Crystal Growth & Design* **2015**, *15* (3), 1446–1451. https://doi.org/10.1021/cg5018032.
(33) Qin, L.; Putnis, C. V.; Wang, L. Facet-Specific Dissolution–Precipitation at Struvite–Water Interfaces. *Crystal Growth & Design* **2021**. https://doi.org/10.1021/acs.cgd.1c00400.
(34) Bower, P.; Pareek, G. The History of Technologic Advancements in Urology. In *The History of Technologic Advancements in Urology*; Moran, M. E., Nakada, S. Y., Patel, S. R., Eds.; Springer International Publishing : Imprint: Springer: Cham, 2018; pp 87–96. https://doi.org/10.1007/978-3-319-61691-9.
(35) Morrow, P. A. *A System of Genito-Urinary Diseases, Syphilology and Dermatology*; Appleton: New York, 1893.
(36) Hale, G. M.; Querry, M. R. Optical Constants of Water in the 200-Nm to 200-Mm Wavelength Region. 9.
(37) Sayer, J.; Johnson, D. E.; Price, R. E.; Cromeens, D. M. Ureteral Lithotripsy with the Holmium:YAG Laser. *Journal of Clinical Laser Medicine & Surgery* **1993**, *11* (2), 61–65. https://doi.org/10.1089/clm.1993.11.61.
(38) Chan, K. F.; Vassar, G. J.; Pfefer, T. J.; Teichman, J. M. H.; Glickman, R. D.; Weintraub, S. T.; Welch, A. J. Holmium:YAG Laser Lithotripsy: A Dominant Photothermal Ablative Mechanism with Chemical Decomposition of Urinary Calculi. *Lasers in Surgery and Medicine* **1999**, *25* (1), 22–37. https://doi.org/10.1002/(SICI)1096-9101(1999)25:1<22::AID-LSM4>3.0.CO;2-6.
(39) Vassar, G. J.; Chan, K. F.; Teichman, J. M. H.; Glickman, R. D.; Weintraub, S. T.; Pfefer, T. J.; Welch, A. J. Holmium: YAG Lithotripsy: Photothermal Mechanism. *Journal of Endourology* **1999**, *13* (3), 181–190. https://doi.org/10.1089/end.1999.13.181.
(40) Romeu, G.; Marzullo-Zucchet, L. J.; Díaz, J.; Villarroya, S.; Budía, A.; Ordaz, D. de G.; Caballer, V.; Vivas, D. Comparing Extracorporeal Shock Wave Lithotripsy and Ureteroscopy Laser Lithotripsy for Treatment of Urinary Stones Smaller than 2 Cm: A Cost-Utility Analysis in the Spanish Clinical Setting. *World J Urol* **2021**, *39* (9), 3593–3598. https://doi.org/10.1007/s00345-021-03620-w.

(41) Friedlander, D. F.; Brant, A.; McClure, T. D.; Del Pizzo, J.; Nowels, M. A.; Trinh, Q.-D.; Sedrakyan, A.; Chughtai, B. Real-World Comparative Effectiveness of Shockwave Lithotripsy versus Ureterorenoscopy for the Treatment of Urinary Stones. *World J Urol* **2021**, *39* (6), 2177–2182. https://doi.org/10.1007/s00345-020-03430-6.
(42) Fried, N. M. Thulium Fiber Laser Lithotripsy: An in Vitro Analysis of Stone Fragmentation Using a Modulated 110-Watt Thulium Fiber Laser at 1.94 Mm. *Lasers in Surgery and Medicine* **2005**, *37* (1), 53–58. https://doi.org/10.1002/lsm.20196.
(43) Fried, N. M.; Irby, P. B. Advances in Laser Technology and Fibre-Optic Delivery Systems in Lithotripsy. *Nat Rev Urol* **2018**, *15* (9), 563–573. https://doi.org/10.1038/s41585-018-0035-8.
(44) Hardy, L. A.; Vinnichenko, V.; Fried, N. M. High Power Holmium:YAG versus Thulium Fiber Laser Treatment of Kidney Stones in Dusting Mode: Ablation Rate and Fragment Size Studies. *Lasers in Surgery and Medicine* **2019**, *51* (6), 522–530. https://doi.org/10.1002/lsm.23057.
(45) Aldoukhi, A. H.; Roberts, W. W.; Hall, T. L.; Ghani, K. R. Watch Your Distance: The Role of Laser Fiber Working Distance on Fragmentation When Altering Pulse Width or Modulation. *Journal of Endourology* **2019**, *33* (2), 120–126. https://doi.org/10.1089/end.2018.0572.
(46) Cölfen, H. (Helmut); Antonietti, M.; Cölfen, H.; Antonietti, M. *Mesocrystals and Nonclassical Crystallization*; John Wiley & Sons Ltd: West Sussex, England, 2008.
(47) Davey, R. J.; Garside, J. *From Molecules to Crystallizers*; Oxford Chemistry Primers; Oxford University Press: Oxford, New York, 2001.
(48) Ruiz-Agudo, E.; Burgos-Cara, A.; Ruiz-Agudo, C.; Ibañez-Velasco, A.; Cölfen, H.; Rodriguez-Navarro, C. A Non-Classical View on Calcium Oxalate Precipitation and the Role of Citrate. *Nat Commun* **2017**, *8* (1), 768. https://doi.org/10.1038/s41467-017-00756-5.
(49) Hajir, M.; Graf, R.; Tremel, W. Stable Amorphous Calcium Oxalate: Synthesis and Potential Intermediate in Biomineralization. *Chemical Communications* **2014**, *50* (49), 6534–6536. https://doi.org/10.1039/C4CC02146K.
(50) Ihli, J.; Wang, Y.-W.; Cantaert, B.; Kim, Y.-Y.; Green, D. C.; Bomans, P. H. H.; Sommerdijk, N. A. J. M.; Meldrum, F. C. Precipitation of Amorphous Calcium Oxalate in Aqueous Solution. *Chem. Mater.* **2015**, *27* (11), 3999–4007. https://doi.org/10.1021/acs.chemmater.5b01642.
(51) Jenewein, C.; Ruiz-Agudo, C.; Wasman, S.; Gower, L.; Cölfen, H. Development of a Novel CaCO3 PILP Based Cementation Method for Quartz Sand. *CrystEngComm* **2019**, *21* (14), 2273–2280. https://doi.org/10.1039/C8CE02158A.
(52) Millan, A. Crystal Growth Shape of Whewellite Polymorphs: Influence of Structure Distortions on Crystal Shape. *Crystal Growth & Design* **2001**, *1* (3), 245–254. https://doi.org/10.1021/cg0055530.
(53) Robinson, J. W.; Ghani, K. R.; Roberts, W. W.; Matzger, A. J. Near-Infrared Absorption Coefficients in Kidney Stone Minerals and Their Relation to Crystal Structure. *J. Phys. Chem. C* **2023**, *127* (1), 759–767. https://doi.org/10.1021/acs.jpcc.2c07475.
(54) Zheng, C.; F. Greer, H.; Chiang, C.-Y.; Zhou, W. Microstructural Study of the Formation Mechanism of Metal–Organic Framework MOF-5. *CrystEngComm* **2014**, *16* (6), 1064–1070. https://doi.org/10.1039/C3CE41291A.

(55) Xie, B.; Halter, T. J.; Borah, B. M.; Nancollas, G. H. Aggregation of Calcium Phosphate and Oxalate Phases in the Formation of Renal Stones. *Crystal Growth & Design* **2015**, *15* (1), 204–211. https://doi.org/10.1021/cg501209h.
(56) Glickman, R. D.; M.d, J. M. H. T.; Vassar, G. J.; Weintraub, S. T.; Chan, K. F.; Pfefer, T. J.; Welch, A. J. Chemical Decomposition of Urinary Stones during Holmium-Laser Lithotripsy: II. Evidence for Photothermal Breakdown. In *Laser-Tissue Interaction X: Photochemical, Photothermal, and Photomechanical*; SPIE, 1999; Vol. 3601, pp 369–376. https://doi.org/10.1117/12.350022.
(57) Shalini, S.; Frank, D. S.; Aldoukhi, A. H.; Majdalany, S. E.; Roberts, W. W.; Ghani, K. R.; Matzger, A. J. Assessing the Role of Light Absorption in Laser Lithotripsy by Isotopic Substitution of Kidney Stone Materials. *ACS Biomater. Sci. Eng.* **2020**, *6* (9), 5274–5280. https://doi.org/10.1021/acsbiomaterials.0c00790.
(58) Chan, K. F.; Vassar, G. J.; Pfefer, T. J.; M.d, J. M. H. T.; Glickman, R. D.; Weintraub, S. T.; Welch, A. J. Chemical Decomposition of Urinary Stones during Holmium-Laser Lithotripsy: I. Lack of a Photomechanical Effect. In *Laser-Tissue Interaction X: Photochemical, Photothermal, and Photomechanical*; SPIE, 1999; Vol. 3601, pp 377–386. https://doi.org/10.1117/12.350023.
(59) Robinson, J. W.; Marom, R.; Ghani, K. R.; Roberts, W. W.; Matzger, A. J. Performance of Brushite Plaster as Kidney Stone Phantoms for Laser Lithotripsy. *Urolithiasis* **2023**, *52* (1), 10. https://doi.org/10.1007/s00240-023-01505-8.
(60) Frank, D. S.; Aldoukhi, A. H.; Roberts, W. W.; Ghani, K. R.; Matzger, A. J. Polymer–Mineral Composites Mimic Human Kidney Stones in Laser Lithotripsy Experiments. *ACS Biomater. Sci. Eng.* **2019**, *5* (10), 4970–4975. https://doi.org/10.1021/acsbiomaterials.9b01130.
(61) Taş, A. C. Molten Salt Synthesis of Calcium Hydroxyapatite Whiskers. *Journal of the American Ceramic Society* **2004**, *84* (2), 295–300. https://doi.org/10.1111/j.1151-2916.2001.tb00653.x.
(62) Prywer, J.; Sieroń, L.; Czylkowska, A. Struvite Grown in Gel, Its Crystal Structure at 90 K and Thermoanalytical Study. *Crystals* **2019**, *9* (2), 89. https://doi.org/10.3390/cryst9020089.
(63) Thomas, A. Biomimetic Growth and Morphology Control of Calcium Oxalates, Max Planck Institute, 2009.
(64) Thomas, A.; Rosseeva, E.; Hochrein, O.; Carrillo-Cabrera, W.; Simon, P.; Duchstein, P.; Zahn, D.; Kniep, R. Mimicking the Growth of a Pathologic Biomineral: Shape Development and Structures of Calcium Oxalate Dihydrate in the Presence of Polyacrylic Acid. *Chem. Eur. J.* **2012**, *18* (13), 4000–4009. https://doi.org/10.1002/chem.201102228.
(65) Greenspan, L. Humidity Fixed Points of Binary Saturated Aqueous Solutions. *J. RES. NATL. BUR. STAN. SECT. A.* **1977**, *81A* (1), 89. https://doi.org/10.6028/jres.081A.011.
(66) Ibis, F.; Dhand, P.; Suleymanli, S.; van der Heijden, A. E. D. M.; Kramer, H. J. M.; Eral, H. B. A Combined Experimental and Modelling Study on Solubility of Calcium Oxalate Monohydrate at Physiologically Relevant pH and Temperatures. *Crystals* **2020**, *10* (10), 924. https://doi.org/10.3390/cryst10100924.
(67) Robertson, K. M.; Milliken, R. E.; Li, S. Estimating Mineral Abundances of Clay and Gypsum Mixtures Using Radiative Transfer Models Applied to Visible-near Infrared Reflectance Spectra. *Icarus* **2016**, *277*, 171–186. https://doi.org/10.1016/j.icarus.2016.04.034.

(68) Roush, T. L.; Esposito, F.; Rossman, G. R.; Colangeli, L. Estimated Optical Constants of Gypsum in the Regions of Weak Absorptions: Application of Scattering Theories and Comparisons to Independent Measurements. *Journal of Geophysical Research: Planets* **2007**, *112* (E10). https://doi.org/10.1029/2007JE002920.
(69) Ye, C.; Sklute, E. C.; Glotch, T. D. Orientation Averaged Visible/Near-Infrared and Mid-Infrared Optical Constants of Hydrous Ca-Sulfates: Gypsum and Bassanite. *Earth and Space Science* **2021**, *8* (10), e2021EA001834. https://doi.org/10.1029/2021EA001834.
(70) Jansen, E. D.; van Leeuwen, T. G.; Motamedi, M.; Borst, C.; Welch, A. J. Temperature Dependence of the Absorption Coefficient of Water for Midinfrared Laser Radiation. *Lasers in Surgery and Medicine* **1994**, *14* (3), 258–268. https://doi.org/10.1002/lsm.1900140308.
(71) Warren, S. G.; Brandt, R. E. Optical Constants of Ice from the Ultraviolet to the Microwave: A Revised Compilation. *J. Geophys. Res.* **2008**, *113* (D14), D14220. https://doi.org/10.1029/2007JD009744.
(72) Chan, K. F.; Hammer, D. X.; Choi, B.; Teichman, J. M. h.; McGUFF, H. S.; Pratisto, H.; Jansen, E. D.; Welch, A. J. Free Electron Laser Lithotripsy: Threshold Radiant Exposures. *Journal of Endourology* **2000**, *14* (2), 161–167. https://doi.org/10.1089/end.2000.14.161.
(73) Rozenberg, M.; Shoham, G.; Reva, I.; Fausto, R. A Correlation between the Proton Stretching Vibration Red Shift and the Hydrogen Bond Length in Polycrystalline Amino Acids and Peptides. *Phys. Chem. Chem. Phys.* **2005**, *7* (11), 2376–2383. https://doi.org/10.1039/B503644E.
(74) Ratajczak, H.; Orville-Thomas, W. J. Hydrogen-Bond Studies: Part I. The Relation between Vibrational Frequencies and Bond Length in O-H β O Hydrogen-Bonded Systems. *Journal of Molecular Structure* **1968**, *1* (6), 449–461. https://doi.org/10.1016/0022-2860(68)87019-X.
(75) Libowitzky, E. Correlation of 0-H Stretching Frequencies and 0-H· · ·0 Hydrogen Bond Lengths in Minerals. 13.
(76) Blackmon, R. L.; Fried, N. M.; Irby, P. B. Comparison of Holmium:YAG and Thulium Fiber Laser Lithotripsy: Ablation Thresholds, Ablation Rates, and Retropulsion Effects. *JBO* **2011**, *16* (7), 071403. https://doi.org/10.1117/1.3564884.
(77) Petit, I.; Belletti, G. D.; Debroise, T.; Llansola-Portoles, M. J.; Lucas, I. T.; Leroy, C.; Bonhomme, C.; Bonhomme-Coury, L.; Bazin, D.; Daudon, M.; Letavernier, E.; Haymann, J. P.; Frochot, V.; Babonneau, F.; Quaino, P.; Tielens, F. Vibrational Signatures of Calcium Oxalate Polyhydrates. *ChemistrySelect* **2018**, *3* (31), 8801–8812. https://doi.org/10.1002/slct.201801611.
(78) Hirsch, A.; Azuri, I.; Addadi, L.; Weiner, S.; Yang, K.; Curtarolo, S.; Kronik, L. Infrared Absorption Spectrum of Brushite from First Principles. *Chem. Mater.* **2014**, *26* (9), 2934–2942. https://doi.org/10.1021/cm500650t.
(79) Sidorczuk, D.; Kozanecki, M.; Civalleri, B.; Pernal, K.; Prywer, J. Structural and Optical Properties of Struvite. Elucidating Structure of Infrared Spectrum in High Frequency Range. *J. Phys. Chem. A* **2020**, *124* (42), 8668–8678. https://doi.org/10.1021/acs.jpca.0c04707.
(80) Conti, C.; Casati, M.; Colombo, C.; Realini, M.; Brambilla, L.; Zerbi, G. Phase Transformation of Calcium Oxalate Dihydrate–Monohydrate: Effects of Relative Humidity and New Spectroscopic Data. *Spectrochimica Acta Part A: Molecular and*

Biomolecular Spectroscopy **2014**, *128*, 413–419. https://doi.org/10.1016/j.saa.2014.02.182.
(81) A. Curry, N.; W. Jones, D. Crystal Structure of Brushite, Calcium Hydrogen Orthophosphate Dihydrate: A Neutron-Diffraction Investigation. *Journal of the Chemical Society A: Inorganic, Physical, Theoretical* **1971**, *0* (0), 3725–3729. https://doi.org/10.1039/J19710003725.
(82) Tobar, C.; Cordova, R.; Solomon, T.; Palombo, K.; Olivares, G.; Helston, J.; Luo, W.; Cizmeciyan, D.; Benesi, A. Water Dynamics in Deuterated Gypsum, CaSO4·2D2O, Investigated by Solid State Deuterium NMR. *Journal of Magnetic Resonance* **2020**, *310*, 106640. https://doi.org/10.1016/j.jmr.2019.106640.
(83) Goldberga, I.; Patris, N.; Chen, C.-H.; Thomassot, E.; Trébosc, J.; Hung, I.; Gan, Z.; Berthomieu, D.; Métro, T.-X.; Bonhomme, C.; Gervais, C.; Laurencin, D. First Direct Insight into the Local Environment and Dynamics of Water Molecules in the Whewellite Mineral Phase: Mechanochemical Isotopic Enrichment and High-Resolution 17O and 2H NMR Analyses. *J. Phys. Chem. C* **2022**. https://doi.org/10.1021/acs.jpcc.2c02070.
(84) Todorov, L. G.; Sivaguru, M.; Krambeck, A. E.; Lee, M. S.; Lieske, J. C.; Fouke, B. W. GeoBioMed Perspectives on Kidney Stone Recurrence from the Reactive Surface Area of SWL-Derived Particles. *Sci Rep* **2022**, *12* (1), 18371. https://doi.org/10.1038/s41598-022-23331-5.
(85) Williams, J. C.; Lingeman, J. E.; Daudon, M.; Bazin, D. Using Micro Computed Tomographic Imaging for Analyzing Kidney Stones. *Comptes Rendus. Chimie* **2021**, *25* (S1), 1–12. https://doi.org/10.5802/crchim.89.
(86) Zarse, C. A.; McAteer, J. A.; Sommer, A. J.; Kim, S. C.; Hatt, E. K.; Lingeman, J. E.; Evan, A. P.; Williams, J. C. Nondestructive Analysis of Urinary Calculi Using Micro Computed Tomography. *BMC Urol* **2004**, *4* (1), 15. https://doi.org/10.1186/1471-2490-4-15.
(87) Gleeson, M.; Morizet, J.; Mahou, P.; Daudon, M.; Bazin, D.; Stringari, C.; Schanne-Klein, M.-C.; Beaurepaire, E. Kidney Stone Classification Using Multimodal Multiphoton Microscopy. *ACS Photonics* **2023**, *10* (10), 3594–3604. https://doi.org/10.1021/acsphotonics.3c00651.
(88) Manzoor, M. A. P.; Agrawal, A. K.; Singh, B.; Mujeeburahiman, M.; Rekha, P.-D. Morphological Characteristics and Microstructure of Kidney Stones Using Synchrotron Radiation μCT Reveal the Mechanism of Crystal Growth and Aggregation in Mixed Stones. *PLOS ONE* **2019**, *14* (3), e0214003. https://doi.org/10.1371/journal.pone.0214003.
(89) Kaiser, J.; Holá, M.; Galiová, M.; Novotný, K.; Kanický, V.; Martinec, P.; Ščučka, J.; Brun, F.; Sodini, N.; Tromba, G.; Mancini, L.; Kořistková, T. Investigation of the Microstructure and Mineralogical Composition of Urinary Calculi Fragments by Synchrotron Radiation X-Ray Microtomography: A Feasibility Study. *Urol Res* **2011**, *39* (4), 259–267. https://doi.org/10.1007/s00240-010-0343-9.
(90) Racek, M.; Racek, J.; Hupáková, I. Scanning Electron Microscopy in Analysis of Urinary Stones. *Scandinavian Journal of Clinical and Laboratory Investigation* **2019**, *79* (3), 208–217. https://doi.org/10.1080/00365513.2019.1578995.
(91) Chatterjee, P.; Chakraborty, A.; Mukherjee, A. K. Phase Composition and Morphological Characterization of Human Kidney Stones Using IR Spectroscopy, Scanning Electron Microscopy and X-Ray Rietveld Analysis. *Spectrochimica Acta Part A: Molecular and Biomolecular Spectroscopy* **2018**, *200*, 33–42. https://doi.org/10.1016/j.saa.2018.04.005.

(92) Jussiani, E. I.; Colaço, M. V.; Kuplich, L.; Carrerete, F.; Pinto, R.; Barroso, R. C.; Appoloni, C. R.; Nogueira, L. P. Mineral Composition of Urinary Stones by Single Energy Desktop Microtomography. *J. Inst.* **2018**, *13* (06), C06008–C06008. https://doi.org/10.1088/1748-0221/13/06/C06008.
(93) Duan, X.; Qu, M.; Wang, J.; Trevathan, J.; Vrtiska, T.; Williams, J. C.; Krambeck, A.; Lieske, J.; McCollough, C. Differentiation of Calcium Oxalate Monohydrate and Calcium Oxalate Dihydrate Stones Using Quantitative Morphological Information from Micro-Computerized and Clinical Computerized Tomography. *Journal of Urology* **2013**, *189* (6), 2350–2356. https://doi.org/10.1016/j.juro.2012.11.004.
(94) Khan, S. R.; Hackett, R. L. Identification of Urinary Stone and Sediment Crystals by Scanning Electron Microscopy and X-Ray Microanalysis. *The Journal of Urology* **1986**, *135* (4), 818–825. https://doi.org/10.1016/S0022-5347(17)45868-X.
(95) Bazin, D.; Frochot, V.; Haymann, J.-P.; Letavernier, E.; Daudon, M. Crystal Size in μ Crystalline Pathologies and Its Clinical Implication. *Comptes Rendus. Chimie* **2022**, *25* (S1), 133–147. https://doi.org/10.5802/crchim.96.
(96) Costa-Bauzá, A.; Grases, F.; Julià, F. The Power of Desktop Scanning Electron Microscopy with Elemental Analysis for Analyzing Urinary Stones. *Urolithiasis* **2023**, *51* (1), 50. https://doi.org/10.1007/s00240-023-01424-8.
(97) Dessombz, A.; Méria, P.; Bazin, D.; Daudon, M. Prostatic Stones: Evidence of a Specific Chemistry Related to Infection and Presence of Bacterial Imprints. *PLOS ONE* **2012**, *7* (12), e51691. https://doi.org/10.1371/journal.pone.0051691.
(98) Ma, R.; Luo, X.; Li, Q.; Zhong, H. The Systematic Classification of Urinary Stones Combine-Using FTIR and SEM-EDAX. *International Journal of Surgery* **2017**, *41*, 150–161. https://doi.org/10.1016/j.ijsu.2017.03.080.
(99) Uvarov, V.; Popov, I.; Shapur, N.; Abdin, T.; Gofrit, O. N.; Pode, D.; Duvdevani, M. X-Ray Diffraction and SEM Study of Kidney Stones in Israel: Quantitative Analysis, Crystallite Size Determination, and Statistical Characterization. *Environ Geochem Health* **2011**, *33* (6), 613–622. https://doi.org/10.1007/s10653-011-9374-6.
(100) H. Valido, I.; Resina-Gallego, M.; Yousef, I.; Luque-Gálvez, M. P.; Valiente, M.; López-Mesas, M. Calcium Oxalate Kidney Stones, Where Is the Organic Matter?: A Synchrotron Based Infrared Microspectroscopy Study. *J. Biophotonics* **2020**, *13* (12). https://doi.org/10.1002/jbio.202000303.
(101) Daudon, M.; Protat, M. F.; Reveillaud, R. J.; Jaeschke-Boyer, H. Infrared Spectrometry and Raman Microprobe in the Analysis of Urinary Calculi. *Kidney International* **1983**, *23* (6), 842–850. https://doi.org/10.1038/ki.1983.104.
(102) Lucas, I. T.; Bazin, D.; Daudon, M. Raman Opportunities in the Field of Pathological Calcifications. *Comptes Rendus. Chimie* **2022**, *25* (S1), 83–103. https://doi.org/10.5802/crchim.110.
(103) Tamosaityte, S.; Pucetaite, M.; Zelvys, A.; Varvuolyte, S.; Hendrixson, V.; Sablinskas, V. Raman Spectroscopy as a Non-Destructive Tool to Determine the Chemical Composition of Urinary Sediments. *Comptes Rendus. Chimie* **2022**, *25* (S1), 73–82. https://doi.org/10.5802/crchim.121.
(104) Zhu, W.; Sun, Z.; Ye, L.; Zhang, X.; Xing, Y.; Zhu, Q.; Yang, F.; Jiang, G.; Chen, Z.; Chen, K.; Ma, E.; Wang, L. Preliminary Assessment of a Portable Raman Spectroscopy System for Post-Operative Urinary Stone Analysis. *World J Urol* **2022**, *40* (1), 229–235. https://doi.org/10.1007/s00345-021-03838-8.

(105) Cui, X.; Zhao, Z.; Zhang, G.; Chen, S.; Zhao, Y.; Lu, J. Analysis and Classification of Kidney Stones Based on Raman Spectroscopy. *Biomed. Opt. Express, BOE* **2018**, *9* (9), 4175–4183. https://doi.org/10.1364/BOE.9.004175.
(106) Frochot, V.; Castiglione, V.; Lucas, I. T.; Haymann, J.-P.; Letavernier, E.; Bazin, D.; Fogazzi, G. B.; Daudon, M. Advances in the Identification of Calcium Carbonate Urinary Crystals. *Clinica Chimica Acta* **2021**, *515*, 1–4. https://doi.org/10.1016/j.cca.2020.12.024.
(107) Chang, C.-C.; Chiu, Y. Applying Quantitative Micro-Raman Spectroscopy to Analyze Stone Compositions Extracted from Ureteroscopic Lithotripsy Urine. *Urological Science* **2017**, *28* (1), 19–22. https://doi.org/10.1016/j.urols.2016.04.002.
(108) Wentrup-Byrne, E.; Armstrong, C. A.; Armstrong, R. S.; Collins, B. M. Fourier Transform Raman Microscopic Mapping of the Molecular Components in a Human Tooth. *Journal of Raman Spectroscopy* **1997**, *28* (2–3), 151–158. https://doi.org/10.1002/(SICI)1097-4555(199702)28:2/3<151::AID-JRS71>3.0.CO;2-5.
(109) Timlin, J. A.; Carden, A.; Morris, M. D. Chemical Microstructure of Cortical Bone Probed by Raman Transects. *Appl. Spectrosc., AS* **1999**, *53* (11), 1429–1435.
(110) Khan, A. F.; Awais, M.; Khan, A. S.; Tabassum, S.; Chaudhry, A. A.; Rehman, I. U. Raman Spectroscopy of Natural Bone and Synthetic Apatites. *Applied Spectroscopy Reviews* **2013**, *48* (4), 329–355. https://doi.org/10.1080/05704928.2012.721107.
(111) Golcuk, K.; Mandair, G. S.; Callender, A. F.; Sahar, N.; Kohn, D. H.; Morris, M. D. Is Photobleaching Necessary for Raman Imaging of Bone Tissue Using a Green Laser? *Biochimica et Biophysica Acta (BBA) - Biomembranes* **2006**, *1758* (7), 868–873. https://doi.org/10.1016/j.bbamem.2006.02.022.
(112) Gong, B.; Oest, M. E.; Mann, K. A.; Damron, T. A.; Morris, M. D. Raman Spectroscopy Demonstrates Prolonged Alteration of Bone Chemical Composition Following Extremity Localized Irradiation. *Bone* **2013**, *57* (1), 252–258. https://doi.org/10.1016/j.bone.2013.08.014.
(113) Shea, D. A.; Morris, M. D. Bone Tissue Fluorescence Reduction for Visible Laser Raman Spectroscopy. *Appl. Spectrosc., AS* **2002**, *56* (2), 182–186.
(114) Chen, T.-C.; Shea, D. A.; Morris, M. D. Effect of Hydrogen Peroxide Bleaching on Bone Mineral/Matrix Ratio. *Appl. Spectrosc., AS* **2002**, *56* (8), 1035–1037.
(115) Yakubovskaya, E.; Zaliznyak, T.; Martínez Martínez, J.; Taylor, G. T. Tear Down the Fluorescent Curtain: A New Fluorescence Suppression Method for Raman Microspectroscopic Analyses. *Sci Rep* **2019**, *9* (1), 15785. https://doi.org/10.1038/s41598-019-52321-3.
(116) Ulian, G.; Valdrè, G.; Corno, M.; Ugliengo, P. The Vibrational Features of Hydroxylapatite and Type A Carbonated Apatite: A First Principle Contribution. *American Mineralogist* **2013**, *98* (4), 752–759. https://doi.org/10.2138/am.2013.4315.
(117) Casciani, F.; Condrate Sr., R. A. The Vibrational Spectra of Brushite, CaHPO4·2H2O. *Spectroscopy Letters* **1979**, *12* (10), 699–713. https://doi.org/10.1080/00387017908069196.
(118) Stefov, V.; Šoptrajanov, B.; Kuzmanovski, I.; Lutz, H. D.; Engelen, B. Infrared and Raman Spectra of Magnesium Ammonium Phosphate Hexahydrate (Struvite) and Its Isomorphous Analogues. III. Spectra of Protiated and Partially Deuterated Magnesium Ammonium Phosphate Hexahydrate. *Journal of Molecular Structure* **2005**, *752* (1), 60–67. https://doi.org/10.1016/j.molstruc.2005.05.040.

(119) Izatulina, A. R.; Gurzhiy, V. V.; Krzhizhanovskaya, M. G.; Chukanov, N. V.; Panikorovskii, T. L. Thermal Behavior and Phase Transition of Uric Acid and Its Dihydrate Form, the Common Biominerals Uricite and Tinnunculite. *Minerals* **2019**, *9* (6), 373. https://doi.org/10.3390/min9060373.
(120) Frincu, M. C.; Fogarty, C. E.; Swift, J. A. Epitaxial Relationships between Uric Acid Crystals and Mineral Surfaces: A Factor in Urinary Stone Formation. *Langmuir* **2004**, *20* (16), 6524–6529. https://doi.org/10.1021/la049091u.
(121) Königsberger, E.; Tromans, A.; May, P. M.; Hefter, G. Solubility of Calcium Oxalate Monohydrate in Concentrated Electrolyte Solutions. *J. Chem. Eng. Data* **2021**, *66* (1), 840–847. https://doi.org/10.1021/acs.jced.0c00925.
(122) Pramanik, R.; Asplin, J. R.; Jackson, M. E.; Williams, J. C. Protein Content of Human Apatite and Brushite Kidney Stones: Significant Correlation with Morphologic Measures. *Urol Res* **2008**, *36* (5), 251–258. https://doi.org/10.1007/s00240-008-0151-7.
(123) Daudon, M.; Jungers, P.; Bazin, D.; Williams, J. C. Recurrence Rates of Urinary Calculi According to Stone Composition and Morphology. *Urolithiasis* **2018**, *46* (5), 459–470. https://doi.org/10.1007/s00240-018-1043-0.
(124) Sarigul, N.; Korkmaz, F.; Kurultak, İ. A New Artificial Urine Protocol to Better Imitate Human Urine. *Sci Rep* **2019**, *9* (1), 20159. https://doi.org/10.1038/s41598-019-56693-4.
(125) Clapham, L.; McLean, R. J. C.; Nickel, J. C.; Downey, J.; Costerton, J. W. The Influence of Bacteria on Struvite Crystal Habit and Its Importance in Urinary Stone Formation. *Journal of Crystal Growth* **1990**, *104* (2), 475–484. https://doi.org/10.1016/0022-0248(90)90150-J.
(126) Bayuseno, A. P.; Schmahl, W. W. Thermal Decomposition of Struvite in Water: Qualitative and Quantitative Mineralogy Analysis. *Environmental Technology* **2020**, *41* (27), 3591–3597. https://doi.org/10.1080/09593330.2019.1615558.
(127) Jacobs, D. H., A. Hesse ,D. Chemolysis of Struvite Stones by Acidification of Artificial Urine - An in Vitro Study. *Scandinavian Journal of Urology and Nephrology* **2001**, *35* (5), 345–349. https://doi.org/10.1080/003655901753224387.
(128) Awonusi, A.; Morris, M. D.; Tecklenburg, M. M. J. Carbonate Assignment and Calibration in the Raman Spectrum of Apatite. *Calcif Tissue Int* **2007**, *81* (1), 46–52. https://doi.org/10.1007/s00223-007-9034-0.
(129) Gault, M. H.; Chafe, L.; Longerich, L.; Mason, R. A. Calcium and Calcium Magnesium Carbonate Specimens Submitted as Urinary Tract Stones. *The Journal of Urology* **1993**, *149* (2), 244–249. https://doi.org/10.1016/S0022-5347(17)36047-0.
(130) Izatulina, A. R.; Gurzhiy, V. V.; Krzhizhanovskaya, M. G.; Kuz'mina, M. A.; Leoni, M.; Frank-Kamenetskaya, O. V. Hydrated Calcium Oxalates: Crystal Structures, Thermal Stability, and Phase Evolution. *Crystal Growth & Design* **2018**, *18* (9), 5465–5478. https://doi.org/10.1021/acs.cgd.8b00826.
(131) Echigo, T.; Kimata, M.; Kyono, A.; Shimizu, M.; Hatta, T. Re-Investigation of the Crystal Structure of Whewellite [$Ca(C_2O_4)\cdot H_2O$] and the Dehydration Mechanism of Caoxite [$Ca(C_2O_4)\cdot 3H_2O$]. *Mineral. mag.* **2005**, *69* (1), 77–88. https://doi.org/10.1180/0026461056910235.
(132) Liu, Y.; Zhong, P. BegoStone—a New Stone Phantom for Shock Wave Lithotripsy Research (L). *The Journal of the Acoustical Society of America* **2002**, *112* (4), 1265–1268. https://doi.org/10.1121/1.1501905.

(133) Esch, E.; Simmons, W. N.; Sankin, G.; Cocks, H. F.; Preminger, G. M.; Zhong, P. A Simple Method for Fabricating Artificial Kidney Stones of Different Physical Properties. *Urol Res* **2010**, *38* (4), 315–319. https://doi.org/10.1007/s00240-010-0298-x.
(134) Charles Chuong, C. J.; Zhong, P.; Preminger, G. M. A Comparison of Stone Damage Caused by Different Modes of Shock Wave Generation. *The Journal of Urology* **1992**, *148* (1), 200–205. https://doi.org/10.1016/S0022-5347(17)36553-9.
(135) Rassweiler, J.; Irion, U.; Strauss, R.; Bub, P.; Eisenberger, F. Technical Considerations Using a Pulsed Neodym-YAG Laser for Endoscopic Shock Wave Lithotripsy. *European Urology* **2017**, *16* (5), 374–377. https://doi.org/10.1159/000471620.
(136) King, J. B.; Katta, N.; Teichman, J. M. H.; Tunnell, J. W.; Milner, T. E. Mechanisms of Pulse Modulated Holmium:YAG Lithotripsy. *Journal of Endourology* **2021**, *35* (S3), S-29. https://doi.org/10.1089/end.2021.0742.
(137) Heimbach, D.; Jacobs, D.; Winter, P.; Süverkrüp, R.; Hesse, A. Production of Artificial Urinary Stones from Natural Materials and Their Physical Properties. *Scandinavian Journal of Urology and Nephrology* **1997**, *31* (1), 9–13. https://doi.org/10.3109/00365599709070294.
(138) Bader, M. J.; Pongratz, T.; Khoder, W.; Stief, C. G.; Herrmann, T.; Nagele, U.; Sroka, R. Impact of Pulse Duration on Ho:YAG Laser Lithotripsy: Fragmentation and Dusting Performance. *World J Urol* **2015**, *33* (4), 471–477. https://doi.org/10.1007/s00345-014-1429-8.
(139) Fadeeva, I. V.; Barinov, S. M.; Fomin, A. S. Polymer Materials Containing Calcium Phosphates for Medicine: Part I. Methylcellulose and Starch Containing Calcium Phosphates (Review). *Inorg. Mater. Appl. Res.* **2020**, *11* (1), 109–116. https://doi.org/10.1134/S2075113320010104.
(140) Alkhraisat, M. H.; Mariño, F. T.; Rodríguez, C. R.; Jerez, L. B.; Cabarcos, E. L. Combined Effect of Strontium and Pyrophosphate on the Properties of Brushite Cements. *Acta Biomaterialia* **2008**, *4* (3), 664–670. https://doi.org/10.1016/j.actbio.2007.12.001.
(141) Engstrand Unosson, J.; Persson, C.; Engqvist, H. An Evaluation of Methods to Determine the Porosity of Calcium Phosphate Cements. *Journal of Biomedical Materials Research Part B: Applied Biomaterials* **2015**, *103* (1), 62–71. https://doi.org/10.1002/jbm.b.33173.
(142) Grover, L. M.; Gbureck, U.; Hutton, A.; Farrar, D.; Ansell, C.; Barralet, J. E. Low Porosity $CaHPO_4$-$2H_2O$ Cement. *KEM* **2003**, *254–256*, 205–208. https://doi.org/10.4028/www.scientific.net/KEM.254-256.205.
(143) Xu, H. H.; Wang, P.; Wang, L.; Bao, C.; Chen, Q.; Weir, M. D.; Chow, L. C.; Zhao, L.; Zhou, X.; Reynolds, M. A. Calcium Phosphate Cements for Bone Engineering and Their Biological Properties. *Bone Res* **2017**, *5* (1), 1–19. https://doi.org/10.1038/boneres.2017.56.
(144) Zhang, J.; Liu, W.; Schnitzler, V.; Tancret, F.; Bouler, J.-M. Calcium Phosphate Cements for Bone Substitution: Chemistry, Handling and Mechanical Properties. *Acta Biomaterialia* **2014**, *10* (3), 1035–1049. https://doi.org/10.1016/j.actbio.2013.11.001.
(145) Tamimi, F.; Sheikh, Z.; Barralet, J. Dicalcium Phosphate Cements: Brushite and Monetite. *Acta Biomaterialia* **2012**, *8* (2), 474–487. https://doi.org/10.1016/j.actbio.2011.08.005.
(146) Marom, R.; Roberts, W. W.; Hall, T. L.; Robinson, J.; Matzger, A. J.; Ghani, K. R. Characterization of Thulium Fiber Laser Pulses: Differences between Short and Long Pulse. *Journal of Urology* **2023**, *209* (Supplement 4), e360. https://doi.org/10.1097/JU.0000000000003254.19.

(147) Wong, D. G.; Shiang, A.; Ostergar, A.; Sands, K. G. Enhanced Popcorning Using Polyanionic Chelating Solutions as Irrigation. *Urolithiasis* **2023**, *51* (1), 90. https://doi.org/10.1007/s00240-023-01464-0.
(148) Ostrowski, N.; Roy, A.; Kumta, P. N. Magnesium Phosphate Cement Systems for Hard Tissue Applications: A Review. *ACS Biomater. Sci. Eng.* **2016**, *2* (7), 1067–1083. https://doi.org/10.1021/acsbiomaterials.6b00056.
(149) Sarkar, A. K. Hydration/Dehydration Characteristics of Struvite and Dittmarite Pertaining to Magnesium Ammonium Phosphate Cement Systems. *J Mater Sci* **1991**, *26* (9), 2514–2518. https://doi.org/10.1007/BF01130204.
(150) Gelli, R.; Tonelli, M.; Martini, F.; Calucci, L.; Borsacchi, S.; Ridi, F. Effect of Borax on the Hydration and Setting of Magnesium Phosphate Cements. *Construction and Building Materials* **2022**, *348*, 128686. https://doi.org/10.1016/j.conbuildmat.2022.128686.
(151) Heimbach, D.; Jacobs, D.; Winter, P.; Hesse, A. Dissolution of Artificial (Natural) Stones in a Standard Model: First Results. *Journal of Endourology* **1997**, *11* (1), 63–66. https://doi.org/10.1089/end.1997.11.63.
(152) Bachmann, R.; Heimbach, D.; Kersjes, W.; Jacobs, D.; Schild, H.; Hesse, A. A New Type of Artificial Urinary Calculi: In Vitro Study by Spiral CT. *Investigative Radiology* **2000**, *35* (11), 672.
(153) Vermeulen, C. W.; Lyon, E. S. Mechanisms of Genesis and Growth of Calculi. *The American Journal of Medicine* **1968**, *45* (5), 684–692. https://doi.org/10.1016/0002-9343(68)90204-0.
(154) Vermeulen, C. W.; Ellis, J. E.; Hsu, T.-C. Experimental Observations on the Pathogenesis of Urinary Calculi. *Journal of Urology* **1966**, *95* (5), 681–690. https://doi.org/10.1016/S0022-5347(17)63518-3.
(155) Vermeulen, C. W.; Lyon, E. S.; Fried, F. A. On the Nature of the Stone-Forming Process. *Journal of Urology* **1965**, *94* (2), 176–186. https://doi.org/10.1016/S0022-5347(17)63596-1.
(156) Stamnes, K.; Tsay, S.-C.; Wiscombe, W.; Jayaweera, K. Numerically Stable Algorithm for Discrete-Ordinate-Method Radiative Transfer in Multiple Scattering and Emitting Layered Media. *Appl. Opt., AO* **1988**, *27* (12), 2502–2509. https://doi.org/10.1364/AO.27.002502.
(157) Libois, Q.; Picard, G.; France, J. L.; Arnaud, L.; Dumont, M.; Carmagnola, C. M.; King, M. D. Influence of Grain Shape on Light Penetration in Snow. *The Cryosphere* **2013**, *7* (6), 1803–1818. https://doi.org/10.5194/tc-7-1803-2013.
(158) Latimer, W. M.; Schutz, P. W.; Hicks, J. F. G. The Heat Capacity and Entropy of Calcium Oxalate from 19 to 300° Absolute. The Entropy and Free Energy of Oxalate Ion. *J. Am. Chem. Soc.* **1933**, *55* (3), 971–975. https://doi.org/10.1021/ja01330a015.
(159) Svoboda, R.; Zmrhalová, Z. O.; Galusek, D.; Brandová, D.; Chovanec, J. Thermal Decomposition of Mixed Calcium Oxalate Hydrates – Kinetic Deconvolution of Complex Heterogeneous Processes. *Physical Chemistry Chemical Physics* **2020**, *22* (16), 8889–8901. https://doi.org/10.1039/C9CP06867H.
(160) Sádovská, G.; Wolf, G. Enthalpy of Dissolution and Thermal Dehydration of Calcium Oxalate Hydrates. *J Therm Anal Calorim* **2015**, *119* (3), 2063–2068. https://doi.org/10.1007/s10973-014-4350-x.
(161) Suda, H.; Yashima, M.; Kakihana, M.; Yoshimura, M. Monoclinic .Tautm. Hexagonal Phase Transition in Hydroxyapatite Studied by X-Ray Powder Diffraction and Differential

Scanning Calorimeter Techniques. *J. Phys. Chem.* **1995**, *99* (17), 6752–6754. https://doi.org/10.1021/j100017a068.
(162) Stiehler, R. D.; Huffman, H. M. Thermal Data. IV. The Heats of Combustion of Adenine, Hypoxanthine, Guanine, Xanthine, Uric Acid, Allantoin and Alloxan. *J. Am. Chem. Soc.* **1935**, *57* (9), 1734–1740. https://doi.org/10.1021/ja01312a071.
(163) Wishart, D. S.; Guo, A.; Oler, E.; Wang, F.; Anjum, A.; Peters, H.; Dizon, R.; Sayeeda, Z.; Tian, S.; Lee, B. L.; Berjanskii, M.; Mah, R.; Yamamoto, M.; Jovel, J.; Torres-Calzada, C.; Hiebert-Giesbrecht, M.; Lui, V. W.; Varshavi, D.; Varshavi, D.; Allen, D.; Arndt, D.; Khetarpal, N.; Sivakumaran, A.; Harford, K.; Sanford, S.; Yee, K.; Cao, X.; Budinski, Z.; Liigand, J.; Zhang, L.; Zheng, J.; Mandal, R.; Karu, N.; Dambrova, M.; Schiöth, H. B.; Greiner, R.; Gautam, V. HMDB 5.0: The Human Metabolome Database for 2022. *Nucleic Acids Res* **2022**, *50* (D1), D622–D631. https://doi.org/10.1093/nar/gkab1062.
(164) Frost, R. L.; Palmer, S. J. Thermal Stability of the 'Cave' Mineral Brushite CaHPO4·2H2O – Mechanism of Formation and Decomposition. *Thermochimica Acta* **2011**, *521* (1), 14–17. https://doi.org/10.1016/j.tca.2011.03.035.
(165) Frost, R. L.; Weier, M. L.; Erickson, K. L. Thermal Decomposition of Struvite. *Journal of Thermal Analysis and Calorimetry* **2004**, *76* (3), 1025–1033. https://doi.org/10.1023/B:JTAN.0000032287.08535.b3.